nks

Nordisk kerne-sikkerheds-forskning
Nordisk kärn-säkerhets-forskning
Pohjoismainen ydin-turvallisuus-tutkimus
Nordic nuclear safety research

RAK2

NKS/RAK-2(96)TR-A2

STUDIES ON MELT-WATER-STRUCTURE INTERACTION DURING SEVERE ACCIDENTS

B. R. Sehgal
T. N. Dinh
T. J. Okkonen
V. A. Bui
R. R. Nourgaliev
J. Andersson

Division of Nuclear Power Safety
Royal Institute of Technology
100 44 Stockholm, Sweden

October 1996

Studies on Melt-Water-Structure Interaction During Severe Accidents

by

B.R. Sehgal
T.N. Dinh
T.J. Okkonen
V.A. Bui
R.R. Nourgaliev
J. Andersson

Division of Nuclear Power Safety
Royal Institute of Technology
100 44 Stockholm, Sweden

Abstract

Results of a series of studies, on melt-water-structure interactions which occur during the progression of a core melt-down accident, are described. The emphasis is on the in-vessel interactions and the studies are both experimental and analytical. Since, the studies performed resulted in papers published in proceedings of the technical meetings, and in journals, copies of a set of selected papers are attached to provide details. A summary of the results obtained is provided for the reader who does not, or cannot, venture into the perusal of the attached papers.

1. Introduction

This report describes the studies performed at the Division of Nuclear Power Safety on melt-water-structure interaction that occur during the progression of a core melt-down accident. These studies, which started in 1994, are sponsored by a consortium headed by SKI, to which the Swedish and Finnish power companies, the U.S. NRC, the Nuclear Power Inspectorate (HSK) in Switzerland, and the NKS Project also belong. This report is produced for publication as an NKS Project report.

2. Background

Much research has been performed in the last 15 years on the phenomenology of the progression of severe accidents in LWRs. Much has been learned and some of the issues relating to containment performance have been resolved [1]. These include for example PWR containment failure due to in-vessel steam explosions, direct containment heating (DCH); and the BWR Mark-I containment failure due to liner melt-through. Resolution of these issues was based on probabilistic arguments, supported by realistic descriptions of the phenomena, which were validated to varying extent by experimental data.

Areas of severe accident phenomenology which have received much attention but have not yet been adequately resolved are, (a) the interaction of corium melt with the lower head vessel wall in the presence or absence of water, (b) interaction of the melt jet upon it's release from the vessel with the containment space below the vessel, which may or may not contain a deep pool of water. The major questions of concern here are, (1) extent of the ablation of the initial hole, or failure in the vessel wall, through which the melt is discharged, since that determines the melt jet diameter and the mass rate of corium discharged into the containment, (2) the extent of spreading of the melt jet on the concrete basemat in the space under the vessel if there is none or little water present, (3) during interaction with a deep water pool, the fraction of the melt jet that will fragment and cool, and the fraction of the melt jet, which will not fragment, and deposit as a melt pool under water to attack the concrete basemat, (4) the coolability of the melt pool under water and (5) the long term coolability of the debris bed formed, if substantial fragmentation of the melt jet, with very small particles, is predicted to occur. Another question which has been asked, regarding the interaction of the melt with water, is the strength and the frequency of steam explosions, since, if they occur, they may fragment the jet completely into very small particles, produce a large amount of hydrogen in a very short time, and produce large dynamic loads on the containment.

Previous work in the U.S.A on the melt interactions with the vessel wall has largely been analytical [2], except for the experiments conducted at Sandia and reported by Pilch [3]. Those experiments, on hole ablation, were performed with iron-alumina thermite and covered a limited range on the ablation of the hole. A scaling relationship was derived and it was shown that the experiments did not cover the range pertinent to either the penetration--failure case or the vessel-creep-rupture case.

Large scale melt-vessel interaction experiments are currently being performed in the CORVIS Project [4] in Switzerland. Those experiments employ a flat steel plate loaded by a heated thermite melt. The heating of the thermite melt is done with graphite electrodes. Melt-water interactions are being studied experimentally at JRC Ispra under the auspices of the FARO Project [5]. Prototypic materials (UO2 - ZrO2 - Zr) of up to 150 kg are being used. These experiments are primarily directed towards in-vessel interactions, since in the experiments, the pressure is high and the water is saturated. A few experiments have been performed.

Recently a considerable body of work has been performed on the feasibility of retaining core melt material within the reactor pressure vessel (RPV), if the RPV can be flooded externally in the containment. Simulant material experiments [6] have been performed in the COPO facility in Finland, at the University of California Santa Barbara, and at the University of California, Los Angeles. Further simulant material experiments are planned in the Nuclear Research Center in Grenoble; and a prototypic material program RASPLAV [7] is ongoing at the Kurchatov Institute in Moscow. Melt spreading has been studied analytically at Argonne National Laboratory. A number of experiments [8] with stainless steel melt have been performed in Japan. The French researchers have constructed a small scale facility at Grenoble to perform spreading experiments with simulant materials [9]. Other experiments have also started recently and more data should be obtained in the future.

Large scale melt coolability experiments are currently being performed at Argonne National Laboratory, under the auspices of the MACE Program [10]. One test showing partial coolability has been successfully performed. A large scale test employing $\approx$ 2000 kg of $U0_2$-$Zr0_2$ melt is scheduled to be performed near the end of 1996. Particulate debris coolability experiments have been performed in several laboratories over a number of years and successful correlations [11] have been developed for one-dimensional beds cooled by water entry from top and bottom. There is, however, very little data on multi- dimensional beds [12], of variable particle size, shape and dimensions, that may be generated in the ex-vessel melt-water interactions that lead to considerable fragmentation.

The brief review above points to the situation of inadequate resolution of several key issues in the progression of the severe accidents, which has prevented an adequate assessment of the risks. An example is the quantification of the risks for the Swedish and Finnish BWRs, which specify automatic flooding of the lower containment drywell in the event of the core uncovery. A study performed at KTH recently [13], identified the same issues as those enumerated above, whose phenomenologies have such large uncertainties that an adequate risk assessment was not possible. On such considerations, we proposed the Melt-Structure-Water Interaction Project to SKI, developed the workscope and obtained support from other organizations, including the NKS Project.

3. Objectives

The primary objectives of our research program are to obtain data on the melt-structure-water interactions that occur during the progression of a severe accident, after a core melt has occurred, in a LWR. Specifically, data will be obtained for

- the ablation process, which increases the size of a hole, or a local failure, in the power head wall of the reactor pressure vessel (RPV), as the core melt is discharged into the containment

- the melt spreading process on the PWR cavity floor, or on the BWR dry-well floor, in a relatively dry containment scenario

- the melt fragmentation process that occurs when the melt jet is discharged into a water pool

- the melt coolability process, under a water overlayer, that occurs when the unfragmented melt collects at the bottom of the water and attacks the concrete basemat

- the debris coolability process that occurs when the heat-generating fragmented melt particles collect in the bottom of the pool and attack the concrete basemat.

Other objectives are to (a) establish scaling relationships so that the experimental results obtained are appropriate for model validation, and could be extended to prototypical situations, (b) construct phenomenological and/or first-principle computational models for the processes mentioned above, and, (c) validate the developed and the existing models against data obtained in the experiments conducted in this program, and elsewhere.

4. Approach

The approach of the research program is basically experimental, but supported by substantial analysis development activity. The experiments will be performed at more than one scale, and with more than one oxidic mixture melt. The controlling physical parameters, for each interaction studied, will be varied systematically. For example, for the hole ablation experiments, the parameters to vary would be (1) melt superheat, (2) melt viscosity, (3) melt flow velocity through the hole, (4) initial hole size and (5) different melting-temperature wall materials. The extent of parameter variations will be determined through the scaling and sensitivity analysis, performed concurrent with, or prior to, experiment planning.

For the melt spreading process, the important variables are (i) melt superheat, (ii) melt solidus temperature, (iii) melt interaction with concrete, (iv) water presence, (v) containment cavity configuration (e.g., presence of a sump) and (vi) melt thermophysical properties.

For the melt-water interaction experiments, the parameters of interest are (a) melt superheat, (b) melt viscosity, (c) melt surface tension, (d) melt density, (e) melt jet diameter, (f) water subcooling, (g) water depth, and perhaps, (h) system pressure. These experiments will be performed in a tank, capable of withstanding some pressurization. No triggering will be employed, since the study of steam explosions is not an objective.

For the melt coolability with a water overlayer experiments, the approach will be to perform tests, similar to the MACE tests [14], with provision of electrodes to supply the equivalent of decay heat to the oxidic melt, which can be poured in the test section from the furnace. Experiments may be performed with water entry from the bottom, the coolability mode advocated in Germany for the proposed core catcher [15]. The coolability experiments will have a gas supply system to simulate the gases generated during concrete ablation by corium. The gas flow rate will be made proportional to the temperature of the melt. The parameter variations for coolability testing could be (a) the size of the test, (b) the depth of the melt, (c) the gas flow rate, (d) the water addition time, (e) the initial superheat of the melt and (f) the melt viscosity variation with temperature.

The experiments for the coolability of a particulate debris bed under water should simulate particulates formed during the melt-water interaction experiments. The attempt will be to build a bed, with a conical shape, having smaller size particles on top. This bed should include electric heating wires to provide the decay heat to the debris bed. The parameters of interest are, (i) the particle size and their variations along the depth of the bed, (ii) the specific heat input, (iii) the temperature reached before water addition and (iv) the three dimensionality of the system.

Conceptual drawings are shown in Figures 1 to 5 for the experiments on the vessel melt retention, melt spreading, melt-water interaction, melt coolability with a water overlayer and the particulate debris bed coolability.

5. Melt Material Employed in Tests

Persistent concerns about the experiments that represent severe accident interactions relate to their (a) cost, (b) scale and (c) prototypicality. In general, a prototypical (UO_2 - ZrO_2 - Zr melt) severe accident experiment costs large sums of money and, therefore, such experimental programs have to be supported by a consortium of several nations. The examples are the ACE/MACE program, the FARO Program, each of which have cost, or will cost, several million U.S. dollars. The large scale MACE M3 test is projected to cost approximately 1.2 million dollars. To save costs and avoid radiation hazard, some of the severe accident experiments are performed with the simulant material: iron-alumina thermite melt. This material has been used at various scales ranging from a few kg as e.g., in the Sandia hole ablation experiments [3] and the Fauske-Associate melt-water interaction experiments [16], to several tens of kg as e.g., in the Sandia direct containment heating (DCH) experiments, to several hundreds of kg as e.g. in the CORVIS melt-vessel interactions project. Molten thermite material is a mixture of iron and alumina at 2800 K; thus the iron is at very high superheat, while the alumina is at low superheat. Thermite also segregates, right after it melts, due to the very different densities of iron and alumina. Without separating the oxide and the metallic components, there are difficulties in interpretations of experimental results, because of differences in the superheats and densities. Understandably, the superheat and segregation are very important parameters in melt-structure-water interactions, since they affect most of the phenomena, e.g., hole ablation, melt fragmentation, steam explosion, spreading, coolability etc. Recently, Al_20_3 melt from thermite has been reparated from the iron melt and has been used in various melt interaction experiments. Unfortunately, it has been found that the interaction of molten Al_20_3 with water is very different than that of UO_2 - ZrO_2 melt.

The melt material proposed for the present experimental program is a simulant material; it's choice was based on a number of considerations, some of which are listed in the following:

(a) the corium melt is primarily an oxidic mixture (UO2 - ZrO2) except for having some metallic content (Zr, S.S.)

(b) the corium-structure-water interactions involve the passage of corium from a liquid to the solid state. During the transition, the corium properties e.g. thermal conductivity, surface tension and viscosity change drastically, since they depend not only on the composition, but also on the solid (particulate) content of the corium melt as it cools down.

(c) The corium melt interactions with water involving melt fragmentation and/or steam explosion, depend on the processes of film boiling and radiation heat transfer.

(d) The corium interactions with concrete involve addition of miscible silicon and other oxides from the concrete to the corium melt. This process changes the the character of the melt drastically, e.g., it's viscosity increases by orders of magnitude and it becomes a non-newtonian (shear stress not equal to a constant viscosity times the rate of change of velocity) fluid [17]. The changes in the melt properties affect the heat transfer to concrete, and to a water overlayer, if melt coolability is attempted by addition of water. The crust properties of thermal conductivity and structural strength determine, respectively, it's influence on heat transfer and it's stability. Both of these are a function of the melt composition, which is a mixture of oxidic materials from the original corium and the oxidic materials from concrete.

The above phenomenological and material considerations led to our search for a mixture of oxidic materials with the following attributes:

- melts at relatively high temperature so that the radiation heat transfer and film boiling phenomena are present in the interactions

- can include some metallic components

- has properties, in particular, viscosity and thermal conductivity, which have magnitudes and temperature variations similar to those for UO_2 - ZrO_2 or UO_2 - ZrO_2 - concrete mixtures

- the mixture is inert, cheap and easy to handle

- there is an experience base, and infrastructure, for melting large quantities of the mixture and working with the melt

- there is an experience base pertinent to the experiments envisaged in this research program

- the developmental work, necessary to perform the envisaged experiments, successfully, is not exorbitantly expensive and long-lasting.

Our choices are binary oxidic mixtures which melt in the range of 1000 K to 1700 K. It is possible to use a variety of mixtures tailored to (a) specified differences between the liquidus and solidus temperatures, (b) specified viscosity and thermal conductivity values and their temperature variations. These mixtures are relatively cheap, and there is a very large commercial experience-base in Sweden on handling and working with these materials in the glass industry.

We have employed a mixture of $PbO + B_2O_3$ for initial scooping experiments. The toxicity of PbO required special handling and we have discarded the use of PbO. Instead, we have used mixtures of $CaO + B_2O_3$ with different proportions and mixtures of $ZnO + B_2O_3$. Phase diagram of those mixtures are shown in Figures 6 and 7. The properties of these mixtures are being measured. The currently available data is shown in Figure 8 and in Table 1.

6. Facilities

There were no facilities to perform nuclear power safety research at the Division of Nuclear Power Safety at KTH, until late 1994. The facilities were constructed in an experimental hall obtained from the KTH administration. A 880 KVA power supply was installed to provide the power needed for the various experiments envisaged. The water and the compressed air supply were provided. An efficient and large-capacity ventilation system was constructed, in order to exhaust the gases that may be produced in the melt-creation processes. An induction furnace with a coil to provide upto 35 liters of melt from the mixtures of powdered oxidic materials was purchased and recently installed. Initially, a 5 liter crucible were installed and the initial experiments were performed with that volume of melt. A general view of some of the equipment in the laboratory is provided in Fig. 6.

The laboratory infrastructure was installed, i.e., 1) a machine shop to construct the test sections for the experiments, 2) a welding shop, towards the same purpose, 3) a chemical room, with a ventilated glove box to prepare the oxidic mixtures and 4) the tools, clothing, safety equipment and other paraphernalia needed for an efficient operation of the laboratory. The laboratory is manned by 2 full time technicians and it is equipped with a crane. It also has a pit of dimensions 4 meters x 2.5 meters x 1 meter deep, where melt-vessel interaction and melt spreading experiments will be performed. By the middle of 1997 we intend to build a containment, located on top of this pit, to house the experiments in which the molten oxidic mixture interacts with water, i.e., the melt jet-water interaction experiments, the melt spreading-in-presence-of-water experiments and the melt coolability experiments. The containment will house another induction furnace at its top elevation, in which melt will be prepared to drop into water tanks housed within the containment.

Instrumentation is a focus of development in the laboratory. For visual observations, a video system with a shutter speed capability down to 1/10,000 seconds has been purchased. A similar still camera system has also been purchased. Procurement of an X-ray camera system is under consideration, in order to observe, and identify, interfacial phenomena in melt-jet-water interaction experiments. Additional instrumentation will be obtained as needed.

7. Research Program Progress

The research program started in 1994 and some scoping experiments were performed in the laboratory of the Metal Casting Institute at KTH. However, since the main thrust of the program is experimental, a laboratory had to be constructed. Its construction took much longer than the original estimate and the experimental work started in earnest only in the fourth quarter of 1995. Since, the laboratory construction did not involve many of our staff members, they concentrated on developing models. The emphasis of the research has been on the in-vessel accident progression phase during which the melt is discharged from the vessel through a failure site (hole) and hole-ablation occurs. Additionally, recently some experiments have been performed on the melt droplet fragmentation, during melt-water interaction, in order to identify the influence of the melt properties on the melt fragmentation mechanisms.

The research program is continuing, and from January 1, 1996 is complemented by a program titled "Melt-Vessel Interaction", sponsored by European Union, in which KTH will perform experiments and develop analysis-methodology for the processes of in-vessel melt coolability, in-vessel melt retention, vessel failure and melt discharge. The melt-structure-water interaction program will continue till December 31, 1998, subject to the approval of the APRI Project, U.S. NRC and the Finnish organizations.

8. Research Program Description and Results Up To June 30, 1996

The research program has resulted in many publications. We are presenting here a selection which provides, (i) description of the experimental program and some results on vessel hole ablation and on melt droplet-water interaction; and (ii) description of the analysis models and results dealing with the thermal hydraulic and material behavior occurring during the melt-vessel and melt-water interaction processes. Reprints or pre-prints of nine papers, whose particulars are listed below, are attached here. In the following paragraphs, we will provide summaries of the findings reached in these publications.

A Selected List of Papers Published

[1] T.N. Dinh and R.R. Nourgaliev, "Prediction of Turbulent Characteristics in a Fluid Layer with Internal Energy Sources", Proceedings of the 2nd European Thermal- Sciences Conference, pp.843-850. Rome, Italy, (29-31 May 1996),

[2] V.A. Bui and T.N. Dinh, "Modeling of Heat Transfer in Heat-Generating Liquid Pools by an Effective Diffusivity-Convectivity Approach", Proceedings of the 2nd European Thermal-Sciences Conference, pp.1365-1372. Rome, Italy, (29-31 May, 1996).

[3] V.A. Bui, T.N. Dinh and B.R. Sehgal, "Numerical Modeling of Heating and Melting Processes in Internally-Heated Debris Beds in a Reactor Vessel Lower Plenum", Proceedings of the Fourth International Conference "Heat Transfer-96", in the session 'Advanced Computational Methods in Heat Transfer, Udine, Italy. (8-10 July 1996).

[4] T.N. Dinh, V.A. Bui, R.R. Nourgaliev, and B.R. Sehgal, "Crust Dynamics under PWR In-Vessel Melt Retention Conditions", Proceedings of the 1996 National Heat Transfer Conference, in the session "Scaling and Simulation" Houston, Texas, (August 3-6, 1996).

[5] V.A. Bui, T.N. Dinh, and B.R. Sehgal, "In-Vessel Core Melt Pool Formation during Severe Accidents", Proceedings of the 1996 National Heat Transfer Conference, in the session "Fundamental Phenomena in Severe Accidents", Houston, Texas, (August 3-6, 1996).

[6] B.R. Sehgal, J. Andersson, V.A. Bui, T.N. Dinh and T. Okkonen, "Experiments on Vessel Hole Ablation During Severe Accidents", Proceeding of the Intern. Seminar on Heat and Mass Transfer in Severe Reactor Accidents,

Izmir, Turkey, 1995, Begel House Publ., (1996).

[7] T.N. Dinh, V.A. Bui, R.R. Nourgaliev, T. Okkonen and B.R. Sehgal, "Modeling of Heat and Mass Transfer Processes During Core Melt Discharge From A Reactor Pressure Vessel", Proceedings of the Seventh International Topical Meeting on Nuclear Reactor Thermal Hydraulics NURETH-7, New York, USA, 1995, NUREG/CP-0142, Vol.3, pp.1809-1829. Also in press; Nuclear Engineering and Design, (1996).

[8] T.J. Okkonen and B.R. Sehgal, "Influence of Melt Freezing Characteristics on Steam Explosion Energetics". Proceedings of the Fourth International Conference on Nuclear Engineering (ICONE-4), New Orleans, Louisiana, (March 10-14, 1996).

9. SUMMARY OF RESEARCH RESULTS

The research work performed at KTH, within NKS project, can be divided into three parts, namely, 1) modeling of the in-vessel thermal loading during core melt-vessel interaction, 2) vessel hole ablation and thermal hydraulics of core melt discharge from the reactor pressure vessel, and 3) phenomena of melt-water interactions.

In the first part, model development, validation, and application were performed to analyze core melt pool formation and progression in the RPV lower plenum.

In the second part current understanding of the vessel hole ablation and core melt discharged was advanced by experiments and associated modeling work.

In the third part, freezing behavior and fragmentation of melt particles were studied, numerically, and experimentally.

9. 1 Phenomena of In-Vessel Thermal Loading

New turbulence "data" were generated by direct numerical simulation of the internally-heated fluid layer flow and heat transfer. A new model for core melt pool natural convection heat transfer was developed and validated for steady-state and transient conditions for a variety of boundary and geometry conditions. A numerical method for phase change problems was applied in order to develop a computer code, which can handle solution of 2D conservation equations in the complex domain of the debris and vessel head during the core melt-vessel interaction process. Phenomena of potential importance to the behavior of core melt pool were identified and analyzed. These are crust dynamics and the effect of the mushy-phase properties on melt pool heat transfer. Finally, an integral code was developed to analyze core melt progression in the late phase of melt-vessel interactions. The code enables reactor calculations in a 2D formulation, taking into account the crust behavior, melting of the vessel steel, and natural convection heat transfer in melt pool.

9.1.1. Prediction of Turbulence Characteristics in a Fluid Layer with Internal Energy Sources (Paper No. 1)

The objective of our research program is to investigate heat transfer in internally-heated melt pools under high-Rayleigh-number conditions, which result in turbulent flows. Such a process may occur in a postulated severe nuclear reactor accident, when a decay-heated core melt pool may form. Isothermal rigid boundary conditions are applied to all pool's boundaries, where freezing of core melt occurs. The most notable application envisaged is related to the accident management scheme of external flooding of the reactor vessel to preclude its failure; thereby containing and cooling the melt within the vessel. In such a case, determination of both the local heat flux distribution along the cooled walls and upward versus downward energy splitting are of paramount importance. Major, relevant, experiments were conducted by employing simulant liquids (water, freon), so the data base can only be used to develop prediction models, but not for direct extrapolation to reactor situations.

Furthermore, in a previous study [18], we showed that standard low-Reynolds-number κ - ε models fail to predict heat transfer in turbulent natural convection flows under consideration. In particular, these models fail in describing accurately the heat fluxes to the top and, also, to the bottom surface of the liquid pool.

It was indicated that reliable predictions of the local heat fluxes in the large volumetrically-heated core melt pool would require application of the Reynolds stress models, or the second-order modifications of the two-equation models, for description of the turbulence. Most importantly, anisotropic behavior in stably-stratified and unstably stratified-layers must be modeled.

In this study, we focus the analysis on turbulent characteristics in an internally-heated fluid layer with isothermally cooled top and thermally insulated bottom surfaces. The main idea was to obtain necessary turbulence data from direct numerical simulation (DNS) of a naturally convecting flow, and to analyse major peculiarities of turbulence behaviour under unstable-stratification condition.

Direct numerical simulation of a naturally convecting flow in an internally heated fluid layer, with a constant temperature boundary condition on the upper surface and thermal insulation boundary condition on the bottom surface, was performed for several Rayleigh numbers in the range $5 \cdot 10^6$ - $1 \cdot 10^8$ using finite-difference schemes. The approach enabled the determination of the top wall heat fluxes, the mean temperature fields, the distributions of Reynolds stresses and turbulent heat fluxes.

The study led to the following conclusions:

- The calculated Nusselt number, temperature distribution within the fluid layer and the temperature fluctuations are in good agreement with experimental data of Kulacki and Goldstein [19]. Also, the calculated turbulent heat fluxes agree well with those predicted by the analytical model of Cheung [20].

- Analysis of the calculated turbulent characteristics showed significant anisotropy of turbulent transport properties. In particular, the turbulent Prandtl number was smaller than unity and decreased with increasing Rayleigh number. So, the isotropic eddy diffusion approach can not be used to describe turbulent natural convection heat transfer under unstable-stratification conditions. Furthermore, dissipation time scale ratio R was shown to differ, significantly, from values, accepted for thermal variance equilibrium conditions.

- The turbulence data obtained are important for developing Reynolds stress correlations, and reliable methods, for describing turbulent natural convection heat transfer to the isothermally-cooled upper surface, in an internally heated liquid pool.

9.1.2. Modeling of Heat Transfer in Heat Generating Liquid Pools by Effective Conductivity-Convectivity Approach (Paper No. 2)

During a hypothetical severe accident, in a nuclear reactor, a molten corium pool may form on the lower head of the reactor vessel, as a result of core melt-down. In such a case knowledge of the transient thermal behavior of the decay-heated corium pool is essential for the assessment of the capability of retaining melt inside the reactor vessel by providing cooling from outside, or in the absence of cooling the timing of the vessel lower head failure.

Heat transfer inside a liquid pool, with volumetric heat sources, is driven by natural convection, whose character changes from laminar mode to turbulent, according to the Rayleigh (Ra) number. The natural convection, inside such a melt pool, has a large stratified region on most of lower pool portion, and an intensly-mixed region of unstable-stratification above. The heat transfer to the side wall is, however, governed by the development of the boundary layer of the flow moving downward along the cooled wall.

The aim of this work was to develop a new method for modeling heat transfer in a heat-generating liquid pool, which can reasonably describe the related physical processes and phenomena, and, at the same time, is simple enough, so that it can be implemented in an integral reactor safety code.

In general, the modeling is based on solving the two-dimensional energy conservation equation, while taking into account the effects of anisotropic heat conduction. Effects of natural convection are modeled by means of "pseudo-convective" terms and effective diffusivity coefficients. The thermally-driven effective velocities are calculated using a heat-balance treatment, and experimental correlations of heat transfer coefficients on the cooled boundaries.

In this study, heat transfer in internally heated liquid pools is modeled with a particular emphasis on the validation of the developed method in various geometries, and under different boundary conditions. It was shown, by comparing the calculated results with the available experimental data, that the method could predict, a) fractions of heat removed to the various cooled surfaces of the pool, b) temperature fields within the pool under steady-state and transient conditions, and c) local heat flux distribution on the bottom curved surface of the pool.

It is perhaps instructive to note that, although the method is able to portray the most significant features of natural convection heat transfer in heat-generating liquid pools, it is restricted by the uncertainties, or errors, in the analytical and experimental correlations employed. In this sense, the present model does not provide new physical insights into the heat transfer characteristics in laminar or turbulent internally heated liquid (melt) pools. However, the developed method provides a reasonable technique for determining the characteristics of molten pool during its formation and progression. Thus, the time history of the pool temperature field and the heat fluxes imposed on pool boundaries, can be properly predicted by this robust and efficient modeling approach. Such information is needed for evaluating the mode and timing of vessel failure, the character of the melt discharged in the event of vessel failure, and finally, the potential for retaining the melt, within the vessel, through external cooling of the vessel.

9.1.3. Numerical Modeling of Heating and Melting Processes in Internally-Heated Debris Beds in a Reactor Vessel Lower Plenum (Paper No. 3)

The study considered the two-dimensional thermal processes in internally-heated oxidic debris beds in the lower plenum of a light water reactor vessel, during the course of severe accidents, with core meltdown and relocation. Heat transfer and phase change processes in debris beds and vessel lower head wall were investigated numerically with particular emphasis on the dynamic characteristics of the thermal transients occuring. The main purpose of the work was to develop an appropriate modeling approach, which enables the analysis of complicated physical processes (involving dynamic changes of bed porosity, anisotropic heat transfer in remelting beds with internal energy sources) in the complex domain of a debris bed situated on the vessel lower head wall.

In the present study we developed a computational method, which can be used to integrally analyze the thermal transients occurring inside the debris bed and reactor vessel wall, and to assess several parameters, which influence these transients. These are 1) the configuration of the inhomogeneous core debris bed, 2) the heat generation inside the debris bed and vessel wall, and 3) the thermal interaction between the debris bed and wall. More specifically, the heat transfer processes involve radiation, debris bed melting, formation of the melt pool, pool natural circulation and local melting of the vessel wall. From the "simulation" point of view, it is difficult to rigorously adress all of these coupled processes. The simplified approaches, using the single-point analysis give limited description of the dynamics of the coupled processes and phenomena. Therefore, the development of a modeling approach, which can reasonably describe the physics, and, at the same time, be simple enough to implement in an integral reactor safety code, is a worth-while goal, which was pursued here.

The modeling approach was based on the energy conservation equation, derived for a two-dimensional, general curvilinear coordinate system, while taking into consideration the orthogonal anisotropy of heat conduction inside the debris bed. A multi-block control-volume numerical scheme, for two-dimensional cartesian or cylindrical non-orthogonal geometries, was developed and applied to predict heat transfer in the solid or porous debris beds and the evolving melt pools.

All separate mathematical and physical models of the relevant phenomena were implemented into a computer code, which was then applied to analyze the core debris bed heat up and melting; and the reactor vessel temperatures in a severe accident scenario involving core melt-down and relocation. The natural convection heat transfer in the forming melt pools was described by means of an earlier-developed effective conductivity-convectivity approach.

Calculated results indicate that the modeling approach is efficient and capable of providing a realistic picture of the debris bed heat up and melting inside the lower head of the vessel.

9.1.4. Crust Dynamics under PWR In-Vessel Melt Retention Conditions(Paper No. 4)

In the last few years, severe accident management has come to the fore as a concept to upgrade the safety of the existing and the future nuclear power plants. In particular, the concept of retaining the molten corium within the reactor vessel by external cooling of the vessel, in the event of core melt-down, is chosen as the basic severe accident management strategy for the Finish Loviisa VVER-440 plant and the AP 600 plant.

The physical picture of a corium melt pool retained in the PWR vessel may be described as follows: (a) a solid crust ($T \leq T_{sol}$)will form at the vessel wall; (b) a mushy region will exist between the corium melt pool and the solid crust - in which the properties will be different - in-between those for the solid and the liquid corium; (c) the melt pool whose boundary will be at T_{liq}. In general, the heat flux,directed to the boundary of the melt pool, will be determined by the natural convection processes, occurring in the pool and not by the crust enveloping the pool. However, this is true, if the solid crust layer is stable, and if the mushy region between T_{liq} and T_{sol} behaves like the solid crust i.e., it does not have a circulation flow, which may enhance the heat transfer to the walls, and affect the thickness of the solid crust. The crust dynamics and stability may become important, if the crust thickness ξ_{cr} is small and varying in time. The transient heat conduction and phase change in the crust layer can feedback to the core melt pool's natural convection flow and its temperature. Theoretically, periodic self-sustained oscillations were identified by Cheung [21], who investigated heat transfer processes in an internally heated fluid layer, cooled to freezing from above.

In this study, the thermal hydraulic behavior of the crust and of the mushy layers, which envelop the decay-heated molten corium pool, was investigated. Based on results of umerical simulation and the sensitivity study, some phenomena were identified and analyzed. They are: the transient thermal interaction between the upper crust layer and the unsteady melt flow; the convection in the vertical molten vessel steel layer; the heat transfer and flow in the mushy zone.

It was found that the upper crust, though thin, is thermally stable, whereas the existence and stability of the side ward crustare sensitive to the convective heat transfer in the vertical molten-vessel steel layer. The flow and convective heat transfer in the mushy zone of the crust layer are found to have both stabilizing (from the hydrodynamic point of view) and destabilizing influence (from the thermal point of view) on crust dynamics. The significance level of these effects in the prototypic accident cases is, however, unclear, since they strongly depend on a corium property, namely the mushy-phase permeability coefficient, which is unknown. Only experimental observations can provide information, with which further assessments could be made.

9.1.5. In-Vessel Core Melt Pool Formation during Severe Accidents (Paper No. 5)

In this study a model to describe the debris bed heat-up process, occurring in the lower head of an LWR vessel, during the course of a severe accident is developed and applied. The model treats the case of a uniform composition, initially quenched, debris bed of zero porosity, which is slowly converted into a melt pool. The hemispherical lower head wall is included in the modeling and its melt-through due to the thermal attack of the melt pool is calculated. The model is based on the solution of the two-dimensional, general curvilinear geometry, energy equation. The anisotropic heat diffusion is modeled, and the heat transport in, and at the boundaries of, the developing melt pool, undergoing natural convection, is described in a subsidiary model. In this sub-model, the heat transport to the upper boundary is through the upward movement of plumes (or layers), whose average velocity is calculated to deliver the requisite heat flux at the upper boundary. The heat transport to the hemispherical boundary is through conduction and then through a boundary layer created by the downward flow along the curved wall from the upper part of the pool. Thus, the temperatures within the pool are calculated. A melt pool is created after the liquidus temperature (appropriate for the melt composition) is exceeded. The vessel melting and melt-through is calculated by following the temperatures in the vessel wall. No structural calculations were performed.

The model was applied to the BWR scenario of lower head melt pool formation, and vessel melt-through, as an illustration. The heat sinks of the control rod guide and instrumentation tubes were ignored. Also ignored was the presence of any Zircaloy in the BWR debris, which may lead to chemical energy addition.

The calculation showed that due to the relatively low heat conductivity of the core debris, the effect of the cold boundaries does not extend far into the debris bed. Thus, the heat up process is quite coherent for the debris bed. First, a mushy state is reached and, then, a molten state is reached, almost simultaneously, for a substantial fraction of the debris bed volume. The heat-up process would be coherent for a larger fraction of the debris volume in a PWR, since it has a relatively smaller surface/mass ratio than for the BWR lower head.

It was found that the thickness of the crust (debris) around the pool does not affect the fractions of the heat generated, going to the top and sideward boundaries. It confirms the physically-intuitive observation that the heat flows to the boundaries are directed by the natural convection processes in the melt pool. The crust simply acts as a boundary condition at the liquidus temperature to the melt pool.

There are, currently, many simplifications and assumptions in our models e.g., no chemical reactions, zero porosity, uniform composition etc., which will affect the results calculated here. We envision further development of this model to remove some of the assumptions and approximations made. The models developed here, nevertheless, represent the thermal hydraulic processes quite well and could be incorporated in the codes describing the overall progression of a severe accident.

9.2. Vessel Hole Ablation and Core Melt Discharge

The failure of a light water reactor vessel may occur if the severe accident progression proceeds unchecked, without cooling of the melt that may be attacking the lower head. The vessel pressure level is important in identifying the mode of the failure of the lower head. For the PWR high pressure scenarios it is likely that the lower head wall, raised to high temperatures (>800°C) due to the melt attack, may creep and eventually fail. This failure mode: creep-rupture; may take 1 to 3 hours to progress. In general, substantial thinning of the vessel will take place. In the absence of high pressure e.g., through the accident management action of depressurization in a PWR, creep rupture will not take place. Creep rupture is not likely for a BWR, since the automatic depressurization system (ADS) is an integral part of BWR operations and accident management. However, in the BWR accident scenario, in which a core melt pool forms from the quenched debris bed (after a few hours) the thermal loading is intense enough to raise the vessel temperature to near the melting point. At which time some creep of the vessel wall may occur due to the mass loading of the melt in the vessel.

Another vessel failure mechanism identified is that of penetration failure. This failure may occur in both PWRs and BWRs, releatively rapidly, if a melt pour from the original boundary of the core on to the lower head wall, lands on the weld holding the instrument tube (or a control rod guide tube in a BWR) in the vessel. In general, this is not so likely. Penetration failures can occur, later, when the thermal loading in a dry vessel becomes locally large enough to subject the welds to temperatures higher than the weld melting temperature.

In all of these vessel failure modes, an initial failure site ablates as the melt is discharged through it. The failure hole ablation (and increase of failure size) is a very rapid process. It is estimated that the vessel melt pool may be discharged in the time span of 15-50 seconds. Thus, the hole ablation process is 2 to 3 orders of magnitude faster than the vessel creep rupture and the melt pool formation processes. During the melt discharge process, the vessel pressure also goes down to the containment pressure level in 15-50 seconds, and the creep process essentially stops after the melt discharge process has begun.

The vessel hole ablation and the melt discharge processes determine the mass rate of melt attacking the containment. In this sense, the containment loading rate is a direct function of the vessel melt discharge rate; thus the containment integrity evaluations are also subject to the correct prediction of these two in-vessel processes. Additionally, if the melt discharge from the vessel, encounters a pool of water, as it does for Swedish BWRs, due to the accident management scheme of flooding the containment when there is the possibility of a core melt accident, a large steam explosion could occur, whose dynamic loadings may also be of concern for containment integrity. The intensity of the steam explosion loading also depend upon the melt jet mass participating in the explosion process, which is a function of the melt mass flow rate as a function of time. Thus, the correct prediction of the hole ablation and of the melt discharge processes is essential for the prediction of steam explosion loads.

We have investigated the vessel hole ablation, and the melt discharge processes, experimentally by employing simulant materials, and analytically by modeling the heat and mass transfer process during core melt discharge. The modeling is based on the observations obtained during the experiments, and resulted in a model, named HAMISA (hole ablation modeling in severe accidents). Papers No. 6 and 7, respectively, describe, the scoping experiments that were performed and the models that were developed.

9.2.1 Experiments in Vessel Hole Ablation During Severe Accidents (Paper No. 6)

In this paper, results obtained in a set of experiments investigating the hole ablation process are reported. A capability has been established at the nuclear safety laboratory of the Royal Institute of Technology to perform the melt interaction experiments using a simulant mixture of oxides heated to melting temperatures. In the first set of experiments, a mixture of $Pb0+B_20_3$, which melts at around 800°C, has been used. Superheats of upto 200°C can be easily accomplished.

The hole ablation experiments were performed with approximately 35 kg of the $Pb0+B_20_3$ melt, interacting with the lead plates, which melt at 327°C. The initial temperature of the melt was in the range of 900 to 1000°C. Thus, the temperature difference between temperature of melt and the plate melting temperature were in the range of 600 to 700°C, which is also typical for the prototypic scenarios. The thickness of the lead plate (representing the vessel wall) was varied, for these experiments, between 20 mm and 40 mm, with an initial hole size of 10 mm. A scaling analysis was performed based on the one-dimensional hole ablation model developed by Pilch. Pilch did not account for the movement of melt crust formed at the surface of interaction with the plate. We believe that the main question in the hole ablation process is whether a crust, formed on the melting vessel wall, and subjected to the melt flow, will remain stable or not. Periodic sweeping out and reforming of the crust may be the operative mechanism. A primary objective of our hole ablation experiments was to delineate the role of crust, since if the crust is stable the final hole size is $\approx$ 50% of the final hole size for an unstable or absent crust.

The first set of experiments showed the presence of a crust layer, which seemed to persist throughout the hole ablation (i.e., the melt discharge) process. The 10 mm hole enlarged to a 60 mm hole for the case of the 20 mm plate. The hole ablation process was found to be 2 dimensional.

Comparison of the data measured to the results of the HAMISA model developed showed good agreement. Further experiments on the hole ablation process with a melt made from a different oxidic mixture, and with different material plates to represent the vessel wall, are planned.

9.2.2 Modeling of Heat and Mass Transfer Processes During Core Melt Discharge (Paper No. 7)

In a light water reactor core meltdown severe accident, the molten core material could cause a failure of the lower head of the reactor pressure vessel (RPV), if sufficient internal or external cooling of the vessel could not be provided. Depending on the vessel design and accident conditions, the lower head integrity could be lost due to a global or a local creep rupture of the lower head wall, or, - if the lower head had penetrations - a local penetration failure, Rempe et al., [2]. The initial failure site will enlarge rapidly, due to heat transfer from the ejected melt (corium), which is at a much higher temperature than the vessel wall melting point. Melt-induced loads on the containment and any further accident progression - involving interactions between core melt and the coolant, structures and atmosphere in the reactor cavity of a pressurized water reactor (PWR), or in the pedestal (lower drywell) and suppression pool of a boiling water reactor (BWR) - would largely depend on the melt ejection characteristics.

Melt ejection and lower head ablation experiments, using an oxidic melt material ($Tf \sim 1000$-$1500K$), discharged from a vessel, with a low-melting-point metallic lower head ($T_{v,mp}$ ~600-900 K), are underway at the Royal Institute of Technology (KTH), Stockholm. Until now we have employed the oxidic melt mixture PbO-B_2O_3 (80-20 wt%). It has a melting point of about 900K and its melt-phase viscosity of about 0.1 Pa.s increases with solidification, a characteristic of the core melt as well. In the scoping tests on vessel ablation, pure lead with a melting point of 600K has been used as the lower head wall material. The integral scaling is based on the analysis by Pilch [3]. It was found that we need melt volumes of the order 10-100 liters to reach similitude to prototypic conditions, in which the initial lower head failure site flow rate is small compared to the vessel melt contents. In the scoping experiments that we have performed, so far, with melt volumes of about 3-7 liters, the melt has a substantial superheat and the lead plate thickness varied in the range of 2-4 cm (Paper No. 1). A detailed phenomenological model has been developed to support experimental design, and to analyse the results obtained.

For reactor safety analyses and accident management considerations, the primary interests are the *hole growth dynamics* ($D_{hole}(t)$ and *melt discharge flow parameters* (melt flow rate, superheat, composition). The phenomenological considerations are built around three key elements: the thermal-hydraulic behavior of the core melt in the vessel lower head, the fluid dynamics and heat transfer of the melt flow in the ablating hole, and the thermal and physical (phase-change, mass-transfer) response and feedback of the lower head wall.

The objective of this work is to study heat and mass transfer processes related to core melt discharge from a reactor vessel in a light water reactor severe accident. The phenomenology modeled includes (1) convection in, and heat transfer from, the melt pool in contact with the vessel lower head wall; (2) fluid dynamics and heat transfer of the melt flow in the growing discharge hole; and (3) multi-dimensional heat conduction in the ablating lower head wall.

During the core melt discharge, the convective heat fluxes (from melt flow to discharge hole boundaries) are the driving mechanisms for vessel wall ablation. Thus, the heat transfer characteristics of a laminar entry region in experiments, and those of a turbulent entry region in prototypic situations, have to be analysed in an accurate manner. Based on a tentative identification, ranking and evaluation of related physical phenomena, the most important phenomena are found to be (1) crust formation and relocation dynamics, (2) temperature dependence of melt properties, and (3) the multi-dimensional heat conduction and ablation front propagation in the vessel wall beneath the crust.

The basic objective of model development was to study the scalability of experimental results, and the uncertainties inherent in such extrapolation, due to those in the modeling and the data. In order to ensure direct applicability of the data obtained, the prototypicality of the experimental behavior of the melt flow, heat transfer, wall behavior and crust integrity has to be established. Since this is hard to achieve, we must address the scaling distortions in our tests and their relevance to the reactor case. Analytical modeling helps considerably in this task. Separate effects data are employed to validate analytical modeling. The models employed whenever reasonable - only first-principle formulations, or well-supported assumptions on physical mechanisms. Calculated results guided the applicability of available correlations for heat transfer and friction, under prototypical and experimental conditions of interest. Furthermore, new or modified correlations can be introduced in the integrated model HAMISA (Hole Ablation Modeling In Severe Accidents) developed in this work.

Specifically, studies were performed to investigate thermal hydraulics of core melt pool and its interaction with the crust and vessel structure during core melt discharge processes. The so-called phenomenon of gas blowthrough was numerically studied and an empirical correlation of gas blowthrough-onset criterion was examined and recommended for use in relevant calculations.

Effect of entrance region on hydraulic and thermal characteristics of flow-wall interaction in the discharge hole were numerically examined in laminar and turbulent flow regimes. Calculations, using the mechanistic models developed, have confirmed the effects of core melt momentum and heat transport properties (μ, κ) and their temperature dependence. The current modeling has also highlighted the importance of the wall thickness and thermal properties in the scaling considerations for the hole ablation experiments. Further progress in model development and validation relies on analysis of further hole ablation experiments. The HAMISA model, when validated, will be valid for prediction of the hole ablation dynamics during the melt discharge process in prototypic reactor accidents.

9.3. PHENOMENA OF MELT-WATER INTERACTION

9.3.1. Influence of Melt Freezing Characteristics on Steam Explosion Energetics (Paper No. 8)

Dynamic shock loads, which determine the immediate behaviour of structures enclosing the steam explosion zone in a light water reactor (LWR) vessel or cavity, have recently appeared as a focus of steam explosion modelling. At the same time, the initial conditions of interest have been extended from nearly saturated (in-vessel) to highly subcooled (ex-vessel) coolant conditions, with new limiting mechanisms coming into play. Additionally, the thermal energy of the melt particles fragmented by the explosion wave cannot be assumed to be mixed instantly throughout the bulk coolant (even locally), inasmuch as the melt-coolant premixtures are typically quite lean in fuel. On the other hand, the melt-coolant premixing in a deep, subcooled, water pool can lead to relatively fast freezing of the melt particles, hence limiting the maximum thermal energy available for the explosion process. Such dynamical processes within the coolant and the melt phase have to be considered with care before the model predictions can be applied to reactor cases.

In this paper the focus is on the melt freezing behaviour. The approximate time scales of melt freezing are first considered by assuming a uniform temperature profile inside the melt particle. The conditions, under which melt freezing could be limited by internal conduction, were also examined. Several conclusions were obtained as results of this study.

- The quenching (freezing and cooldown) of melt particles should be one of the major factors affecting the ex-vessel steam explosion loadings. Solidified melt particles cannot take part in an explosion, and, consequently, the time scales of freezing are of primary interest. The quenching depends, first of all, on the surface heat fluxes and any other heat sources such as exothermic metal oxidation. Approximate freezing time scales were estimated, but it was also found that the neglect of internal conduction limitations may lead to an underestimation of the freezing times. Transient conduction analyses were performed to explore potential conduction effects, which depend on the particle size and properties. When considering the importance of internal conduction, one should also note that the surface shell includes most of the sphere mass, and that shock-wave-induced fragmentation may be resisted prior to complete freezing.

- The explosive melt fragmentation behaviour may, indeed, depend on the state of the melt particle just prior to shock wave-induced acceleration. A mushy particle can be particularly "stiff" due to internal crystal formation and subsequent increase in effective surface tension and viscosity, while a mostly liquid droplet can only resist moderate forces without fragmenting. It appears prudent to expect differences between three basic configurations: (i)a superheated metal-type melt droplet, (ii) an oxide-type melt particle with a solid crust and a liquid core, and (iii) a mixed-type (binary, ternary) melt particle with a liquid core, an intermediate mushy region and some crust on top. The transitions between these categories depend on material properties and the thickness of the solid and mushy layers.

- We believe that the high surface heat fluxes, the relatively low initial superheats, and the strongly temperature-dependent properties of Corium could be the key to the recent observations in the KROTOS tests (no explosions, yet, with Corium). With binary melt mixtures, the properties change continuously during freezing, in contrast to pure melt materials which exhibit "sudden" solidification. Single droplet experiments should be performed to understand fragmentation of the mixed-type melts, both before and during the explosion propagation phase. With additional data on the time scales that can make the melt particles non-explosive, or, at least, more resistant to fast fragmentation, the freezing models could be employed to predict ex-vessel reactor situations.

Needless to say, also the properties of various core melt mixtures, the pre-explosion particle sizes, as well as the vessel melt release conditions, are crucial for the estimates on ex-vessel steam explosion energetics.

10. Concluding Remarks

This research program was initiated to address several issues of large uncertainties found in the APRI study. Both analysis-development and experiments were performed in order to advance the current understanding of associated process and phenomena. These studies are continued in the current research program at KTH, which includes jet fragmentation experiments and analyses, film boiling experiments and analyses, and experiments and analyses on other phenomena of melt-vessel interactions.

References

1) Sehgal, Some Outstanding Issues in Severe Accident Containment Performance", Proceedings of the Fourth International Topical Meeting on Nuclear Thermal Hydraulics, Operations and Safety, Taipeh, Taiwan (April 7-8, 1994)

2) J.L. Rempe et.al., "Light Water Reactor Lower Head Failure Analysis", NuREG/CR-5642, EGG-2618, (October 1993)

3) M.M. Pilch, "Continued Enlargement of the Initial Failure Site in the Reactor Pressure Vessel", Appendix J in the Report: M.M. Pilch, H. Yan and T.G. Theofanous, "The Probability of Containment Failure by Direct Containment Heating in Zion", NuREG/CR-6075; SAND 93-1535 (June 1993)

4) H. Hirschmann, H.M. Kottowski, Ph. Tipping, "CORVIS Achievements and International Collaboration", Proc. of Workshop on Large Molten Pool Heat Transfer NEA/CSNI/R (94) 11 (1994)

5) D. Magallon, "Summary of FARO Experimental Results", presentation at the FARO-LWR Expert Group Meeting (Jan. 24, 1995)

6) O. Kymäläinen et.al., "Heat Flux Distribution from a Volumetrically-Heated Pool with High Rayleigh Number", Proceedings of the Sixth International Topical Meeting on Nuclear Reactor Thermal Hydraulics, NURETH-6, Grenoble, France, (October 5-8, 1993). Also in Nuclear Engineering Design 149, 401 (1994)

7) T. Speis and V. Asmolov, " RASPLAV: Refining RPV Integrity Strategies for Accident Management", Nuclear Europe World Scan (Sept. 1995)

8) J. Sugimoto, Personal Communication

9) J.M. Veteau and R. Wittmaack, "CORINE Experiments and Theoretical Modeling", FISA-95 Symposium, EU Research on Severe Accidents, Luxembourg (20-22 Nov. 1995)

10) B.R. Sehgal et.al., "MACE Project Overview", Proceedings of the OECD Meeting on Core Debris Concrete Interaction, Karlsruhe Germany (April 1992)

11) V.K. Dhir, "Procedings of the Sixth Information Exchange Meeting on Debris Coolability, EPRI NP-4455 (March 1986)

12) F.P. Tsai and I. Colton, " Dryout of a Multi-Dimensional Porous Bed" in EPRI NP-4455 (March 1986)

13) T.J. Okkonen, T.N. Dinh, V.A. Bui and B.R. Sehgal, "Quantification of the Ex-Vessel Severe Accident Risks for the Swedish Boiling Water Reactors", Project Report for APRI, SKI Report

14) B.R. Sehgal et.al., "ACE Program Phase D: Melt Attack and Coolability Experiments (MACE)", Proceedings of the Second OECD/CSNI Specialist Meeting on Core Debris Concrete Interaction, Karlsruhe, Germany (April 1-3, 1992) and M. Farmer, B. Spencer and B.R. Sehgal, "MACE Core Coolability Test MIB", Transactions ofthe Twentieth Water Reactor Safety Information Meeting, Washington D.C., USA, NuREG/CP-0125 (Oct. 1992)

15) W. Tromm, H. Alsmeyer, M. Buerger, W. Widmann and M. Buck, "COMET Experiments and Theoretical Modeling", FISA-95, Symposium, EU Research on Severe Accidents (20-22 Nov. 1995)

16) R.J. Hammersly and R.E. Henry, "Experiments to Address Lower Plenum Response under Severe Accident Conditions", EPRI-TR-103309 (1994)

17) M.F. Roche, D.V. Steidel, L. Liebowitz, J.J. Fink and B.R. Sehgal, "Viscosity of Corium Concrete Mixtures at High Temperatures ACE-TR-C-37 (Feb. 1994)

18) T.N. Dinh and R. Nourgaliev, "On Turbulence Modeling of Large Volumetrically Heated Liquid Pools", Nucl. Engineering Design; 1995, to appear

19) F.A. Kulucki and R.J. Goldstein, Thermal Convection in a Horizontal Fluid Layer with Uniform Volumetric Energy Sources. J. Fluid Mech. Vol. 55, part 2, 271-287, (1972)

20) F.B. Cheung, S.W. Shiah, D.H. Cho and M.J. Tan, "Modeling of Heat Transfer in an Horizontal Heat-Generating Layer by an Effective Diffusivity Approach. ASME HTD-Vol. 192, pp. 55-62, (1992)

21) F.B. Cheung, "Periodic Growth and Decay of a Frozen Crust over a Heat Generating Liquid Layer", ASME J. Heat Transfer, Vol. 103, pp. 369-375 (1981)

22) Kondo et.al., "Experimental Study on Simulated Molten Jet-Coolant Interactions, "Nuclear Engineering and Design", 155 pp 73-84 (1995)

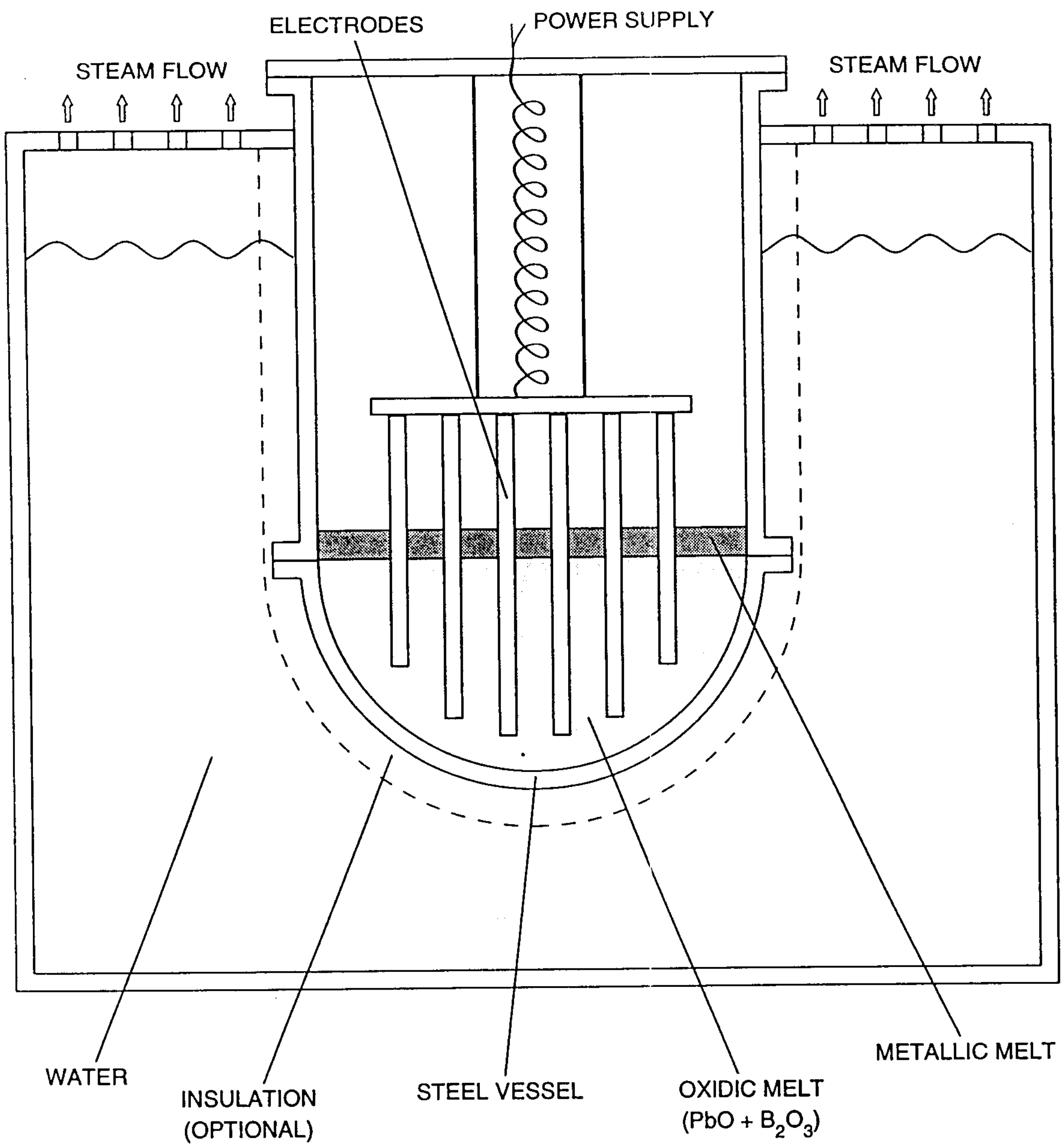

Figure 1. *Vessel Melt-Retention Experiment*

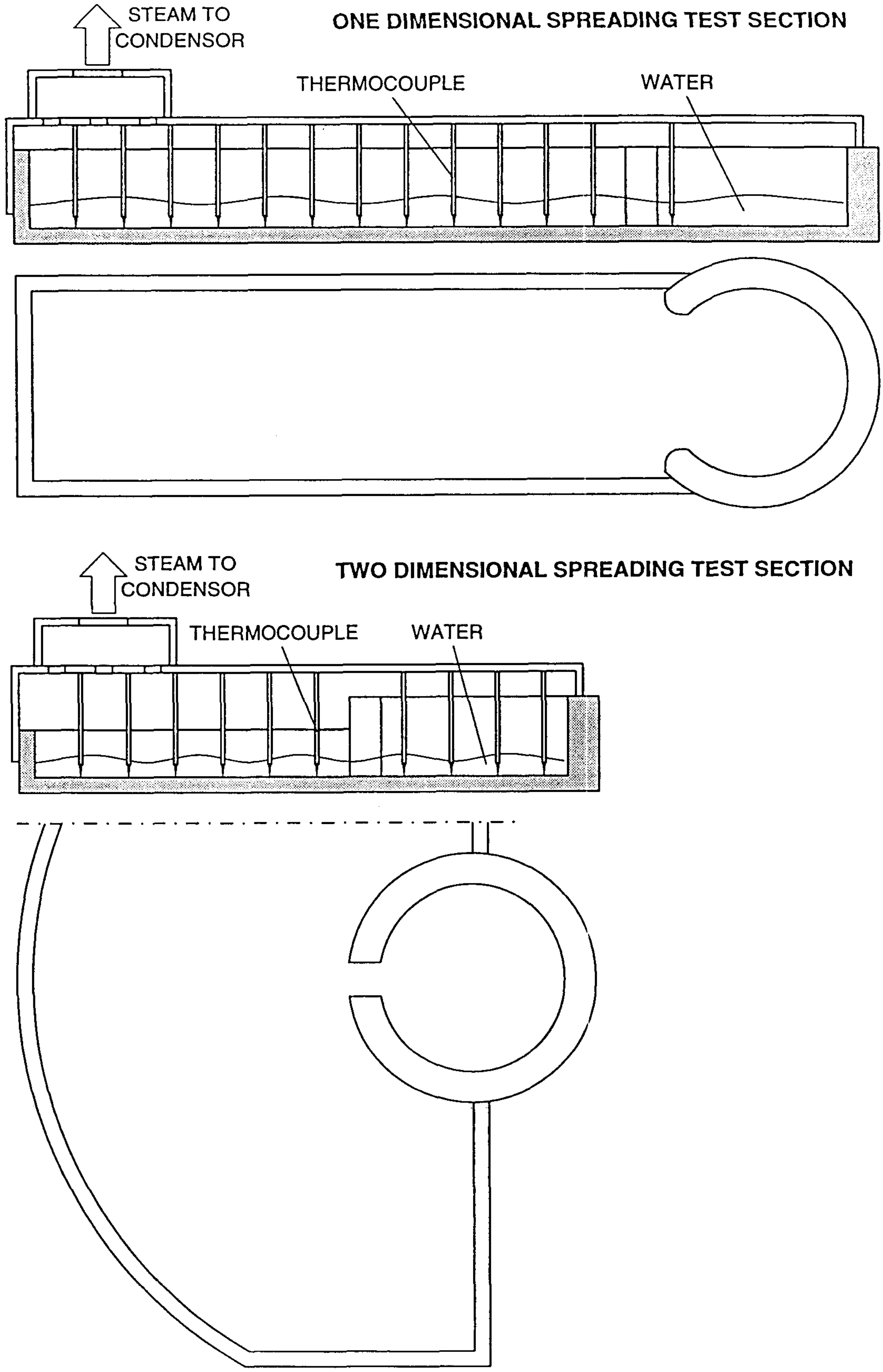

Figure 2. *Melt Spreading Experiments*

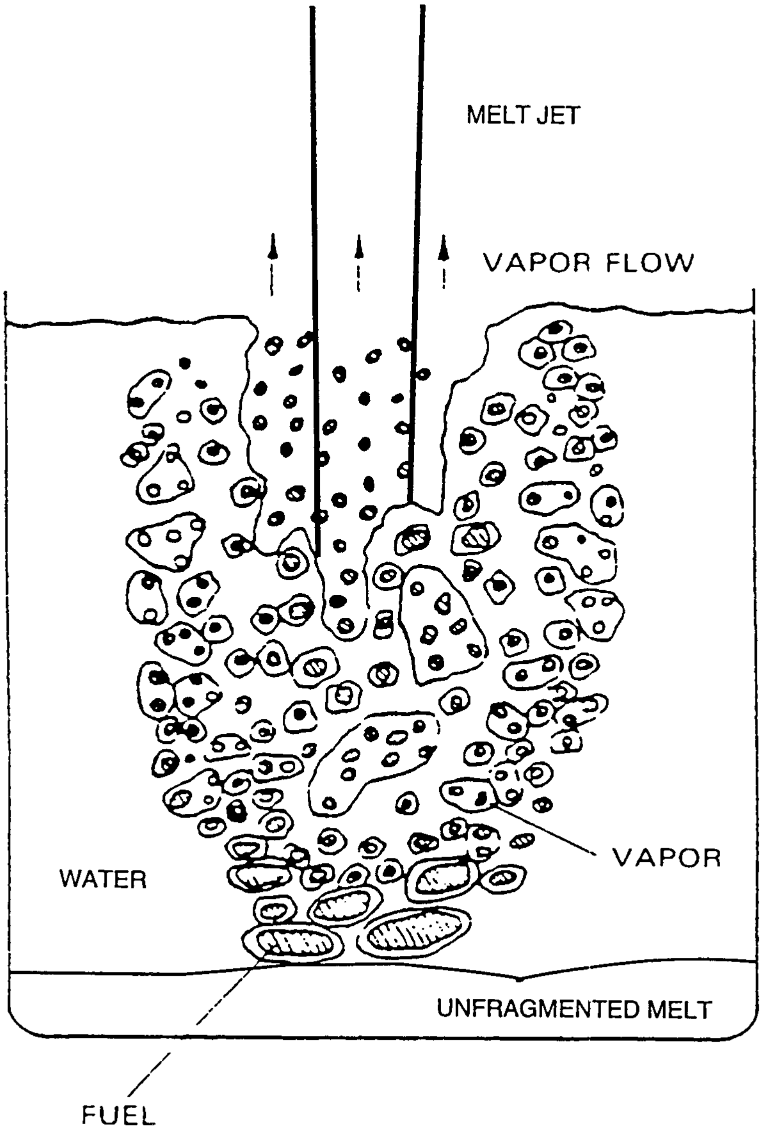

Figure 3. *Melt Jet - Water Interaction Experiment*

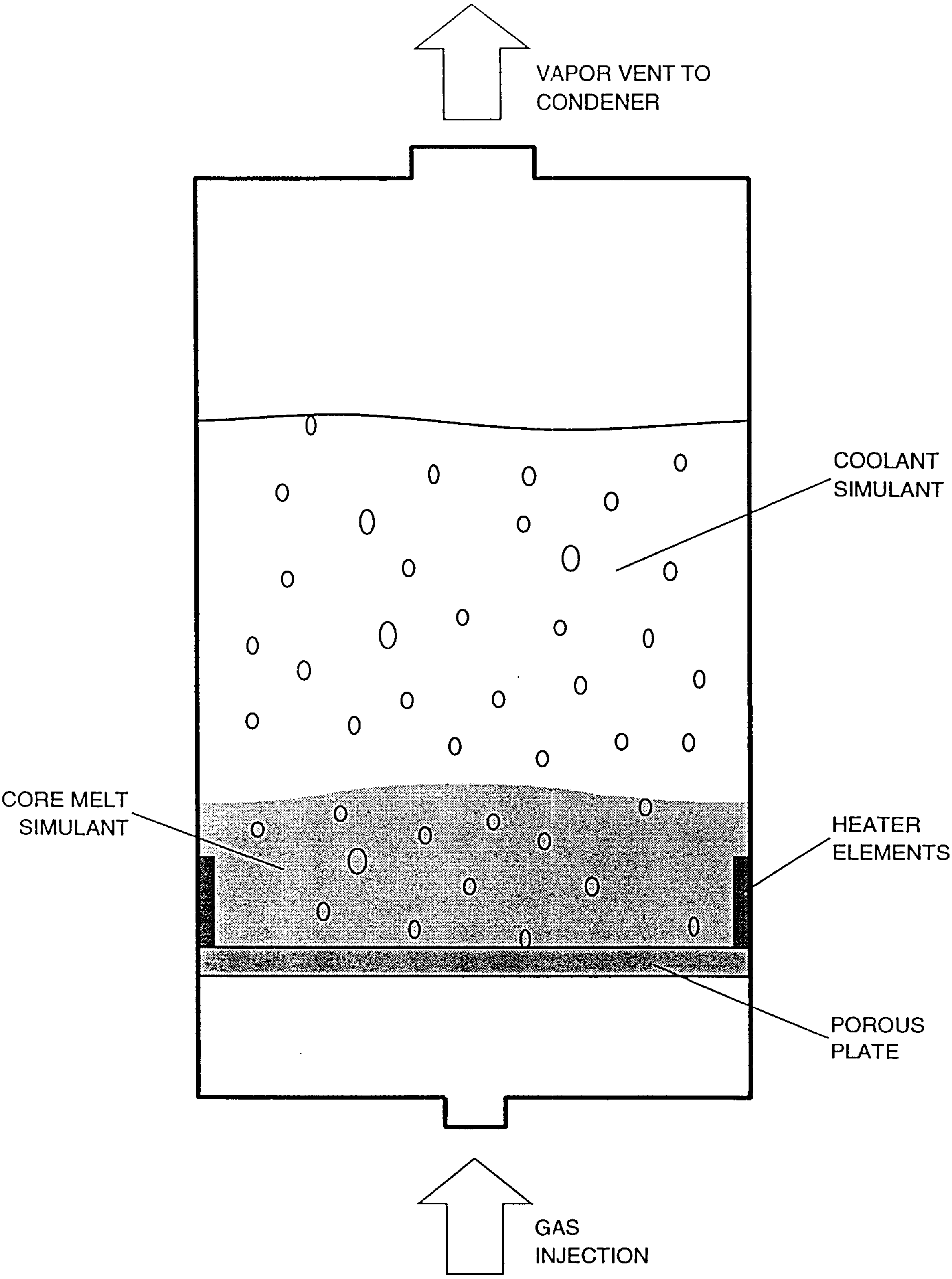

Figure 4. *Melt Pool Coolability Experiment*

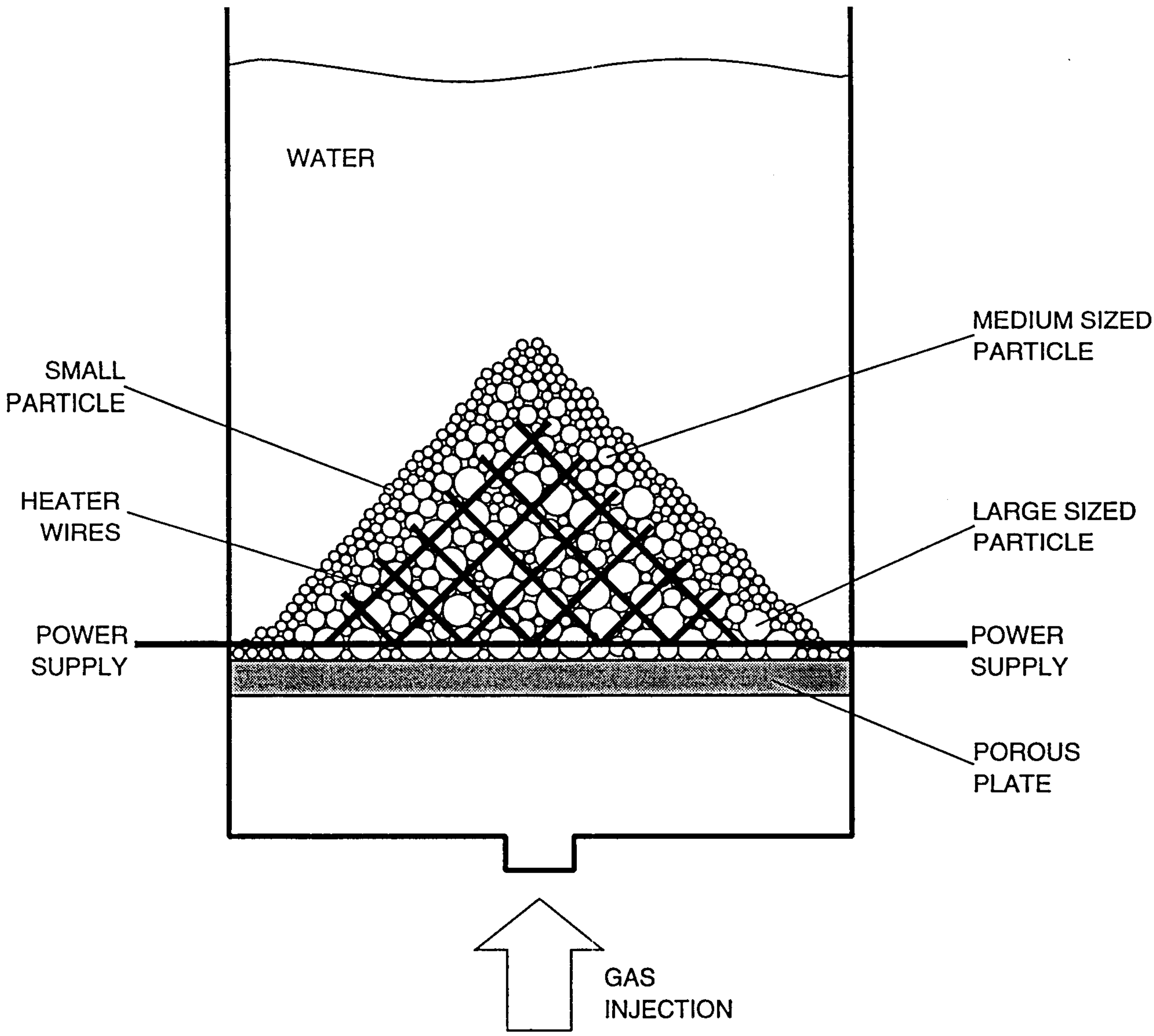

Figure 5. *Debris-Bed Coolability Experiment*

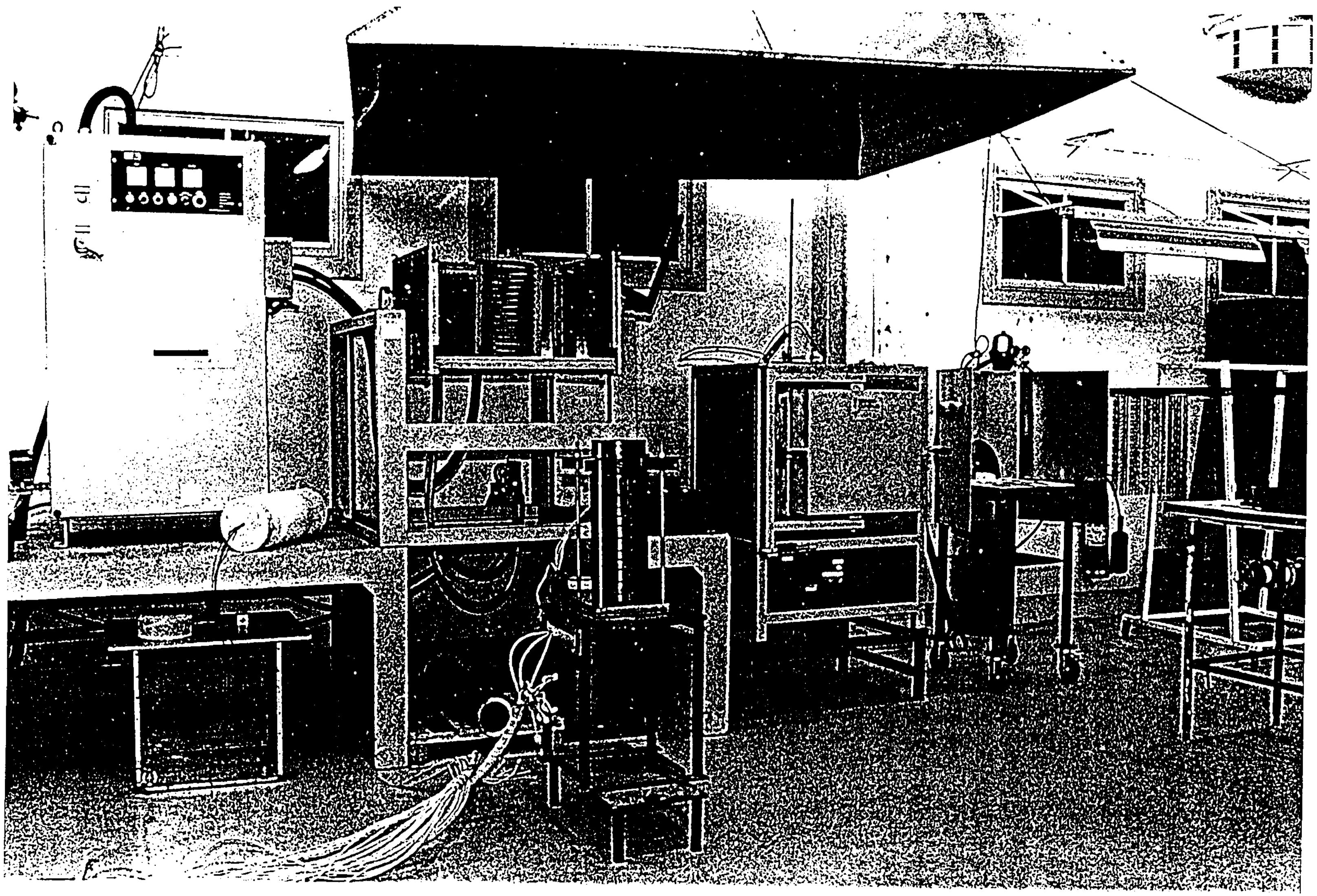

Fig. 6

Paper No. 1

PREDICTION OF TURBULENT CHARACTERISTICS IN A FLUID LAYER WITH INTERNAL ENERGY SOURCES

T.N. Dinh and R.R. Nourgaliev
Royal Institute of Technology, Division of Nuclear Power Safety
Brinellvägen 60, 10044 STOCKHOLM, SWEDEN

ABSTRACT

The paper presents results of numerical prediction and analysis of turbulent natural convection heat transfer and flows in an internally heated fluid layer with isothermally cooled top and thermally insulated bottom surfaces. Calculated turbulent characteristics indicate inadequacy of gradient diffusion approach for problems in question. Useful data needed for Reynolds-stress modeling of natural convection in unstably stratified region have been obtained and discussed.

1. INTRODUCTION

The objective of our research program is to investigate heat transfer in internally heated liquid pools under high-Rayleigh-number conditions, involving a turbulent flow regime. Such a process takes place in severe nuclear reactor accidents, in which a decay-heated core melt pool may form. Isothermal rigid boundary conditions are applied to all pool's boundaries, where freezing of core melt occurs. The most notable application envisaged is related to the accident management scheme of external flooding of the reactor vessel to preclude its failure; thereby containing and cooling the melt within the vessel. In such a case, both local heat flux distribution along the cooled walls and upward versus downward energy splitting are of paramount importance for predicting reactor situations in question. Most notably, major relevant experiments were conducted by employing simulant liquids (water, freon), so the data base can only be used to develop prediction models, but not for direct extrapolation to reactor situations [1].

Furthermore, in a previous study, we showed that standard low-Reynolds-number $k-\epsilon$ models fail to predict heat transfer in turbulent natural convection flows under consideration [2]. In particular, these models fail in describing of heat fluxes to the top and, also, to the bottom surface of the liquid pool.

It was indicated that reliable predictions of the local heat fluxes in the large volumetrically-heated core melt pool would require application of the Reynolds stress models, or the second-order modifications of the two-equation models, for description of the turbulence. Most importantly, anisotropic behavior in stably stratified and unstably stratified layers must be modeled. For example, in a two-equation model, the turbulent Prandtl number, Pr_t, and turbulent viscosity, ν_t, have to be re-formulated to take into account specific effects of turbulence generation in buoyancy-induced, strongly stably and unstably stratified flows in the lower and upper regions of the liquid pool, respectively. Although some empirical correlations for Pr_t and ν_t (as functions of the local Richardson number) have been proposed in [2], a better understanding of turbulent transport mechanism is required to develop general correlations for Reynolds stress closure relationship under unstable stratification conditions. It is perhaps instructive to note that there exist very few works, which reported data measurement of turbulent characteristics for these inherently unsteady state flow regimes [3]. Furthermore, only some theoretically derived distributions of Reynolds stresses and turbulent heat fluxes across internally heated fluid layers were available in the literature, e.g. [4].

In this paper, we focus the analysis on turbulent characteristics in an internally heated fluid layer with isothermally cooled top and thermally insulated bottom surfaces. The main idea is to obtain necessary turbulence data from *direct numerical simulation* (DNS) of a naturally convecting flow and to analyse major peculiarities of turbulence behaviour under unstable stratification condition. In the past, DNS was also used for analyzing natural convection heat transfer in fluid layers with internal heat generation with Ra in the range $3{\cdot}10^4 \div 4 \cdot 10^6$ [5]. In present paper, turbulent characteristics in fluid layers with higher Ra numbers are examined, with a particular emphasis on behaviour of Reynolds stresses in this specific flow.

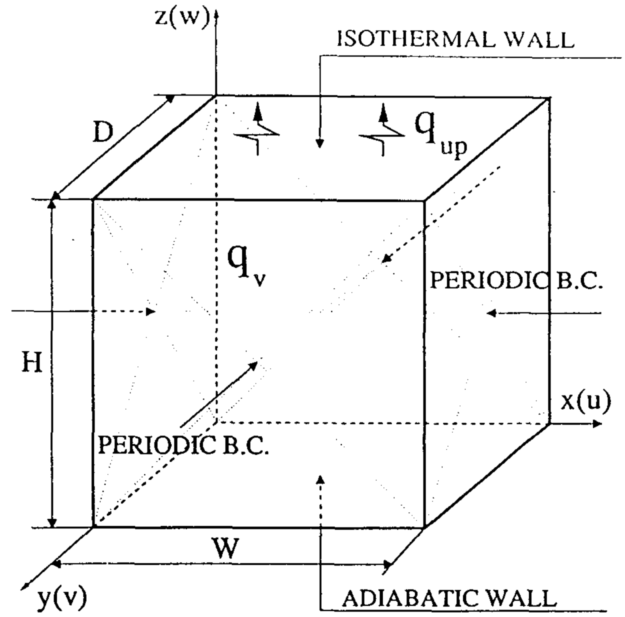

Figure 1: *Coordinate system and computational domain.*

2. SIMULATION AND VALIDATION

2.1 Formulation of the problem

The fluid layer, with height H and internal heat generation rate q_v, is bounded by the upper isothermal surface ($T_{z=H} = T_w$) and bottom adiabatic surface ($z = 0; q_{dn} = 0$); see fig.1. In order to simulate flows and heat transfer within the fluid layer, the governing equations of mass (eq.1), momentum (eq.2) and energy (eq.3) conservation are solved to obtain instantaneous three-dimensional fields of variables of interest:

$$\frac{\partial \rho}{\partial t} + \nabla \cdot (\rho \mathrm{U}) = 0 \tag{1}$$

$$\frac{\partial \rho \mathrm{U}}{\partial t} + \nabla \cdot (\rho \mathrm{U} \otimes \mathrm{U}) = \rho \mathrm{g} + \nabla \cdot (-P\delta + \mu \nabla \mathrm{U}) \tag{2}$$

$$\frac{\partial \rho h}{\partial t} + \nabla \cdot (\rho \mathrm{U} h) - \nabla \cdot (\kappa \nabla T) = \frac{\partial P}{\partial t} + q_v \tag{3}$$

where h is the total enthalpy, P is pressure, and $\mathrm{U} = [u, v, w]$ is the velocity vector. It can be shown for the considered problem that the only dimensionless groups are Rayleigh (Ra) and Prandtl (Pr) numbers.

In addition, periodic boundaries are imposed in two horizontal directions (x, y), and it is assumed that both hydro- and thermo-fields have the same periodic length in the same direction. No-slip boundary conditions are applied to all velocity components at the upper and bottom surfaces. The quiescent state ($\mathrm{U} = 0$ and $T = T_w$) is used as the initial conditions for the time integration.

2.2 Numerical treatment

The numerical calculations were performed using AEA-CFDS FLOW-3D code release 3.3. [6]. The basis of the code is a conservative finite-difference method with all variables defined at the centre of control volumes which fill the physical domain being considered. To avoid the chequerboard oscillations in pressure and velocity the improved Rhie-Chow interpolation method is used. Third-order accurate CCCT upwinded scheme for advection term treatment, fully implicit backward difference time stepping procedure and SIMPLEC velocity-pressure coupling algorithm have been utilized.

During calculations the overall energy balance in the fluid layer is checked. For relatively low Ra numbers ($Ra < 10^6$) computations led to steady state solutions, while for higher Ra numbers the result upward heat flux q_{up}, and, consequently, the overall energy balance and temperature difference within the layer, exhibit an oscillatory behavior (up to 20% for $Ra = 5{\cdot}10^{12}$). The computations were continued and *measurements* of turbulent correlations were started after the quasi-steady state energy balance and unchanged horizontally averaged temperature profile had been achieved. Local second-order one-point momentums were then calculated as $\overline{\phi_1' \phi_2'} = \overline{\phi_1 \phi_2} - \overline{\phi_1} \cdot \overline{\phi_2}$ (here overline means averaging over *measurement time*). The local upper wall heat flux was evaluated by using a Taylor's series expansion of the temperature at three upper nodes of the computational domain.

All *three-dimensional* calculations were performed with using the grid of $35 \times 35 \times 74$ (or 90650 grid points). The mesh was uniform in the horizontal directions (x, y). In order to obtain the sufficiently accurate prediction of the flow and heat transfer characteristics, a very dense grid is needed in the vertical direction z near the layer's upper and bottom surfaces. Hence, a factor of geometrical progression $(1.01 \div 1.18)$ was utilized when generating the z-grid.

2.3 Validation

Calculated Nusselt numbers are compared to empirical correlation by Kulacki et al. $Nu = 0.389 \cdot Ra^{0.228} \pm 15\%$ (refs.[3],[8]), which is valid for the Rayleigh number range $2 \cdot 10^3 \leq Ra \leq 2.2 \cdot 10^{12}$. One can see, on fig.2, a good agreement between calculated and experimental values of Nusselt numbers for Rayleigh numbers up to $5 \cdot 10^{12}$. The post-calculation analysis showed, however, that the currently used $[x, y]$-plane nodalization may not be enough to simulate the finest scale movement for Rayleigh numbers higher than 10^9. In the present paper, therefore, detailed turbulence data are examined and discussed for $Ra \leq 10^9$.

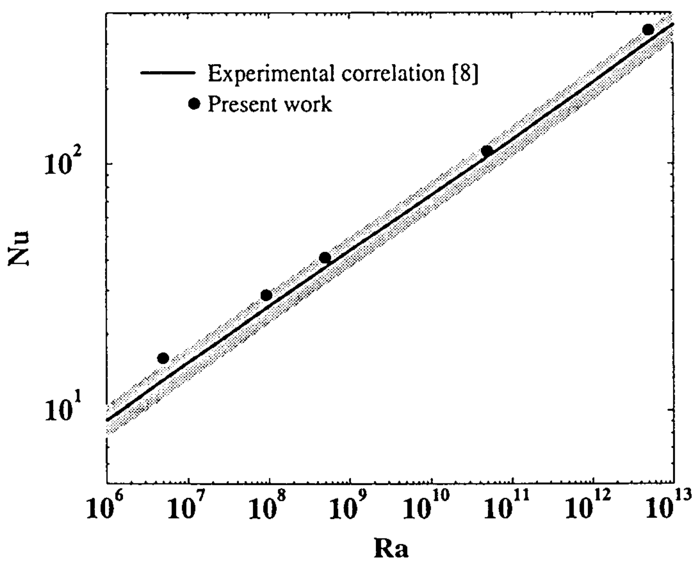

Figure 2: *Prediction of Nusselt number.*

Fig.3 depicts the calculated dimensionless temperature profile across the fluid layer for $Ra = 9.3 \cdot 10^7$. The deviations between the present work result and measurement data [3], empirical correlation [8] as well as analytical model by Cheung [4] are not overriding uncertainty of measurement employed.

As mentioned, heat transfer to the cooled upper surface is governed by unstable stratification convective flows, with cooled blobs falling down to the mixing region of the internally heated fluid layer. In such a case, convective heat transfer can be characterized by a time scale of $t_{blob} \sim \frac{H}{U_{blob,max}}$, which is much smaller than a conduction time scale $t_{cond} \sim \frac{H^2}{\alpha}$. In order to describe, properly, transport phenomena in the upper layer region, calculational time step must be much smaller than t_{blob}, so all blobs are resolved in time. In other words, $\Delta Fo = \frac{\Delta t \cdot \alpha}{H^2} \ll Fo_{blob} = \frac{t_{blob}}{t_{cond}}$. This condition is actually satisfied for all computed cases; see fig.4. Similarly, blob resolution in space requires horizontal mesh size being less than blob size d_{blob} and vertical mess size being less than thermal boundary layer thickness δ_T, i.e. $\Delta x = \Delta y \ll d_{blob}$ and $\Delta z \ll \delta_T$.

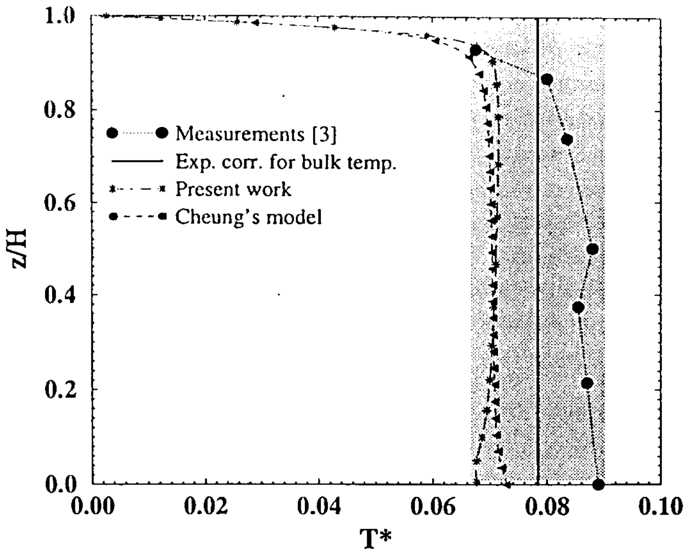

Figure 3: *Prediction of temperature profile.*

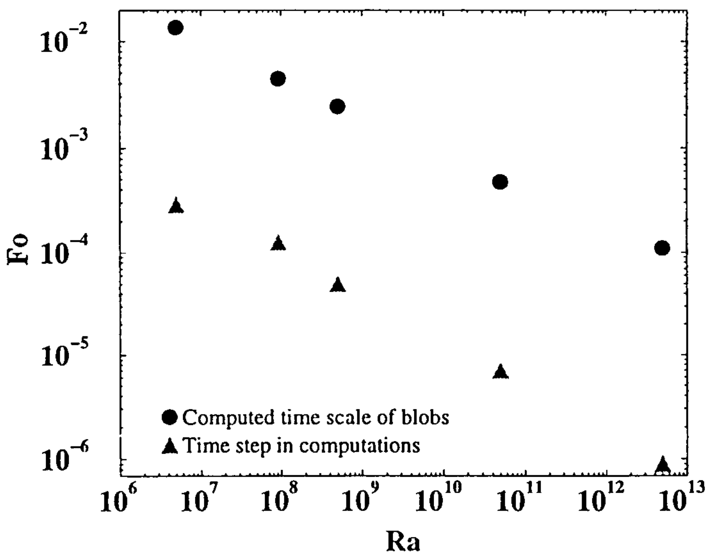

Figure 4: *Time scales and time step.*

The validity of simulation results can also be shown by looking at fig.5, which presents measured and calculated temperature fluctuations. Even though the data were maximum fluctuations [3] and calculated data were root-mean-square temperature fluctuations, they have quite the same behaviour. In both cases, the maximum oscillations were observed nearby to the upper cooled surface. Thus, it is believed that the important turbulence structures can be captured with reasonable resolution.

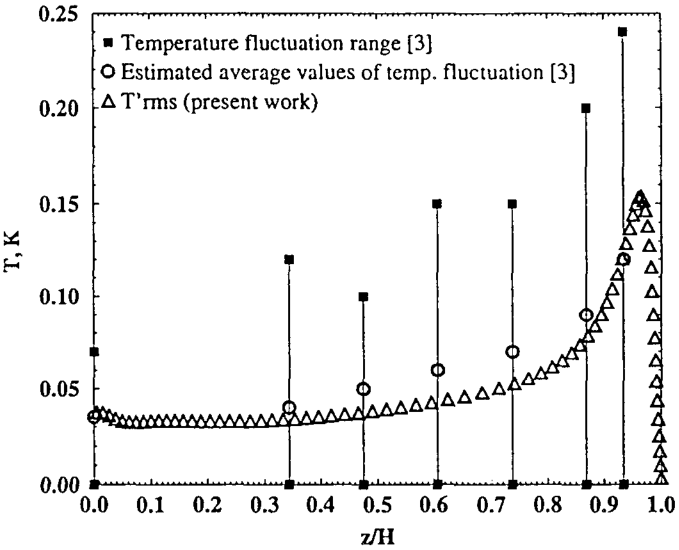

Figure 5: *Temperature fluctuations.*

3. RESULTS AND DISCUSSION

Figs.6-8 show calculated instant temperature fields on a horizontal plane near the upper surface (fig.6), and two vertical planes (fig.7-8). In general, the structure of flow convection consist of cold tongues (thermals) which are generated on the isothermally cooled upper surface and falling down. For relatively low Ra numbers ($Ra \sim 10^6$) the sizes of thermals are the same order of magnitude as the fluid layer height. With increasing of the Rayleigh number the blob size range is wider, and the sketch of thermals on the upper wall becomes more complicated and three-dimensional. Only few of generated on the upper wall fluid blobs are able to maintain their thermal identity and reach the adibatic bottom wall. For very high Ra numbers ($Ra \sim 10^{12}$) the blobs existence is suppressed in the upper wall region. While the largest thermals possess huge energy and determine heat transfer process, important portion of heat is removed by the smallest blobs. So very fine nodalization is required not only in the vertical direction (large temperature gradient) but also in horizontal directions to resolute the small size blobs.

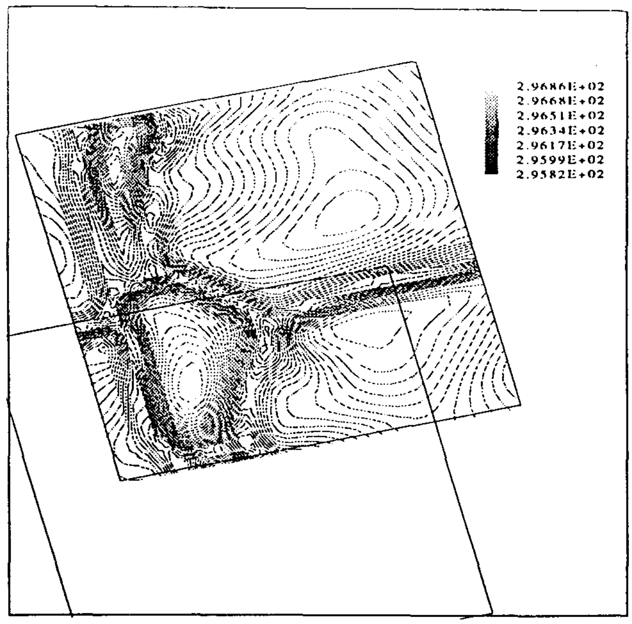

Figure 6: *Instant temperature field* ($[x, y]$*-plane*, $z/H = 0.984$, $Ra = 9.3 \cdot 10^7$).

3.1 Turbulence statistics of the hydro-field

Fig.9 shows the calculated vertical distribution of Reynolds stresses across the fluid layer with $Ra = 9.3 \cdot 10^7$. All the values are dimensionless with respect to $\left(\frac{\nu}{H}\right)^2$ (where $\frac{\nu}{H}$ is a characteristic velocity). It can be seen that the turbulent shear stresses ($\overline{u_i'u_j'}$, $i \neq j$) are negligibly small in comparison to the normal Reynolds stresses ($\overline{v'v'}, \overline{u'u'}, \overline{w'w'}$). In the turbulent core region, the vertical stress, $\overline{w'w'}$, prevails the horizontal stresses ($\overline{u'u'}, \overline{v'v'}$) and, hence, $k \simeq \frac{\overline{w'^2}}{2}$. The turbulent kinetic energy is, however, dominated by the horizontal normal stresses in the nearwall regions, i.e. $k \sim \frac{\overline{u'^2}+\overline{v'^2}}{2}$.

Fig.10 presents the budget of turbulent kinetic energy in dimensionless form, with respect to viscous dissipation scale $\frac{\nu^3}{H^4}$. One can see that the shear-induced turbulence generation is much smaller than buoyancy-induced turbulence generation, i.e. $P_k = -\overline{u_i'u_j'}\frac{\partial U_i}{\partial x_j} \ll B_k = -\beta g \overline{u_i'T'}$. The local turbulence equilibrium ($P_k + B_k \simeq \varepsilon$) takes place only in a convection-dominated region of $0.1 < \frac{z}{H} < 0.4$, while transport of turbulent kinetic energy k plays an important role in the rest region.

3.2 Turbulence statistics of the thermo-field

Fig.11 shows the vertical distribution of turbulent heat fluxes across the fluid layer with $Ra = 9.3 \cdot$

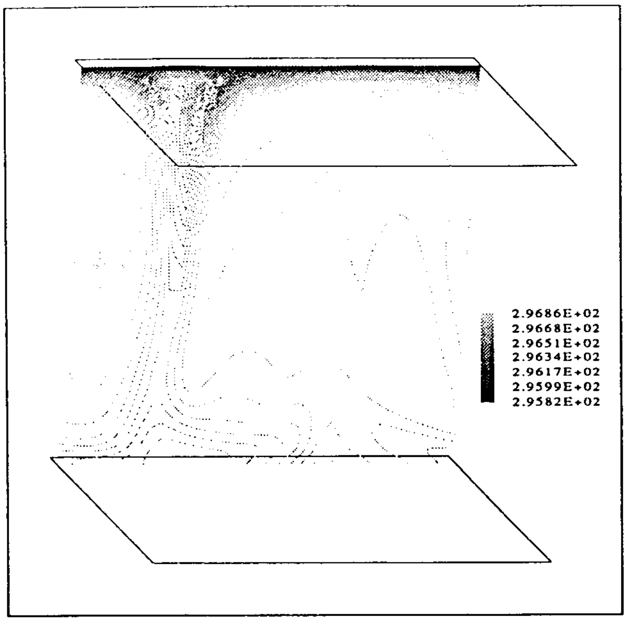

Figure 7: *Instant temperature field ([x, z]-plane, $y/D = 0.0656$ $Ra = 9.3 \cdot 10^7$).*

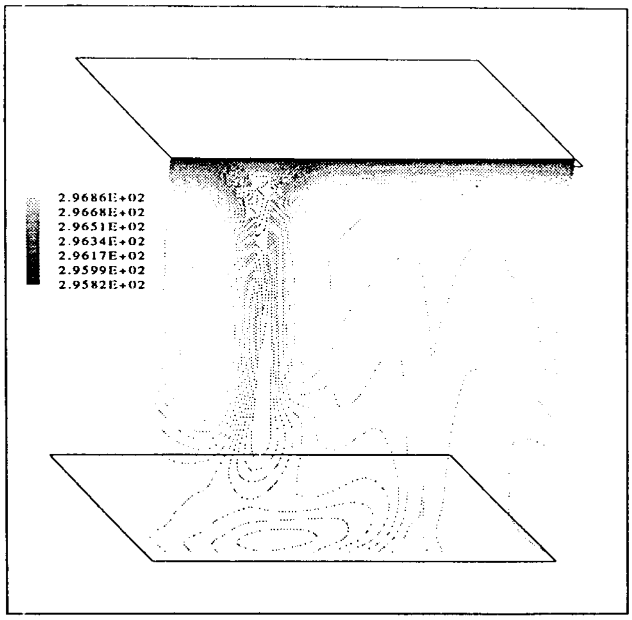

Figure 8: *Instant temperature field ([x, z]-plane, $y/D = 0.787$ $Ra = 9.3 \cdot 10^7$).*

10^7. All the variables are in dimensionless form, with respect to $\frac{\alpha(T_{ave}-T_w)}{H}$. The vertical component $\overline{w'T'}$ is the dominant one in the turbulent heat flux, $\Sigma\overline{u_i'T'} = \overline{v'T'} + \overline{u'T'} + \overline{w'T'}$ in the entire fluid layer. The DNS-measured vertical turbulent heat flux, $\overline{w'T'}$, is in a good agreement with the analytical model by Cheung [4].

Based on an eddy diffusion formulation, one could define turbulent thermal diffusivity of the turbulent flows in question as $\alpha_{T,i} = \frac{\overline{u_i'T'}}{\partial \overline{T}/\partial x_i}$. However, the time-average temperature field of the turbulent core region of the fluid layer is well-mixed, with temperature gradients tending to zero (see fig.3). Besides their infinitely large values, the turbulent diffusivities $\alpha_{T,i}$ are strongly anisotropic in the space directions. These results confirmed the conclusion of the previous study [2], which is based on $k-\varepsilon$ modeling and analysis of specific experiments in internally heated liquid pools.

Fig.12 presents the budget of the fluctuating temperature variance. One can see that temperature fluctuations are generated in the very top region of the fluid layer, $0.85 < \frac{z}{H} < 0.999$. This is in accordance with the behaviour of temperature fluctuations given by fig.5. In addition, the comparison with Cheung's model is given for $Ra = 9.3 \cdot 10^7$.

The present DNS result indicates that non-equilibrium of thermal variance must be modeled in the unstably stratified region, where transport (convection, diffusion, transient) of temperature fluctuations becomes a dominating process.

3.3 Parameters of turbulence modeling

From the above analysis, it becames clear that neither turbulence equilibrium assumption nor isotropic eddy diffusion concept can be utilized to describe turbulence phenomena in question. In order to model the temperature variance in second-order one-point momentum closure approach, the thermal-to-mechanical time scale ($R = \frac{\tau_T}{\tau_u} = \frac{\overline{T'^2}/2\varepsilon_T}{k/\varepsilon}$) must be modeled (for more discussion, see [2]). It was noticed that under unstable stratification condition R may differ, significantly, from the values ($0.4 \div 0.8$), accepted for equilibrium conditions. However, one can see from fig.13 that R is close to 2 in the turbulent core region, and increases near the walls due to their suppression effects.

In order to investigate qualitative behaviour of turbulence in unstably stratified layers, we made an attempt to define the eddy transport properties. By using $\nu_t = C_\mu k^{1/2} L_\varepsilon = C_\mu k^2/\varepsilon$, we obtain the isotropic eddy viscosity, which is rather small [$\frac{\nu_t}{\nu} \simeq (1 \div 2)$ for $Ra = 9.3 \cdot 10^7$, see fig.14]. The isotropic eddy diffusivity for heat is defined by using mixed time scale as follows $\alpha_t = C_\lambda k\sqrt{(k/\varepsilon) \cdot (\overline{T'^2}/\varepsilon_T)}$, with $C_\lambda = 0.11$. Turbulent Prandtl number, $Pr_t = \frac{\nu_t}{\alpha_t}$, is about 0.7 in the turbulent core region for $Ra = 5 \cdot 10^6$,

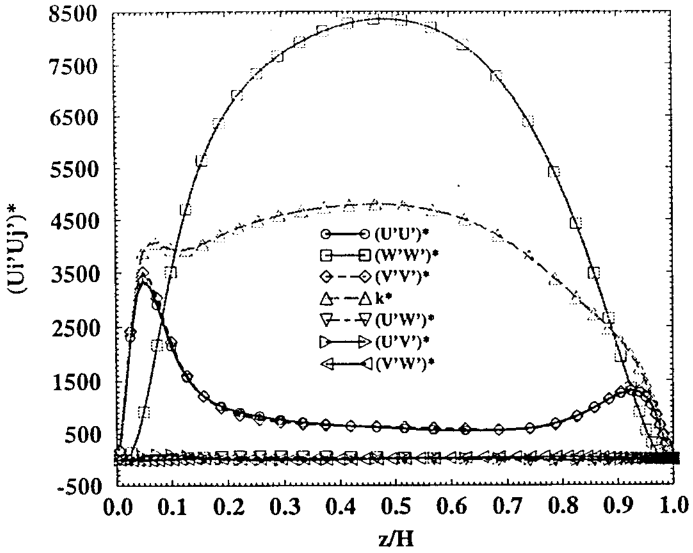

Figure 9: *Distribution of Reynolds stresses.*

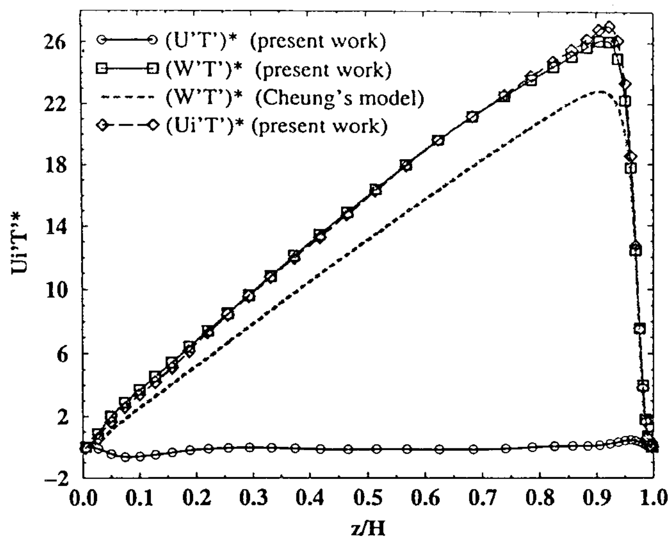

Figure 11: *Distribution of turbulent heat fluxes.*

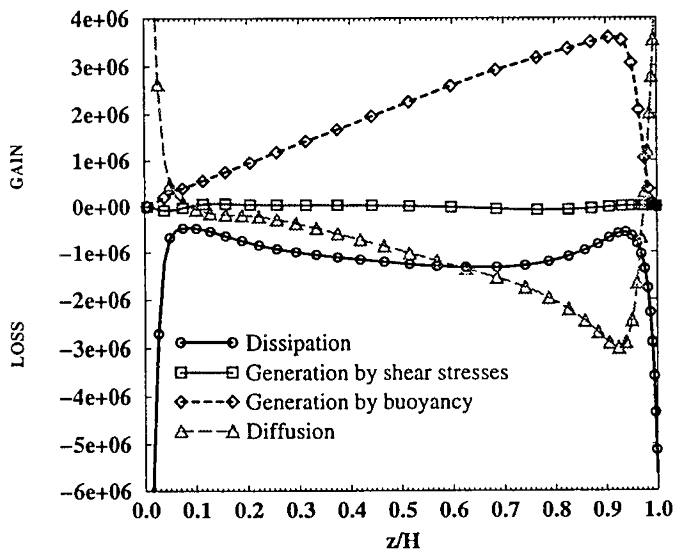

Figure 10: *Budget of turbulent energy.*

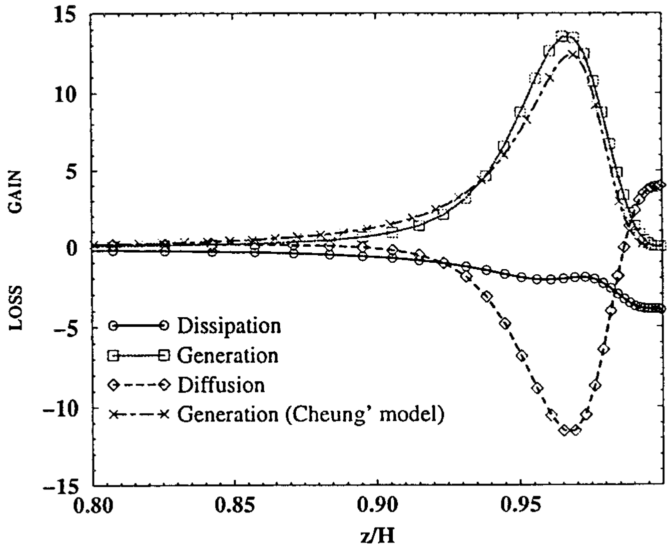

Figure 12: *Budget of mean temperature variance.*

and decreases with the increasing of Rayleigh number (about 0.5 for $Ra = 9.3 \cdot 10^7$, see fig.15). As a consequence of R behaviour, the turbulent Prandtl number decreases, drastically, in the nearwall region to $Pr_t \ll 1$.

It must be noted here that all the comparison and computations were made for the electrolytically heated water layers, which have Prandtl numbers in the range 3÷7. However, reactor core melts have relatively high heat conductivity and, consequently, lower Prandtl numbers (in the range 0.4÷1.2). This question has yet to be addressed.

Finally, it is perhaps instructive to note that the numerical method and simulation approach utilized in the present work are sufficiently robust and general. The technique can, therefore, be used for studies of turbulent natural convection flows with complex geometries [9].

4. CONCLUSION

Direct numerical simulation of a naturally convecting flow in an internally heated fluid layer, with a constant temperature boundary condition on the upper surface and thermal insulation boundary condition on the bottom surface, is performed for several Rayleigh numbers in the range $5 \cdot 10^6$ - $1 \cdot 10^8$ using finite-difference schemes. The approach enables the determination of the top wall heat fluxes, the mean temperature fields, the distributions of Reynolds stresses and turbulent heat fluxes.

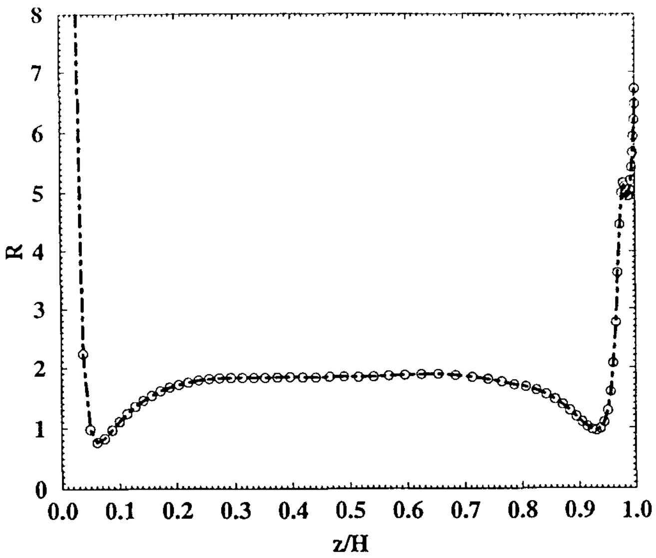

Figure 13: *Dissipation time scale ratio.*

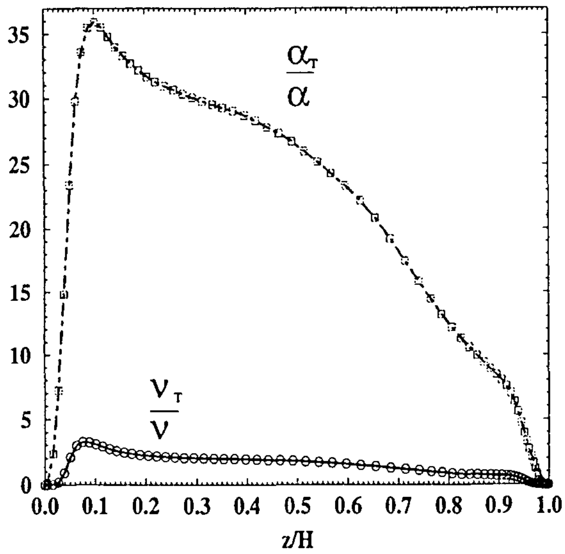

Figure 14: *Turbulent transport properties.*

1. The calculated Nusselt number, temperature distribution within the fluid layer and temperature fluctuations are in good agreement with experimental data of Kulacki et al. [3], [8]. Also, the calculated turbulent heat fluxes agree well with those predicted by the analytical model of Cheung [4].

2. Analysis of the calculated turbulent characteristics shows significant anisotropy of turbulent transport properties. In particular, the turbulent Prandtl number is smaller than unity and decreases with increasing of Rayleigh number. So, the isotropic eddy diffusion approach can not be used to describe turbulent natural convection heat transfer under unstable stratification condition in question. Furthermore, dissipation time scale ratio R is shown to differ, significantly, from values, accepted for thermal variance equilibrium conditions. Preliminarily, values of

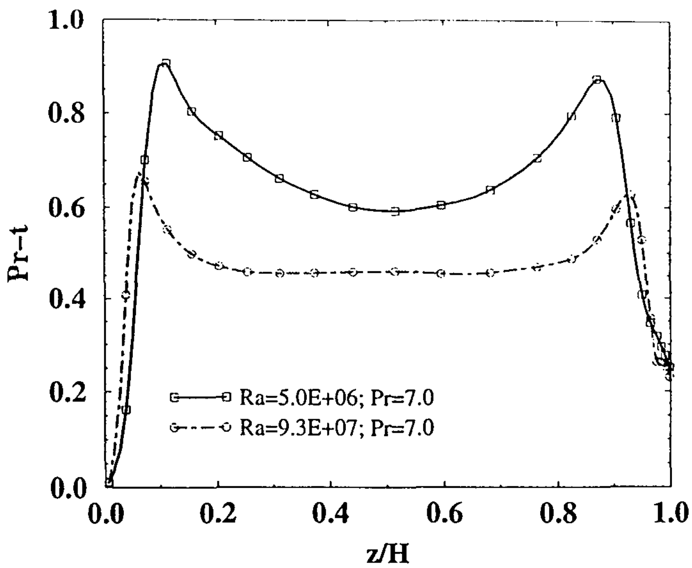

Figure 15: *Turbulent Prandtl number for* $Ra = 5 \cdot 10^6$; $9.3 \cdot 10^7$.

$R > 1$ were obtained for cases with fluid Prandtl number $Pr = 7$.

3. The turbulence data obtained are important for developing Reynolds stress correlations and reliable methods for describing turbulent natural convection heat transfer to the isothermally cooled upper surface in an internally heated liquid pool.

It is necessary to perform, in a near future, similar computations for internally heated liquid layers with fluid Prandtl number ranging between $0.4 \div 1.2$, to explore possible effect of Pr number on the behaviour of turbulent characteristics and to ensure the applicability of calculated data and models to reactor situations of interest.

Acknowledgments- The authors wish to appreciate the support of Professor B.R. Sehgal (RIT) during the course of this work.

Nomenclature

<u>*Arabic*</u>

g	Gravitational acceleration, m/s^2
Nu	Nusselt number, $Nu = q_{up}H/[\kappa(T_w - T_{ave})]$
Pr	Prandtl number, $Pr = \nu/\alpha$
Ra	Rayleigh number, $Ra = q_v H^5 g\beta/(\alpha\kappa\nu)$
t	time, s
T^*	Dimensionless temperature, $T^* = \frac{2}{Nu}$

T_{ave} Bottom-surface averaged temperature

$T_{ave} = \frac{\int_{t_{av}} \int_{A_{dn}} T_{dn} dt \cdot dA}{t_{av} \cdot A_{dn}}$, K

Greek

α Thermal diffusivity, m^2/s

β Coefficient of thermal expansion, 1/K

δ Kroenecker's delta

κ Heat conductivity, W/m·K

μ Dynamic viscosity, Pa·s

ν Kinematic viscosity, m^2/s

ρ Density, kg/m^3

References

[1] Dinh, T.N., Nourgaliev, R.R., and Sehgal, B.R., On Heat Transfer Characteristics of Real and Simulant Melt Pool Experiments, *Proceeding of the Seventh International Topical Meeting on Nuclear Reactor Thermal Hydraulics NURETH-7*, Saratoga Springs, NY, September 10-15, 1995, NUREG/CP-0142, Vol.2, pp.827-845.

[2] Dinh, T.N. and Nourgaliev, R.R., On Turbulence Modeling in Large Volumetrically Heated Liquid Pools, J. *Nuclear Engineering and Design*, 1996 (accepted, in press).

[3] Kulacki, F.A. and Nagle, M.Z., Natural Convection in a Horizontal Fluid Layer with Volumetric Energy Sources, *Transactions of the ASME, J. Heat Transfer*, 1975, Vol.97, pp.204-211.

[4] Cheung, F.B., Natural Convection in a Volumetrically Heated Fluid Layer at High Rayleigh Numbers, *Int.J. Heat Mass Transfer*, Vol.20, pp.499-506, 1977.

[5] G. Grötzbach, Direct Numerical and Large Eddy Simulation of Turbulent Channel Flows. In: *Encyclopedia of Fluid Mechanics.* Vol.6, pp.1337-1391, Ed.: N.P. Cheremisinoff, Gulf Publ. Houston (1987)

[6] CFDS-FLOW3D, 1994, Release 3.3, *User Manual*, June 1994.

[7] Emara, A.A. and Kulacki, F.A., A Numerical Investigation of Thermal Convection in a Heat-Generating Fluid Layer, *Transactions of the ASME, J. of Heat Transfer*, Vol.102, August 1980, pp.531-537.

[8] Kulacki, F.A. and Emara, A.A., Steady and Transient Thermal Convection in a Fluid Layer with Uniform Volumetric Energy Sources, *Journal of Fluid Mechanics*, Vol.83, part 2, pp.375-395, 1977.

[9] Nourgaliev, R.R., Dinh, T.N., and Sehgal, B.R., Natural Convection in Volumetrically Heated and Sidewall Heated Melt Pools: Three-Dimensional Effects, *Proceedings of the IMACS-COST Conference on Computational Fluid Dynamics "3D Complex Flows"*, Lausanne, Switzerland, 1995.

Paper No. 2

MODELING OF HEAT TRANSFER IN HEAT-GENERATING LIQUID POOLS BY AN EFFECTIVE DIFFUSIVITY-CONVECTIVITY APPROACH

V.A. Bui and T.N. Dinh
Royal Institute of Technology, Division of Nuclear Power Safety
Brinellvägen 60, 10044 STOCKHOLM, SWEDEN
Fax + (46)(8) 790-7678, e-mail: anh@ne.kth.se

ABSTRACT - The paper presents an effective diffusivity-convectivity approach to the modeling of heat transfer in heat-generating fluid layers and pools, in which the buoyancy-induced convective heat transport is addressed by means of pseudo-convective terms and effective heat conductivity. The approach was applied to analyze the heat transfer in fluid layers, square as well as semicircular and hemisphere cavities with different boundary conditions. The computational results showed that some essential parameters, like the fraction of heat removal to cooled surfaces, the temperature fields within the layers and pools, and the local distribution of heat fluxes on pool boundaries, can be reasonably described by this approach.

1. INTRODUCTION

Liquid pools with internal heat generation are of primary interest in many industrial cases, especially, in nuclear engineering. Under the hypothetical severe accidents in a nuclear reactor a molten fuel pool may be formed on the lower head of reactor vessel as the result of core melt down or on the floor of containment, when the reactor vessel fails. In such cases the knowledge of the transient thermal behavior of the decay-heated corium pool is essential for the assessment of different safety characteristics of the system, like the coolability of the melt pool or the debris bed, the capability of melt retaining inside the reactor vessel, and the timing of the vessel lower head failure.

Heat transfer inside a liquid pool with volumetric heat source is driven by natural convection, that can be changed from laminar mode to turbulent according to the Rayleigh (Ra) number. The natural convection inside such a melt pool has a large stratified region on most of lower pool portion and an intensively mixed region of unstable stratification on top. The heat transfer to the side wall is, however, governed by the development of the boundary layer of the flow moving downward along the cooled wall.

Due to the complex nature of the natural convection heat transfer inside such internally-heated pools and the involvement of other physical phenomena and mechanisms, like phase change, property changes in a wide temperature range, intense interactions with surrounding environment or structures, the application of traditional approaches, based on the solution of the Navier-Stocks equations and turbulence modeling, can be highly difficult and inefficient. At the same time, the integral methods, based on some lumped-parameter models of involved physical phenomena, while simple, can not provide detailed information about the distribution of local parameters and characteristics. Recently, an effective diffusivity approach was used in the modeling of natural convection heat transfer in heat-generating pools, in which only heat conduction equation is solved and the effect of natural convection is taken into account by using the effective directional thermal conductivities. This approach was successfully used to describe the natural convection heat transfer in some fluid layers and pools with simple boundary conditions (one cooled surface). However, its validation for more complex cases of boundary condition is not yet available.

The aim of the present work is to develop a new method for modeling heat transfer in a heat-generating liquid pool, which can reasonably describe the related physical processes and phenomena, and, at the same time, is simple enough, so that it can be implemented in an integrated reactor safety code.

2. THE MODELING APPROACH

In general, the major features of the developed modeling method can be stated as follows. The heat transfer inside a convecting liquid (melt) pool with volumetric energy source is assumed to be driven by two mechanisms: (a) the *vertical upward* movement of heat-generating stratified fluid layers; and (b) the *horizontal* heat transfer to the cooled side wall through the liquid layer developing downward along the cooled wall. In the present work, the first mechanism is modeled using a new method (named as *effective convectivity* approach), in which the convective term in heat transfer is defined analytically. The second mechanism is modeled by means of *the effective diffusivity* approach (Cheung et al. [1] [2]).

The mathematical formulation of the problem is based on the *two-dimensional*, energy conservation equation, written for a general curvilinear coordinate system:

$$\frac{\partial \rho C \theta}{\partial t} + \nabla \cdot (\rho C \mathbf{U} \theta) = \nabla \cdot (k \nabla \theta) + Q_v \qquad (1)$$

In order to solve equation 1, the velocity $\mathbf{U} = [u, v]$ is analytically determined from the pool characteristics and the boundary conditions. In this work, the horizontal velocity component v is neglected and the buoyancy-induced vertical velocity u is defined from the analytical and experimental correlations of heat transfer coefficients on the boundaries.

The diffusion term of equation 1 can be rewritten for the case of homogeneous orthotropic, anisotropic heat conduction as follows [4]

$$\nabla \cdot (k \nabla \theta) = \frac{\partial}{\partial x}(q_x) + \frac{\partial}{\partial y}(q_y) \qquad (2)$$

with $q_x = -k_x \cdot grad\theta$, $q_y = -k_y \cdot grad\theta$, k_x, and k_y are the heat fluxes and heat conductivities in the direction x (horizontal) and y (vertical), respectively. Moreover, in present work, we assume that $k_y = k$, since the heat transfer in the vertical direction is dominated by the convective transport, u. The effective conductivity, k_x, is defined from the heat transfer rate in the horizontal direction in case of pools cooled from side walls.

The actual expressions for the effective velocity u and effective conductivity k_x will be formulated for each specific case of pool geometry and boundary conditions in the following sections.

3. FLUID LAYERS WITH SIMPLE BOUNDARY CONDITIONS

3.1 Fluid layer cooled from top

The natural convection in a heat generating fluid layer cooled from its top (figure 1) is characterized by an unstably stratified flow pattern, in which the average flow moves mainly upward and carries most of the heat generated within the volume to the isothermally cooled boundary. Simultaneously, cooled liquid tongues fall down in a chaotic manner, carrying liquid mass back to the lower region of the fluid layer. The time-averaged temperature distribution within the fluid layer is quite uniform, except for the very top part nearby the cooled surface. In such a case

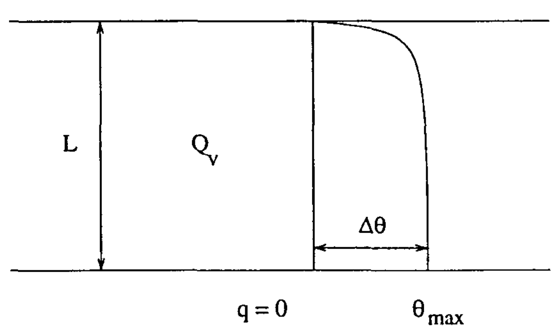

Figure 1: A fluid layer cooled from top.

the heat may be assumed to be removed from the fluid layer only by the average flow with upward velocity u, that can be defined from the heat balance equation $\rho C u \triangle \theta = Q_v L$. Expressing the relation between heat flux $Q_v L$ and temperature difference $\triangle\theta$ through Nusselt number, we obtain the following correlation for u

$$u = \frac{Q_v L}{\rho C \triangle \theta} = \frac{\alpha}{L} Nu_{up} \qquad (3)$$

where $Nu_{up} = 0.338\, Ra^{0.227}$ [5] [6].

Kulacki et al. [5],[6] reported measurements of transient temperature distribution across volumetrically heated horizontal fluid layers, which were cooled from top and thermally insulated from bottom. Measurements were performed for wide ranges of Rayleigh number and layer depth (L). The computational results of the steady-state and transient temperature profiles are presented in figures 2-4 and are in reasonably good agreement with the experimental data (*filled points*).

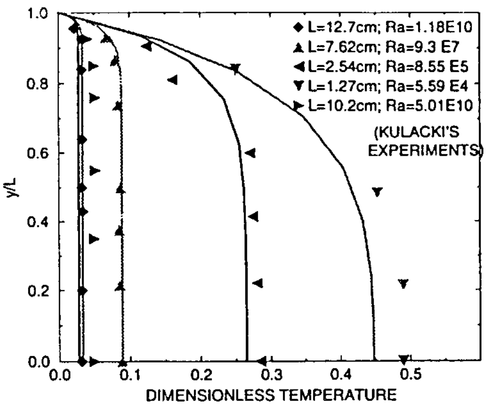

Figure 2: Steady-state temperature distribution.

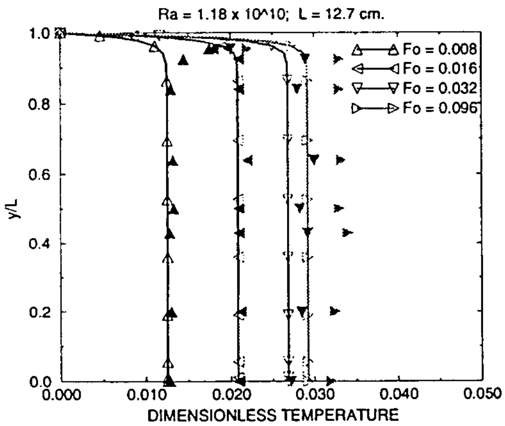

Figure 3: Transient temperature profiles ($Ra = 1.18 \times 10^{10}$).

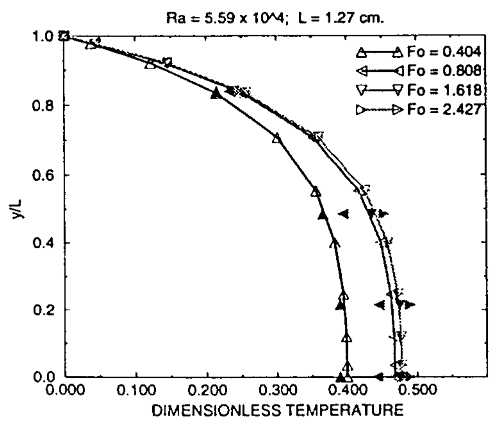

Figure 4: Transient temperature profiles ($Ra = 5.59 \times 10^{4}$).

3.2 Side-cooled liquid cavity

In case of cavities cooled from side the heat transfer to the side walls depends on the characteristics of the boundary layer developing along the vertical wall, that might change from laminar to turbulent flow regime if the local Rayleigh number exceeds a critical value and periodical disturbances occur in the form of thermal waves (figure 5). Because such a boundary layer development occurs only in a very narrow region next to the cooled boundaries and the heat transfer in the horizontal direction is dominant, the proposed approach based on the average (effective) velocities may not be applicable. In this case the effective diffusivity approach proposed by Cheung et al. [1] [2] may be used. The heat conductivity

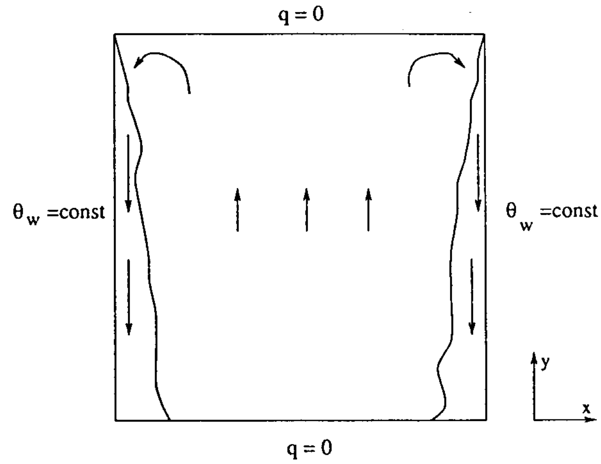

Figure 5: Square cavity cooled from side walls.

on the horizontal direction, k_x, is defined from the following correlation

$$- k_x \left.\frac{\partial \theta}{\partial x}\right|_w = h(\bar{\theta} - \theta_w) = h \triangle \theta_w \qquad (4)$$

where $\bar{\theta}$ is the horizontally averaged temperature for a vertical position. Therefore,

$$k_x = \frac{Nu_y k}{y} \left(\frac{\bar{\theta} - \theta_w}{- \left.\frac{\partial \theta}{\partial x}\right|_w} \right) \qquad (5)$$

where $Nu_y = \frac{h \cdot y}{k}$ is the local Nusselt number. In cases of laminar natural convection heat transfer from an inclined surface, the Eckert-type correlation proposed by Chawla et al.[7] can be applied to define Nu_y

$$Nu_y = 0.508\, Pr^{1/4} \left(\frac{20}{21} + Pr \right)^{-1/4} Ra_y^{1/4} \qquad (6)$$

where Ra_y is the local Rayleigh number based on characteristic length y', that is the boundary-layer development length from the leading edge of the cooled surface:

$$Ra_y = Gr_y Pr = \frac{\beta \triangle \theta_w g y'^3}{\nu^2} \frac{\nu}{\alpha} \quad (7)$$

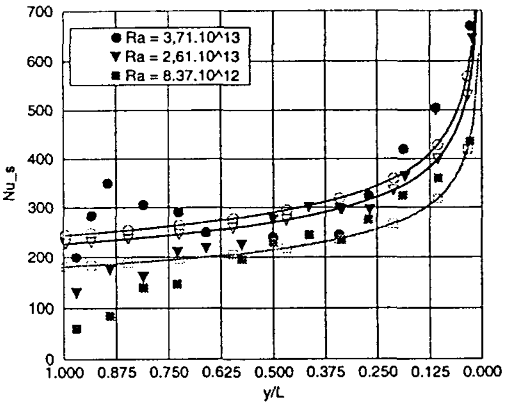

Figure 6: Local distribution of Nu_S at the cooled vertical side wall.

Calculations are performed for the cavity cooled from its sides with the same conditions listed in the experiments performed by Steinberner and Reineke [8]. The size of the cavity is 0.8m x 0.8m. The computational results are presented in figure 6 together with experimental data of Steinberner and Reineke. It is worth to note that the computational local distributions of $Nu_S(y)$ exactly mirrors the dependency 6. Since Nu_y presents the heat transfer across one-dimensional free boundary layer development along infinite heat-exchange surface, no effect of interaction between this boundary layer and the cavity's bottom surface as well as with stagnant liquid layer at the lower part of cavity can be modeled. Therefore, the proposed scheme can not adequately describe the heat flux distribution on the lower part of the side wall and the transition to turbulence (e.g., $Ra = 3.71 \times 10^{13}$ [8]).

4. FLUID LAYERS WITH COMPLEX BOUNDARY CONDITIONS

4.1 Fluid layer cooled from top and bottom

In this case the fluid layer can be divided into two sublayers with distinctive effective velocity for each layer. The upper sublayer is unstably stratified and the generated heat is removed by the effective velocity u_{up} to the upper cooled surface. The lower sublayer is stably stratified with heat removed upwards by the effective velocity u_{low} and downwards by heat conduction. The heat balance in both parts of the layer can be represented as follows

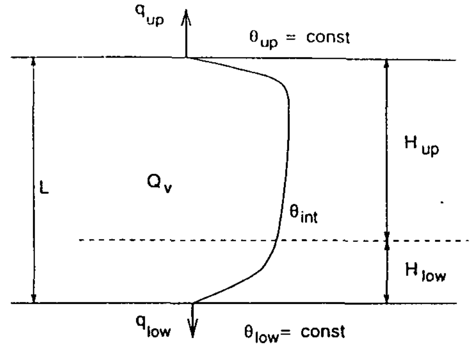

Figure 7: A fluid layer cooled from top and bottom.

$$Q_v H_{low} = \rho C_p u_{low}(\theta_{int} - \theta_{low}) + q_{low};$$
$$Q_v H_{up} = \rho C_p u_{up}(\theta_{int} - \theta_{up}) - \rho C_p u_{low}(\theta_{int} - \theta_{low})$$

Thus, the effective velocities can be calculated from the following correlations

$$\begin{aligned} u_{up} &= \frac{Q_v L}{\rho C_p \triangle \theta_{up}} - \frac{q_{low}}{\rho C_p \triangle \theta_{up}} \\ u_{low} &= \frac{Q_v H_{low}}{\rho C_p \triangle \theta_{low}} - \frac{q_{low}}{\rho C_p \triangle \theta_{low}} \end{aligned} \quad (8)$$

where $\Delta\theta_{up} = (\theta_{int} - \theta_{up})$ and $\Delta\theta_{low} = (\theta_{int} - \theta_{low})$. In case $\theta_{up} = \theta_{low}$, we have $\Delta\theta_{up} = \Delta\theta_{low} = \Delta\theta$.

The interrelations between Q_v, q_{low}, and $\Delta\theta$ can be expressed through $\overline{Nu}$ and Nu_{low} (where $\overline{Nu} = \frac{0.0471\Pi_N^{1/3}}{1-1.734\Pi_N^{-1/9}}$; $\Pi_N = \frac{Ra}{1+0.0414Pr^{-1}}$ [9] and $Nu_{low} = 1.389\, Ra^{0.095}$[8]). The size of the lower sublayer H_{low} can also be evaluated from the Nusselt numbers: $\frac{H_{low}}{L} = \frac{Nu_{low}}{Nu_{up}+Nu_{low}}$. As a result,

$$\begin{aligned} u_{up} &= \frac{\alpha}{L}(\overline{Nu} - Nu_{low}) \\ u_{low} &= \frac{\alpha}{L}\left(\frac{\overline{Nu} Nu_{low}}{Nu_{up} + Nu_{low}} - Nu_{low}\right) \end{aligned} \quad (9)$$

Calculations are performed for layers of different size for wide ranges of Rayleigh number and their results are compared with experimental data obtained by Kulacki and Goldstein [10]. The computational fraction of energy transport to the lower boundary is presented in figure 8 and is in good agreement with experimental data. Figure 9 shows the temperature profiles obtained by calculations (*lines*) in comparison with experimental data (*points*) for different Rayleigh numbers. The discrepancies between these data are within the uncertainty range of measurement and experimental correlations used in the present work. Certainly, the developed method is not able to describe deeper physical relationships (e.g. the dependence of Nusselt number on fluid Prandtl number) other than the physical laws implemented in

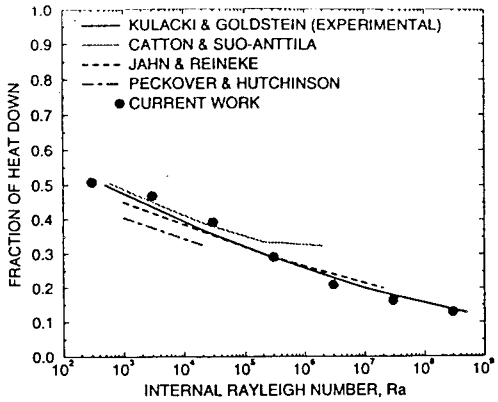

Figure 8: Fraction of heat down.

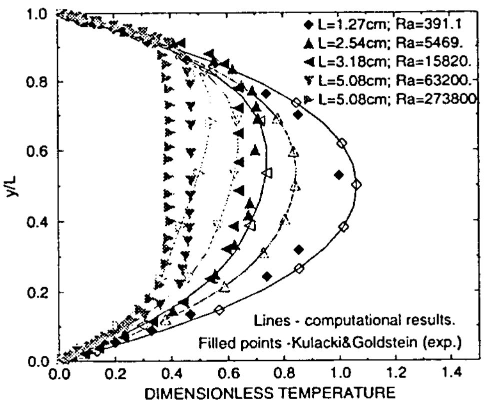

Figure 9: Temperature profiles.

the used correlations. Nevertheless, it is important that the model could correctly predict the fraction of energy removals to the cooled surfaces, which is important for the analysis of the integrity of the reactor vessel, enveloping a debris core melt pool, in cases of severe accidents.

4.2 Square cavities with isothermal boundaries

A combined technique can be applied to model the heat transfer in a cavity with all walls cooled. In this case the heat removal from the top and bottom surfaces are defined by using the technique proposed in the section 4.1 and the heat removal from the side walls are calculated using effective diffusivity approach described in the section 3.2. The experimental data of Steinberner and Reineke [8] are used in order to verify the computational model. The experiments were performed in a flat rectangular cavity of 800mm in size. The test fluid was water and Joulean heating was used as the heat source. The computational results of the local distribution of Nu_S for various Rayleigh numbers in comparison with the experimental data are presented in fig.10. In the case of cavity cooled from all walls there may be some kind of interference of the two above-mentioned heat transfer mechanisms, which reduces the accuracy of both formulations. However, the comparison of computational results with expermental data showed that the model could give quite good proportions of the heat fluxes on top, bottom, and side walls (see figure 11) as well as a reasonable distribution of heat transfer coefficient on the side wall.

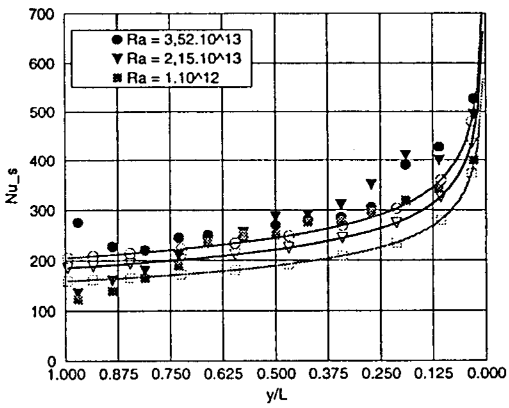

Figure 10: Local distribution of Nu_S number at the vertical wall (all walls cooled).

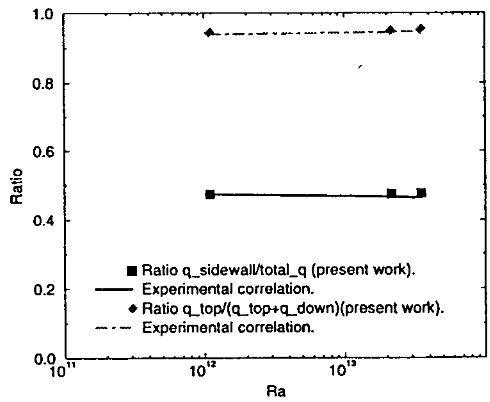

Figure 11: Ratios of heat removed to top, bottom and side walls.

5. COMPLEX GEOMETRY FLUID LAYERS AND POOLS

5.1 Fluid layer with one spherical boundary

The method described in the previous sections can be applied to describe the natural convection heat transfer in more complex geometry, internally heated liquid pools. The following calculations pertain to the experimental study by Min and Kulacki [11] on convective heat transfer in liquid pools with uniformly distributed volumetric energy sources, in which measurements of transient temperature distribution along the centerline of the pool were performed. The pool was bounded from below by a segment of a spherical shell maintained at zero heat flux, from the side by a cylindrical wall also maintained at zero heat flux, and from above by a horizontal surface maintained at constant temperature. In figure 12 the comparison of computational results of transient temperature profiles along the centerline of the pool with experimental data obtained by Min and Kulacki [11] is presented. The model gave a quite good steady-state temperature distribution, while overpredicted the transient from an initial uniform temperature with a step change in Rayleigh number. This is explained by the additional effects of the bottom surface curvature the two-dimensionality of flow pattern.

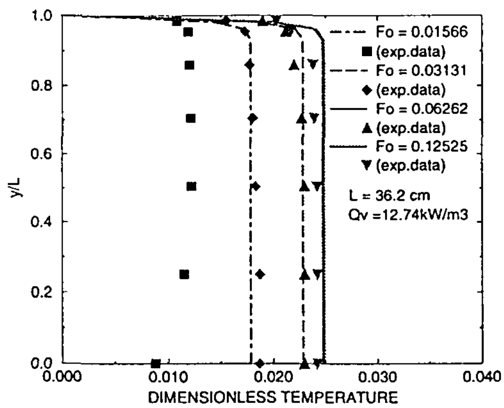

Figure 12: Comparison with experimental data of Min and Kulacki (1978), Run 148

5.2 Semicircular and hemisphere pools

Calculations are also performed for the semicircular and hemisphere pools cooled from all boundaries (figure 13) using the proposed modeling approaches.

Taking into account the surface inclination, we can rewrite equation (4) in a more general form as follows

$$h\,(\bar{\theta} - \theta_w) = \mathrm{q}(z) \qquad (10)$$

where $\mathrm{q}(z)$ is the heat flux, perpendicular to the wall

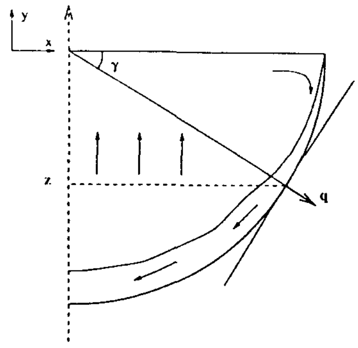

Figure 13: Semicircular and hemisphere pools.

at vertical location z, that can be evaluated as

$$\mathrm{q} = -k_x \left.\frac{\partial\theta}{\partial x}\right|_w cos\gamma(z) + k_y \left.\frac{\partial\theta}{\partial y}\right|_w sin\gamma(z) \qquad (11)$$

where $\gamma(z)$ is the angle of inclination of the wall from vertical direction at vertical location z. Also, the gravitational acceleration g in equations 6-7 should be defined as $\bar{g} = g\,cos\gamma(z)$.

It is worth noting that most of correlations for Nu_y are valid for $\gamma \leq 30^0$, so we assume that only k_x changes along the cooled wall and takes its ordinary value ($k_x = k$) for $\gamma \geq 60^o$. The resulted formulation for k_x has the form

$$k_x = \frac{\left[\frac{Nu_y k}{y'}(\bar{\theta} - \theta_w) - k_y \left.\frac{\partial\theta}{\partial y}\right|_w sin\gamma(z)\right]}{\left[-\left.\frac{\partial\theta}{\partial x}\right|_w cos\gamma(z)\right]}$$

Calculations are performed for a semicircular cavity of 75mm radius with Rayleigh number ranging from 1.4×10^8 to 1.4×10^{13}. The calculated distribution of $Nu_y/\overline{Nu}$ is depicted in figure 14 in comparison with experimental data obtained by Jahn and Reineke [12]. The average Nu_{up} and Nu_{dn} received from calculations (*points*) are shown in figure 15 and agree well with the experimental results (*lines*).

Calculations are also performed for hemisphere pools with 75mm and 150mm radii. The computational average top and bottom Nusselt numbers (*points*) presented in figure 16 are in a good agreement with results of the numerical study of Mayinger et al. (*lines*) (quoted from [13]).

6. SUMMARY

In the paper, heat transfer in internally heated liquid pools is modeled with a particular emphasis on the validation of the developed method in various geometries and under different boundary condi-

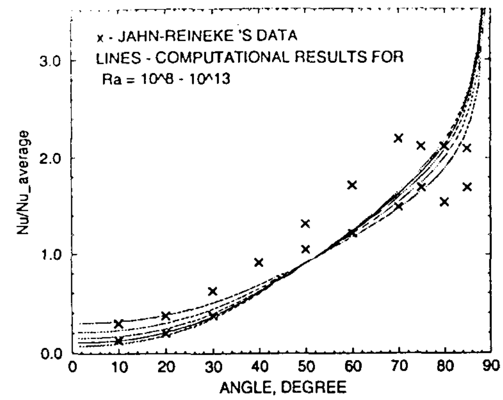

Figure 14: Local distribution of Nusselt number on the curved surface.

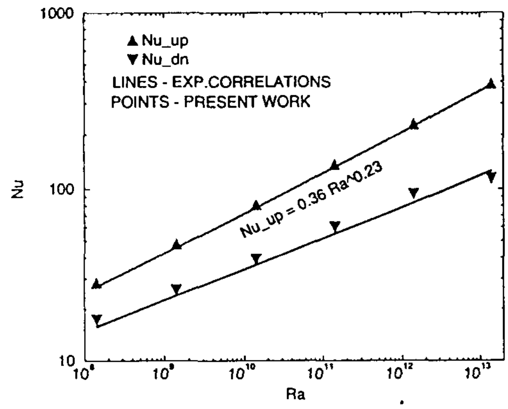

Figure 15: Average Nusselt numbers (semicircular pools).

tions. It has been shown, by comparing the computational results with the available experimental data, that the method is capable of describing fractions of heat removal to the cooled surfaces of cavities, temperature fields within the cavity under steady-state and transient conditions, and local heat flux distribution on the bottom curved surface of liquid pools. In general, the modeling is based on solving two-dimensional energy conservation equation with taking into account the effect of anisotropic heat conduction. Effects of natural convection are modeled by means of "pseudo-convective" terms and effective diffusivity coefficients. The heat-driven effective velocities are calculated using a heat-balance treatment and experimental correlations of heat transfer coefficients on the cooled boundaries.

It is perhaps instructive to note that, although the method is able to portray all most significant features of natural convection heat transfer in heat-generating liquid pools, it is restricted by the un-

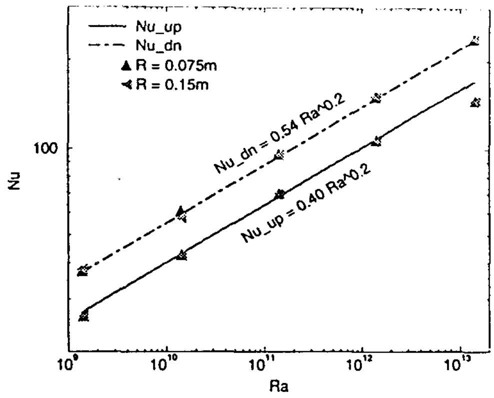

Figure 16: Average Nusselt numbers (hemisphere pools).

certainties of the utilized analytical and experimental correlations. In that sense, the present model can hardly be used to obtain new physical insights into the laminar/turbulent natural convection flows and heat transfer in internally heated liquid (melt) pools. However, the developed method provides an excellent technique for handling the core melt pool, formed inside the decay heated debris bed and located on the lower head of the reactor pressure vessel, when a large number of physical phenomena are involved. The characteristics of molten pool during its formation, namely the pool temperature field and the heat fluxes imposed on pool boundaries, can be properly modeled by this robust and efficient modeling approach. These informations are needed for evaluating the mode and timing of vessel failure as well as parameters of melt discharged from reactor vessel upon its failure.

NOMENCLATURE

Arabic

C	Specific heat, J/(kg.K)
Fo	Fourier number, $Fo = \frac{\alpha \cdot t}{L^2}$
h	Heat transfer coefficient, W/(m.K)
k	Thermal conductivity, W/(m^2.K)
L	Characteristic length, m
Nu	Nusselt number, $Nu = \frac{q \cdot L}{k(\theta_w - \theta)}$
Pr	Prandtl number, $Pr = \nu/\alpha$
Q_v	Volumetric heat flux, W/m^3
Ra	Rayleigh number, $Ra = \frac{q_v L^5}{\alpha k \nu} g\beta$
u, v	Velocity components on vertical and horizontal
x, y	Horizontal and vertical space directions

Greek

α	Thermal diffusivity, m^2/s

β	Coefficient of thermal expansion, 1/K
ν	Kinematic viscosity, m^2/s
ρ	Density, kg/m^3
θ	Temperature, K
θ^*	Dimensionless temperature, $\frac{\theta-\theta_w}{q_v L^2/2k}$

Subscripts

w	wall

References

[1] M.J. Tan, D.H. Cho, and F.B. Cheung, *Thermal Analysis of Heat Generating Pool Bounded From Below by Curved Surfaces.* J. Heat Transfer, Vol.116, pp.127-135, 1994.

[2] Cheung, F.B., Shiah, S.W., Cho, D.H., and Tan, M.J., *Modeling of Heat Transfer in a Horizontal Heat-Generating Layer by an Effective Diffusivity Approach.* ASME HTD-Vol.192, pp.55-62, 1992.

[3] C.J. Kim and M. Kaviany, *A Numerical Method for Phase-change Problems with Convection and Diffusion.* Int.J. Heat Mass Transfer, Vol.35(2), pp.457-467, 1992.

[4] H.S. Carslaw and J.C. Jaeger, *Conduction of Heat in Solids.* Oxford Press, 1959.

[5] F.A. Kulacki and A.A. Emara, *Steady and Transient Thermal Convection in a Fluid Layer with Uniform Volumetric Energy Sources.* J. Fluid Mech. Vol.83, part 2, pp.375-395, 1977.

[6] F.A. Kulacki and M.E. Nagle, *Natural Convection in a Horizontal Fluid Layer With Volumetric Energy Sources.* J. Heat Transfer, Vol.97, pp.204-211, May 1975.

[7] T.C. Chawla and S.H. Chan, *Heat Transfer From Vertical/Inclined Boundaries of Heat-Generating Boiling Pools.* J. Heat Transfer, Vol.104, pp.465-473, 1982.

[8] U. Steinberner and H.H. Reineke, *Turbulent Buoyancy Convection Heat Transfer with Internal Heat Sources.* Proceedings of the 6th Int. Heat Transfer Conference, Toronto, Canada, Vol.2, pp.305-310, 1978.

[9] V.S. Arpaci, *Buoyant Turbulent Flow Driven by Internal Energy Generation.* Int. J. Heat Mass Transfer, Vol.38(15), pp.2761-2770, 1995.

[10] F.A. Kulacki and R.J. Goldstein, *Thermal Convection in a Horizontal Fluid Layer with Uniform Volumetric Energy Sources.* J. Fluid Mech. Vol.55, part 2, 271-287, 1972.

[11] J.H. Min and F.A. Kulacki, *An Experimental Study of Thermal Convection with Volumetric Energy Sources in a Fluid Layer Bounded From Below by a Segment of a Sphere.* Proceedings of the 6th Int. Heat Transfer Conference, Toronto, Canada, paper NR-27, 1978.

[12] M. Jahn and H.H. Reineke, *Free Convection Heat Transfer with Internal Heat Sources: Calculations and Measurements.* Proceedings of the 5th Int. Heat Transfer Conference, Tokyo, Japan, Vol.3, paper NC-2.8, 1974

[13] K.M. Kelkar, R.C. Schmidt, and S.V. Patankar, *Numerical Analysis of Laminar Natural Convection of an Internally Heated Fluid in a Hemispherical Cavity.* Proceeding of National Heat Transfer Conf., San Diego, pp.355-364, 1992.

Paper No. 3

Numerical Modeling of Heat-up and Melting Processes in Internally Heated Debris Bed and Reactor Vessel Lower Plenum

V.A. Bui, T.N. Dinh, and B.R. Sehgal
Nuclear Power Safety Div., Royal Institute of Technology
Brinellvägen 60, 10044 STOCKHOLM, SWEDEN

ABSTRACT

The paper considers the two-dimensional thermal processes in internally heated oxidic debris beds in the lower plenum of a light water reactor vessel during the course of severe accidents with core meltdown and relocation. Heat transfer and phase change processes in debris beds and vessel lower head wall are investigated numerically with a particular emphasis on the dynamic characteristics of thermal transients in question. The main purpose of the work is to develop an appropriate modeling approach, which enables the analysis of complicated physical processes (involving dynamic changes of bed porosity, anisotropic heat transfer in remelting beds with internal energy sources) in complex domains of debris bed and vessel lower head wall. The natural convection heat transfer in the forming melt pools are described by means of an originally developed effective conductivity-convectivity approach. A multi-block control-volume numerical scheme for two-dimensional cartesian or cylindrical non-orthogonal geometries has been developed and applied to predict heat transfer in the solid or porous core debris beds and forming melt pools.

INTRODUCTION

Phenomena of in-vessel melt-structure interaction in a reactor pressure vessel (RPV) lower plenum are of paramount importance in the modeling of severe (meltdown) accident progression in light water reactors (LWRs).

During a course of severe reactor accidents, large amounts of molten core materials are relocated from the reactor core to the lower head plenum to form a decay-heating debris bed. Geometrical, structural, and thermal characteristics of such a debris bed (like mass, composition, porosity, and temperature of debris) depend very much on the accident scenario.

A number of experimental and analytical works have been initiated and performed to improve the current knowledge about the physical nature of core melt - reactor vessel interaction and lower head failure; see e.g. [1]. Among various analytical methods, numerical simulation is a powerful instrument, which can be used to describe the above-mentioned complicated physical phenomena and their inter-dependencies. Sensitivity studies were also performed to consider the effects of parameters, such as debris porosity, debris-to-gap resistance, reactor coolant pressure, and heat transfer conditions on the outer surface of the vessel lower head. Though all these parameters are highly uncertain, the study shed a light on the significance of these factors on the thermal and structural behavior of the reactor vessel. It is worth noting that the mathematical and physical models of different severe accident codes are varying from code to code. Due to the complicated nature of the physical phenomena and the present shortage of knowledge about them, each model employs a set of simplifying hypotheses and assumptions in modeling heat mass transfer processes in complex domains of melt and vessel and vessel failure mechanisms.

The present paper describes the development of a computational method, which can be used to integrally analyze the thermal transients occurring inside the complex-geometry system of debris bed and reactor vessel wall and to assess several factors, which may have significant importance in predicting these transients. Such factors may be the characteristics and configuration of an inhomogeneous core debris bed, the nature of heat transfer processes inside the debris bed and vessel wall, and the thermal interaction between them. More specifically, the heat transfer processes inside the debris bed and vessel wall may involve the heat transfer due to radiation, the heat-up and melting of the debris bed, the formation of the core melt pool and the heat transfer inside the convection-dominated melt pool, the local melting of the vessel wall due to melting or strength failure. From the "simulation" point of view, each of these processes and phenomena is an appealing problem and is difficult to be addressed rigorously. Moreover, the coupling nature of them during the course of interested transients makes the analytical approaches using advanced methods combining the simulations of heat transfer by conduction, radiation, and turbulent natural convection with phase change, to be difficult to be realized. At the same time, the simplified approaches using the single-point analysis could give just limited meaningful description of the dynamics of the involved, inter-related processes and phenomena. Therefore, the development of a modeling approach, which can reasonably describe the related physical phenomena and characteristics, and, at the same time, be simple enough to implement in an integrated reactor safety code, is still a challenging problem.

MODELING APPROACH

Governing equation and numerical treatment method

The modeling development is based on the mathematical formulation of the energy conservation equation, derived for a two-dimensional general curvilinear coordinate system (cartesian and cylindrical axisymmetric) [2]. The equation includes some modifications to take into account the anisotropic heat conduction, which are based on the assumption about homogeneous orthotropic characteristic of the thermally anisotropic medium. The resulted energy conservation equation in a general curvilinear coordinate system (ξ, η) has the following form:

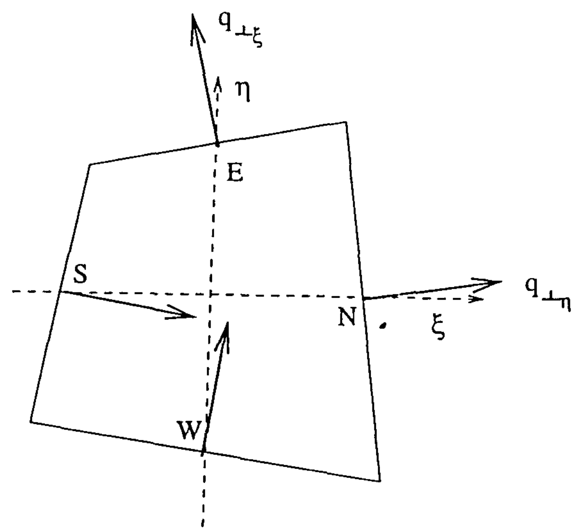

Figure 1: *A computational control volume.*

$$x = x(\xi, \eta), \;\; y = y(\xi, \eta) \tag{1}$$

$$\frac{\partial}{\partial t}(\bar{J}\rho C\theta) + \frac{\partial}{\partial \xi}(\rho C V \theta) + \frac{\partial}{\partial \eta}(\rho C U \theta) = = \frac{\partial}{\partial \xi}\left(\frac{\alpha_\xi k_\xi}{h_\xi}\frac{\partial \theta}{\partial \xi}\right) + \frac{\partial}{\partial \eta}\left(\frac{\alpha_\eta k_\eta}{h_\eta}\frac{\partial \theta}{\partial \eta}\right)$$

$$- \frac{\partial}{\partial \xi}\left(\frac{\beta_\xi k_\lambda}{h_\eta}\frac{\partial \theta}{\partial \eta}\right) - \frac{\partial}{\partial \eta}\left(\frac{\beta_\eta k_\lambda}{h_\xi}\frac{\partial \theta}{\partial \xi}\right) + \bar{J}S(\xi,\eta) \quad (2)$$

where

$$\bar{J} = x^n J, \qquad J = x_\xi y_\eta - y_\xi x_\eta \quad (3)$$

$$U = x_\xi u - y_\xi v, \qquad V = y_\eta v - x_\eta u \quad (4)$$

$$\alpha_\xi = x^n h_\xi h_\eta^2 / J, \qquad \alpha_\eta = x^n h_\eta h_\xi^2 / J \quad (5)$$

$$\beta_\xi = x^n h_\lambda h_\eta / J, \qquad \beta_\eta = x^n h_\lambda h_\xi / J \quad (6)$$

$$h_\xi = (x_\xi^2 + y_\xi^2)^{1/2}, \qquad h_\eta = (x_\eta^2 + y_\eta^2)^{1/2} \quad (7)$$

$$h_\lambda = x_\xi x_\eta + y_\xi y_\eta \quad (8)$$

and

$$k_\xi = \frac{k_x y_\eta^2 + k_y x_\eta^2}{h_\eta^2} \quad (9)$$

$$k_\eta = \frac{k_x y_\xi^2 + k_y x_\xi^2}{h_\xi^2} \quad (10)$$

$$k_\lambda = \frac{k_x y_\xi y_\eta + k_y x_\xi x_\eta}{h_\lambda} \quad (11)$$

By specifying appropriate thermal conductivity coefficients k_x, k_y (without using the convective terms), the above-developed heat transfer equation can be used to describe some cases of heat transfer due to natural convection [3][4]. The particular models of the effective thermal conductivities k_x and k_y depend on the geometry and the boundary conditions of the system under consideration. In this work the convective terms will be modeled by means of a new effective convectivity approach and used in combination with the effective diffusive terms in order to describe the natural convection heat transfer in the forming core melt pool.

The complex geometries of the investigated objects (reactor vessels and debris beds) are treated by dividing them into several computational domains, which are "sewed" together by some heat balance treatment. The computational domains can be connected directly or indirectly with taking into consideration a layer, having a definite heat transfer coefficient, lying between them. In future, this option will be used to model the gap heat transfer between the debris bed and the vessel wall.

The above-developed energy conservation equation is solved iteratively on all computational domains. The values of temperature on the inter-domain boundaries are redefined after each iteration and are used as the domain boundary conditions for the next iteration. The convergence of iterative procedure is defined by controlling the heat balance inside the system.

Convective heat transfer modeling

In the formed decay-heated melt pool, convective heat transfer is the dominated heat removal mechanism, which defines the ratio of heat removals to the boundaries. Since in reactor cases, the natural convection occurs at very high Rayleigh numbers (up to 10^{16}), the application of complicated turbulence models has proved to be unefficient. Recently, a new method for modeling natural convection heat transfer, named as effective diffusivity-convectivity approach, has been developed to describe the heat transfer parameters of heat generating fluid layers and pools [5]. In general, the modeling approach is based on some effective treatment of the convective and diffusive terms of the energy conservation equation, without solving the momentum equations. The heat transfer inside a internally heated, convective melt pool, cooled from all boundaries, is assumed to be driven by two mechanisms: (1) the vertical movement of stratified fluid layers; and (2) the heat transfer to the side wall through a boundary layer, developing downwards along the cooling wall. The first mechanism is modeled by means of a newly developed approach, named as effective convectivity approach, in which the velocities of the convective term (eqn.2) are analytically defined from the pool characteristics. Some treatment has been introduced in order to ensure the mass conservation inside the system, which is based on the redistribution of the mass flows on boundaries to the inner computational nodes. This approach was successfully applied to describe the heat fluxes and temperature distribution inside heat-generated fluid layers cooled from top and bottom [5]. In such cases, when the side cooling takes place, the second mechanism is introduced and modeled using the effective diffusivity approach, which was firstly developed by Cheung et al. in references [3][4] (for cartesian coordinate system only). The combination of above two modeling approaches allows to describe the heat transfer inside fluid layers or pools, cooled from all boundaries.

Recently, this convective heat transfer model has been validated against the data, received by COPO and UCLA experimental studies, which were performed in order to investigate the natural convection heat transfer inside internally heated liquid pools at the high range of Rayleigh numbers ($1.34 \cdot 10^{14}$-$1.61 \cdot 10^{15}$ in COPO and 10^{11}-10^{14} in UCLA experiments). The COPO experiments were based on using a two-dimensional "slice" of the Loviisa torospherical lower head (including a portion of the cylindrical vessel). In UCLA experiments the pools had spherical form and contained Freon-113, which was volumetrically heated using microwave energy. For both cases, the developed convective heat transfer modeling approach was shown to be able to give not only the correct heat transfer coefficients on the cooling surfaces but also the right heat flux distributions on the cooling side wall for all investigated values of Rayleigh numbers (see [6]).

Phase change modeling

The phase change in a remelting debris bed is described by a fixed grid, temperature-base, enthalpy method [7]. This approach is a single region formulation, wherein one above-mentioned governing equation can be used to describe the energy conservation in all phase-change regions. From a single enthalpy conservation equation, which is common for the solid, liquid, and interfacial (mushy) regions, the following heat transfer equation, which has a form similar to eqn.2, can be derived:

$$\frac{\partial(\rho C^o\theta)}{\partial t} = \nabla \bullet (\rho C^o \mathbf{U}\theta + k\nabla\theta) - \frac{\partial(\rho C^o\theta_m)}{\partial t} - \frac{\partial(\rho S^o)}{\partial t} \qquad (12)$$

where $C^o(\theta^*)$ and $S^o(\theta^*)$ are determined from

$$C^o(\theta^*) = \begin{cases} c_s & (\theta^* < -\delta\theta) \\ c_m + \frac{L}{2\delta\theta} & (-\delta\theta \leq \theta^* \leq \delta\theta) \\ c_l & (\theta^* > -\delta\theta) \end{cases} \qquad (13)$$

$$S^o(\theta) = \begin{cases} c_s\delta\theta & (\theta^* < -\delta\theta) \\ c_m\delta\theta + \frac{L}{2} & (-\delta\theta \leq \theta^* \leq \delta\theta) \\ c_s\delta\theta + L & (\theta^* > -\delta\theta) \end{cases} \qquad (14)$$

The specific heat and the heat conductivity of the mushy phase has been taken as the average of those of the solid and liquid phases; i.e., $c_m = (c_s + c_l)/2$.

HEATUP AND MELTING OF DEBRIS BED AND VESSEL WALL

The approach and models, developed in this work, are applied to investigate the processes of heat-up and melting of an initially solid debris bed, located in the lower head of reactor vessel (figure 2). The debris bed is bounded from top by a flat surface and from bottom by the vessel wall, which has a spherical from. The heat is transferred by radiation from the debris bed to the above structures, which have a constant temperature of 1000 K. The reactor vessel is externally cooled by water, so the temperature of the outer vessel surface is assumed to be kept at 378 K. The physical geometry of the debris bed and the reactor vessel is presented by six computational domains (three for the debris bed and three for the vessel wall). The total number of computational nodes is 4814 (figure 3).

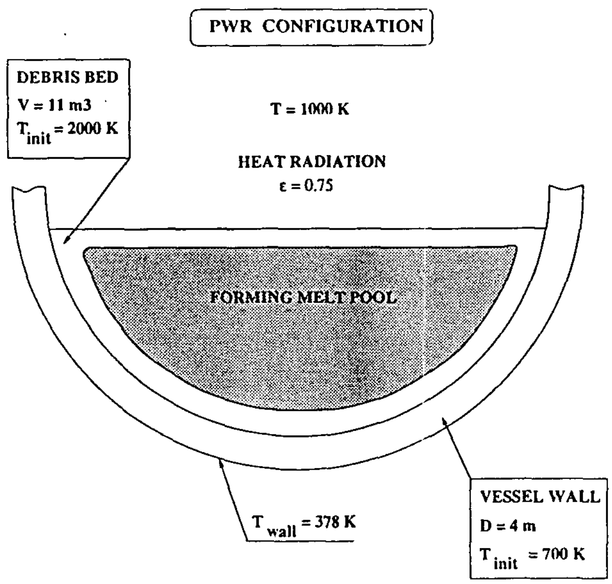

Figure 2: *The initial and boundary conditions.*

With the internal heat generation inside the debris bed set to 0.85 MW/m^3 and the initial debris temperature equal to 2000K, a time span of about 4 hours is needed by the system to dissipate 100% of this energy. With time step equal to 150s, approximately 1.5 hours of CPU time (on HP-700 workstation) is needed to simulate 4 hours of real time process. The melting inside the debris bed begins after about 2.5 hours (figure 4). It is interesting to note that , because of the large size of the debris bed and the relatively low heat conduction coefficient inside it, the effect of the cooled boundaries are rather weak and the debris bed heats up almost uniformly. As a result a large part of the debris bed reaches the melting temperature at the same moment and the initial melt pool already occupies a large portion of the debris bed. After the beginning of melt pool formation the natural convection heat transfer becomes more important and the heat flux to the vessel wall departs from the uniform distribution and its distribution will take the form similar to that of a pure heat-generated fluid pool (figure 5).

A steady-state inside the system is reached after about 4 hours. At this time the core melt pool already occupies a large part of the debris bed, but is still enveloped by a crust layer. As can be seen from figure 6, the thickness of this crust layer varies around the peripheral of the melt pool. The layer may be very thin at the top and upper side part of the melt pool, where the heat fluxes are very high. Along the side boundary the distribution of the crust thickness is almost inversely corresponding to the distribution of the heat flux. It is worth noting that, despite the heat diffusion effect of the crust layer, the ratio of the heat removals upwards and sidewards from the debris bed at the steady-state remains similar to that of a pure melt pool

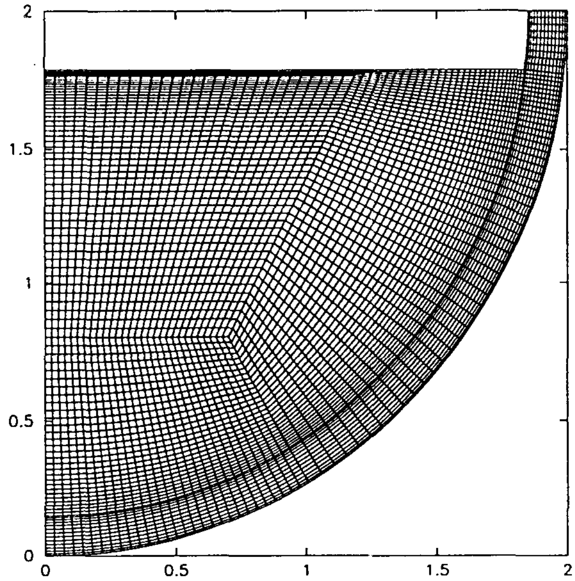

Figure 3: *The computational grid (6 blocks).*

of the same parameters.

The computational results also show that, at the steady-state, the reactor vessel wall may partially melt down. The heat transfer regime inside such a molten layer may be an interesting subject for further investigation. Some sensitivity analyses showed that the assumption about the effective heat transfer coefficient inside such a layer may have a strong effect on the existence of the debris crust layer above it.

CONCLUSION

In this work the complicated phenomena of heat transfer and phase change inside a heat-generated core debris bed, located on the lower head of PWR vessel have been modeled. The modeling approach is based on the energy conservation equation, derived for a two-dimensional, general curvilinear coordinate system, with taking into consideration the orthogonal anisotropy of heat conduction inside the investigated objects. Major efforts have been concentrated on the development of an appropriate model of natural convection heat transfer inside the forming core melt pool, which has proved to be reasonably correct and efficient. All separate mathematical and physical models of the relevant phenomena have been implemented into a computer code, which is then applied to analyze the thermal transient inside the system of the core debris bed and the reactor vessel in a scenario of severe accident with core melt-down and relocation. While calculational results indicate that the modeling approach is efficient and capable of providing a realistic picture about the physical processes in question, there is a clear need for further model validation and improvement basing the results of future analytical and experimental works.

NOMENCLATURE

Arabic

C, c	Specific heat, $J/(kg.K)$
L	Characteristic length, m; Latent heat, J/kg
Nu	Nusselt number, $Nu = \frac{h \cdot L}{k}$
Pr	Prandtl number, $Pr = \nu/\alpha$
Ra	Rayleigh number, $Ra = \frac{q_v L^5}{\alpha k \nu} g\beta$
$\mathbf{U}$	Velocity vector
h	Heat transfer coefficient, $W/(m^2.K)$
k	Coefficient of thermal conductivity, $W/(m.K)$
q_v	Volumetric heat generation rate, W/m^3

Greek

α	Thermal diffusivity, m^2/s
β	Coefficient of thermal expansion, $1/K$
ν	Kinematic viscosity, m^2/s
ρ	Density, kg/m^3
θ	Temperature, K
θ^*	$= \theta - \theta_m$

Subscripts

l	Liquidus
m	Melting point; Mushy
s	Solidus

References

[1] J.L. Rempe et al. *Light Water Reactor Lower Head Failure Analysis.* NUREG/CR-5642. EGG-2618. 1993.

[2] C.J. Kim, S.T. Ro, and J.S. Lee, *A Efficient Computational Technique to Solve the Moving Boundary Problems in the Axisymmetric Geometries.* Int.J. Heat Mass Transfer 36(15), pp.3759-3764, 1993.

[3] M.J. Tan, D.H. Cho, and F.B. Cheung, *Thermal Analysis of Heat Generating Pool Bounded From Below by Curved Surfaces.* J. Heat Transfer 116, pp.127-135, 1994.

[4] F.B. Cheung, S.W. Shiah, D.H Cho, and M.J Tan, *Modeling of Heat Transfer in a Horizontal Heat-Generating Layer by an Effective Diffusivity Approach. Thermal Hydraulics of Severe Accidents*, ASME HTD-Vol. 192, pp.55-62.

[5] V.A. Bui and T.N. Dinh, *Modeling of Heat Transfer in Heat-Generating Liquid Pools by an Effective Diffusivity-Convectivity Approach.* Proceeding of the 2nd European Thermal-Sciences Conference, Rome Italy, 1996.

[6] V.A. Bui, T.N. Dinh, and B.R. Sehgal, *Prediction of Thermal Transients during In-Vessel Core Melt Pool Formation.* A paper submitted to the 1996 National Heat Transfer Conference "Fundamental Phenomena in Severe Accidents", Houston, Texas, August 3-6, 1996.

[7] Y. Cao and A. Faghri, *A Numerical Analysis of Phase-Change Problems Including Natural Convection.* J. Heat Transfer 112, pp.812-816, 1990.

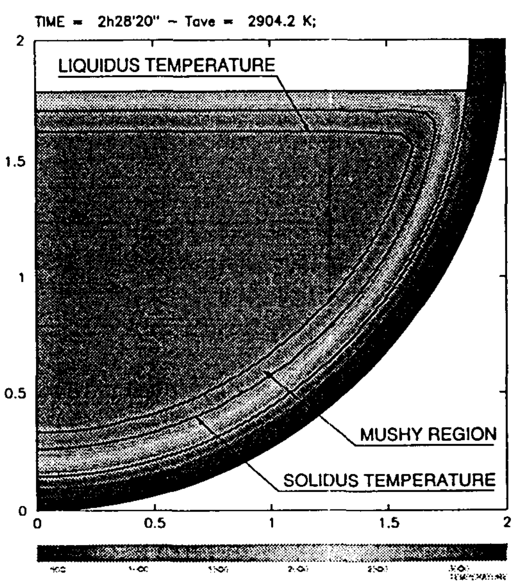

Figure 4: *Initial PWR melt pool, time* $= 2h28'$ $(q_v = 0.85\, MW/m^3)$.

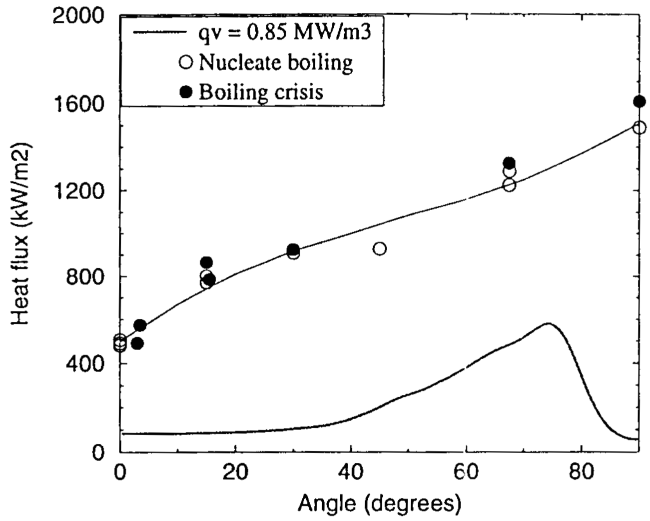

Figure 5: *Heat flux distribution on the outer surface of the vessel.*

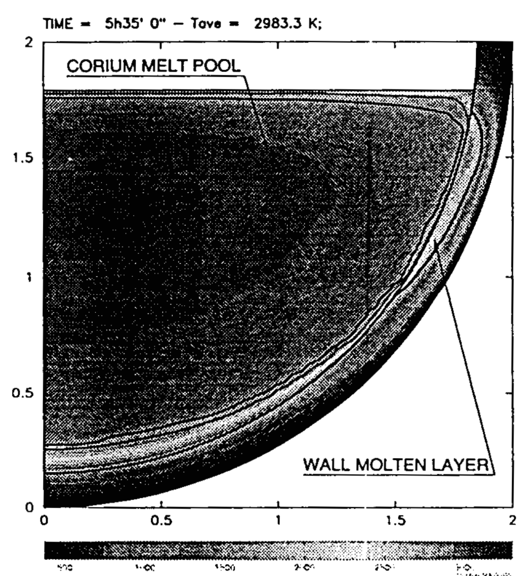

Figure 6: *PWR melt pool at steady-state, ($q_v = 0.85\,MW/m^3$).*

Paper No. 4

CRUST DYNAMICS UNDER PWR IN-VESSEL MELT RETENTION CONDITIONS

T.N. Dinh, V.A. Bui, R.R. Nourgaliev, and B.R. Sehgal
Royal Institute of Technology
Division of Nuclear Power Safety
Brinellvägen 60, 10044 STOCKHOLM, SWEDEN
Fax.: (08) 790-7678; e-mail: nam@ne.kth.se

ABSTRACT

In this paper, some aspects of the dynamic behavior of crust layers, enveloping a corium pool under PWR in-vessel melt retention condition, are analyzed. The upper crust layer, though thin, is shown to be generally stable under prototypic reactor conditions. The sideward crust stability is found to be sensitive to the convective heat transfer in vertical molten vessel steel layer. Based on the results of a numerical simulation of the flow and heat transfer in corium, considered as a binary melt, the stabilizing/destabilizing influence of mushy region on crust dynamics is analyzed. The need for further experimental and related scaling groups studies are discussed in this paper.

I. INTRODUCTION

In the last few years, severe accident management has come to the fore as a concept to upgrade the safety of the existing and the future nuclear power plants. In particular, the concept of retaining the molten corium within the reactor vessel by external cooling of the vessel in the event of core melt-down, is chosen as the basic severe accident management strategy for the Finish Loviisa VVER-440 plant and the AP 600 plant. In fact, if it can be shown, through research, that the molten corium, that may accumulate in the reactor pressure vessel (RPV) lower plenum during the in-vessel progression of the postulated severe accident, can be confined within the vessel; all questions about the integrity of the containment become moot.

The existence of sufficient thermal margin to retain the corium pool within the AP 600 vessel was demonstrated in a recent report by Theofanous and co-workers [1]. Specifically, this study analyzed various thermophysical processes in the core debris, as either a solid oxidic debris or as a molten pool, at steady state. It is worth noting, however, that it is of crucial interest to know the likelihood and conditions, under which a steady state configuration of the system can be achieved.

The physical picture can be quantified as follows: (a) a solid crust ($T \leq T_{sol}$) will form a cold boundary for a corium melt; (b) a mushy region will exist between the melt pool and the solid crust - in which the properties will be different - between those for the solid and the liquid corium; (c) a melt pool whose boundary will be at T_{liq}; and (d) the vessel wall under the crust layer may melt to a certain depth depending upon the heat flux upon the wall. In general, the heat flux directed to the boundary of the melt pool will be determined by the natural convection processes, occurring in the pool and not by the crust thickness outside the pool. However, this hold if the solid crust layer is stable and if the mushy region between T_{liq} and T_{sol} behaves like the solid crust i.e., it doesnot have a circulation flow, which may enhance the heat transfer to the walls ans affect the thickness of the solid crust. Furthermore, crust dynamics may play an important role, when the crust thickness δ_{cr} is small enough, so that transient heat conduction and phase change in the crust layer can feedback to the core melt pool's natural convection flow and heat transfer by modifying the pool boundary conditions. Theoretically, periodic self-sustained oscillations were identified by Cheung [2], who investigated heat transfer processes in an internally heated fluid layer, cooled to freezing from above.

The stability of the solid crust bounded, on one side, by molten steel and, the other side, by the mushy layer has not been examined before. The molten steel layer could be quite large in extent at location where heat flux is the highest. These happen to be near the top corners of the melt pool, where the molten steel layer could flow down to the lower location on the pool surface [1]. Alternatively, the steel layer could stay in place and starts a natural convection flow which would enhance the heat transfer or the conductivity of the steel layer. This scenario and its effect on the heat flux to the vessel wall have not been examined so far, and it is the purpose of this paper to do so.

Generally speaking, there exists very limited information about crust behavior under the in-vessel melt retention conditions. The objective of this study is to examine, theoretically and numerically, flow and heat transfer phenomena, which are of potential importance for dynamic behavior of crust under PWR in-vessel melt retention condition.

II. DYNAMICS OF THE CRUST LAYERS

II.1. Upper crust layer

Since the natural convection flow in the upper pool portion is unstably stratified, and the heat transfer structure is inherently unsteady and three-dimensional, the upward heat flux distribution is strongly non-uniform and varied in time; see e.g. [3]. In other words, the lower surface of the upper crust is subjected to the boundary condition, which differs from the uniform, quasi-steady constant heat flux. Local oscillation of the pool upward heat flux can be characterized by the size δ_{blob} and life time τ_{blob} of cooled blobs. Systematic information about blob characteristics is, unfortunately, absent in the literature. In particular, this is due to difficulties in obtaining and processing such data from experiments. In order to generate the appropriate data base, direct numerical simulation (DNS) can be used. DNS of flow and heat transfer in internally heated fluid layers was performed in ref. [3]. A fairly good agreement with experimental data in internally heated fluid layers was achieved. Calculational results were then analyzed to determine the dependencies of δ_{blob} and τ_{blob} on Rayleigh number Ra. Specifically, the characteristic size of blobs is determined as the upper surface- and time-averaged length scale of zones with local heat flux q_s larger than $\overline{q_s} := q_v \cdot H$; here H is the fluid layer's height. It was found, analytically and numerically from the DNS results, that the dimensionless blob size $\frac{\delta_{blob}}{H}$ is a function of Rayleigh number [2].

$$\frac{\delta_{blob}}{H} \simeq 9 \cdot Ra^{-0.27} \tag{1}$$

Analysis of DNS results also revealed the dependency of the maximum descending velocity in the fluid layers as $U_{max} \sim Ra^{0.35}$. If the time scale of flow convection in the layer is defined as $\tau_{conv} = \frac{H}{U_{max}}$, we obtain

$$Fo_{conv} = \frac{\tau_{conv}\alpha}{H^2} \simeq 3 \cdot Ra^{-0.35} \tag{2}$$

The time scale of blob existence, τ_{blob}, however, should be defined as the time required to replace the cooled liquid mass within the blob by ascending plumes of hotter liquid. Based on an analytical model and eq.(2), it was found that

$$Fo_{blob} = \frac{\tau_{blob}\alpha}{H^2} \simeq 13.5 \cdot Ra^{-0.62} \cdot (1 + 9 \cdot Ra^{0.11}) \tag{3}$$

Figs.1-2 depict the dimensionless time scales (Fourier

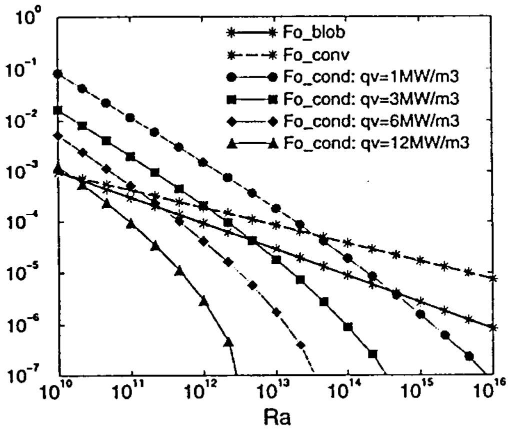

Figure 1: *Crust conduction time scales vs. convection and blob existence time scales.*

numbers) of fluid convection Fo_{conv}, blob existence

[1] Existence and the effects of a molten metal layer, lying separate from the corium pool, are not considered in the present study.

[2] At relatively low Rayleigh numbers, δ_{blob} actually represents the time- and surface-average width of inter-cell cooled structure.

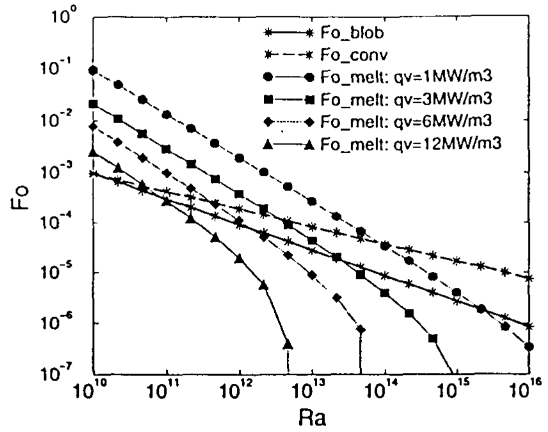

Figure 2: *Crust remelting time scales vs. convection and blob existence time scales.*

Fo_{blob}, conduction front penetration through the crust $Fo_{cond} = \frac{\tau_{cond}\alpha}{H^2}$, and crust remelting $Fo_{melt} = \frac{\tau_{melt}\alpha}{H^2}$. For the given crust thickness δ_{cr}, the time scales for conduction and phase change of crust layer can be determined as $\tau_{cond} = \frac{\delta_{cr}^2}{4\alpha}$ and $\tau_{melt} = \frac{\delta_{cr}\rho_{cr}H_{fus,cr}}{q_v H}$, respectively. Obviously, the heat conduction and phase change time scales increase with the growth of crust thickness. Using the physical properties of corium and correlation of Kulacki and Emara [4], the thickness of the upper crust layer δ_{cr} was found to be a function of the Rayleigh number, Ra, and either heat generation rate q_v or fluid layer height H. The crust thickness decreases with the increase in Rayleigh number and heat generation rate q_v.

It can be seen that, at higher Rayleigh numbers, crust layers are susceptible to thermal attack by ascending flow of hotter fluid. In addition, the higher heat generation rates are, the lower critical Rayleigh numbers Ra_{cr}, at which the crust becomes thermally unstable.

It is of interest to analyze crust behavior in a hemispherical corium pool, contained within the RPV lower plenum of a PWR. Corium melt properties are approximated from [1]. The Steinberner-Reineke correlation ($Nu_{up} = 0.345\ Ra^{0.233}$) [5] [1] and correlation by Theofanous et al. ($Nu_{dn} = 0.0038\ Ra^{0.35}$) [1] are used here to calculate surface-average heat transfer rates to the upper and downward curved pool boundaries, respectively.

Fig.3 shows that even though the upper crust is likely to react to hot melt flow attack, the crust may not be melted through for $q_v < 2MW/m^3$. This estimation was made, however, by using the dependence of the convection time scale on Ra [eq.(2)], obtained for fluid layers. It is believed, however, that the upper portion of hemispherical pool may behave quite similarly to the internally heated fluid layer. Results of the present analysis suggest that the upper crust layer, though thin, is thermally stable under prototypic reactor conditions.

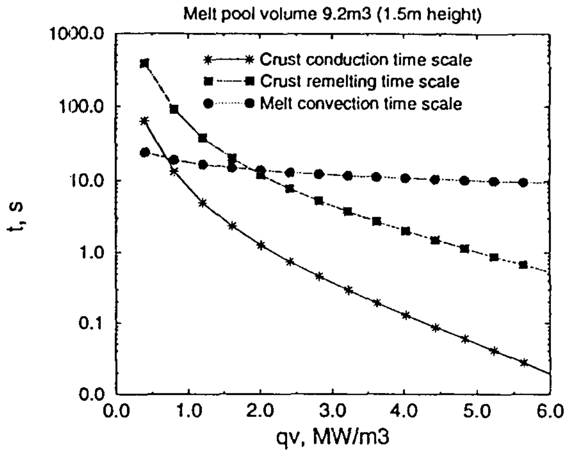

Figure 3: *Time scales of melt pool convection and upper crust heat transfer (reactor case).*

II.2. Sideward crust

Another issue of vital importance for reactor safety is the dynamic behavior (remelting, re-formation, stability) of the sideward crust. In order to be able to remove the heat, which is transferred from the molten corium pool to its curved downward boundary, the vessel steel may partially melt and internal vessel surface may heat up to temperature T_{int} ($T_{int} > T_{mp,w}$). This situation is particularly relevant to the upper part of the crust-vessel interface ($\theta > 45°$), where the local heat flux is high. The quasi-steady conduction analysis indicated that the sideward crust, if it exists, may be floating on top of a layer of molten vessel steel under prototypic reactor conditions. Furthermore, the corium crust may disappear at the pool corner, if the layer of molten vessel steel is assumed to stay, statically, in its original place, and $T_{int} \geq T_{liq,f}$. It was calculated with the heat-conduction approach that up to about 10cm of the vessel steel may be melted away at the pool corner, when q_v is ranging from $1MW/m^3$ to $1.5MW/m^3$.

Convection heat transfer in molten vessel

steel layer

This section considers the convection heat transfer in the vertical molten steel layer on the existence and stability of the sideward crust and its effect. This effect has not been analyzed in previous analyses, related to the in-vessel melt retention. It is worth noting that both temperature difference ($T_{int} - T_{mp,w}$) and molten steel thickness δ_{mw} are sufficiently large to induce natural convection flow within the layer. In fact, the Grashof number of the fluid layer, contained between the crust and solid vessel, defined as $Gr = \frac{g\beta(T_{int}-T_{mp,w})\delta_{mw}^3}{\nu^2}$, may reach 3.10^9, which is fully turbulent in such a condition [6]. Higher the Grashof number is, the higher are the Nusselt number ($Nu_{mw} = \frac{h_{mw}\delta_{mw}}{\kappa_w}$) and corresponding rate of heat transfer through this molten vessel layer.

In this study, we make use of MacGregor and Emery correlation (4), obtained under constant-heat flux condition [3].

$$Nu_{mw} = 0.046(Gr \cdot Pr)^{1/3} \tag{4}$$

The heat transfer coefficient, $h_{mw} = \frac{q_s}{T_{int}-T_{mp,w}}$, can be determined, for a given heat flux q_s, as follows.

$$h_{mw} = 0.1\left(\frac{g\beta q_s \kappa^3}{\nu^2}\right)^{1/4} Pr^{1/4} \tag{5}$$

It can be shown that effective heat conductivity through the molten vessel layer ($\kappa_{eff,mw} = h_{mw}\delta_{mw}$) may be enhanced as much as 20-50 times. Consequently, T_{int} decreases and the crust thickness increases. The thickness of corium crust layer, calculated from eq.(5), is shown on fig.4 for a reactor case with pool height of 1.5m and heat flux peaking factor of 1.8. The computational results show that the corium crust does exist in the entire range of heat generation rate. These findings are in contrast to the result of calculation, in which only heat conduction in the vertical molten steel layer is assumed.

Fig.4 presents the calculated dimensionless parameter $\frac{\delta_{cr}}{\delta_{cr}+\delta_{mw}}$ for two cases, with and without natural convection heat transfer in the vertical molten steel layer. Principally, the beginning of the RPV wall melting can serve as the first regime transition criterion for crust dynamics, because the sideward crust may behave in significantly different ways before and after the vessel melting starts.

[3]When applying correlation (4) to reactor conditions of interest, there exist uncertainties, associated with the validity range of Pr and Gr numbers; see [6], p.266.

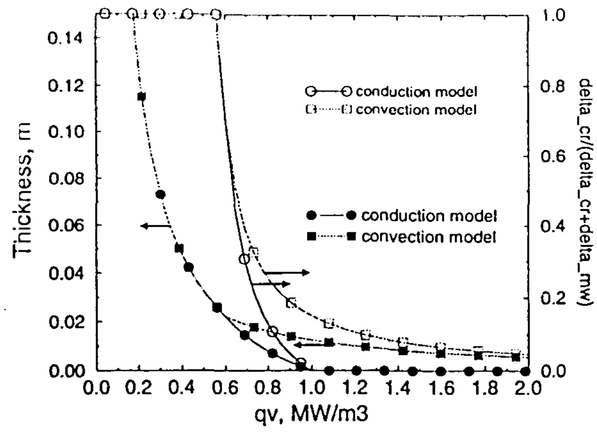

Figure 4: *Thicknesses of corium crust layer, δ_{cr}, and dimensionless group, $\frac{\delta_{cr}}{\delta_{cr}+\delta_{mw}}$, in the cases with and without natural convection heat transfer in the vertical molten steel layer.*

Interestingly, accounting for the convection heat transfer in the vertical molten steel layer does not change much the crust thickness and the dimensionless parameter $\frac{\delta_{cr}}{\delta_{cr}+\delta_{mw}}$, until the Grashof number Gr and conductivity ratio $\frac{\kappa_{eff,mw}}{\kappa_{mw}}$ of the layer reach 2.10^7 and 7, respectively. It is notable that accounting for convection in the vertical molten steel layer has significant effect on corium crust behavior in the most probable range of heat generation rate q_v (from $1MW/m^3$ to $1.5MW/m^3$).

Obviously, uncertainties to be resolved are the heat transfer within the vertical molten steel layer and crust instability. Specifically, the thermal consideration is not able to describe convection-induced instability mechanisms, associated with descending flow in the pool boundary layer and ascending flow in the vertical molten steel layer.

III. EFFECTS OF THE MUSHY-PHASE PROPERTIES

III.1. General remarks

It is known that core melt is, at least, a binary melt, which does not feature a distinct freezing point. The solidus T_{sol} and liquidus T_{liq} temperatures vary with the corium composition, namely zirconia vs. urania. Temperature difference between T_{sol} and T_{liq} ranges from 20K to 100K. Transport properties of corium, such as viscosity ν and thermal diffusivity α, also change significantly in the mushy region. A common understanding is that the boundary condition for the core melt pool is the constant liquidus temperature. This formulation assumes the absence of heat transfer mechanisms, other than heat conduction, in the mushy region. The current assessments do not account for fluid dynamics in the mushy region or its presence as such. The liquidus isotherm, assumed as the pool boundary, is not the real pool-crust interface, but only a temperature boundary between the fully liquid phase and the mushy phase. Crystalization of binary melt in the mushy region is associated with ZrO_2 component, while the UO_2 component remains in its liquid state, which renders, thus, conditions for naturally convecting flow in the porous medium of the mushy region. Certainly, the flows in the melt pool and in the mushy region are thermally conjugated and hydrodynamically interactive. In such a case, the freezing structure of the mushy region can be disturbed, eroded, and removed by the pool boundary flows. In addition, the permeability of the mushy region could make the heat transfer interface between the corium flow and crust (at T_{sol}) considerably larger. On the other hand, accounting for the mushy-phase dynamics could significantly thicken the corium (crust) layer, which has $T < T_{liq}$, and hence, decrease the force, which destabilizes the sideward crust. The mushy region is a thermal resistance, which envelops the corium pool. As such, the mushy region can affect the crust feedback, i.e. the overall heat removal from the debris, the pool energy split, and local heat flux distribution. Therefore, a detailed analysis of flow and heat transfer in binary melt system, particularly, in the mushy region, is desirable to understand this phenomenon.

III.2. Heat transfer in the mushy region

III.2.1. Modeling features

Modeling method. In order to investigate the influence of mushy-phase properties on heat transfer from internally heated core melt pool, a set of numerical experiments was performed. A fixed grid numerical modeling methodology for the phase-change problems with convection-diffusion controlled mushy region was applied [7]. The basic feature of this method lies in the representation of the latent heat of evolution and of the flow in the solid-liquid mushy zone by suitably chosen sources. A two-dimensional formulation of flow and heat transfer in a square cavity was chosen for numerical analysis. The CFDS FLOW3D general-purpose code (release 3.3) [8] is used to solve the set of governing equations, namely, equations of mass, momentum, and energy conservation. Additional routines have been implemented to the code to define the source terms as described in [7]. The developed numerical model was successfully validated against computed results by Voller and Prakash for a test problem [7].

Table 1: *Conditions and mushy-phase properties of test cases.*

Case #	Ra	$\Delta T_{mushy} = \frac{\Delta T_{mushy}}{\Delta T_{pool}}$	Φ_o, $10^{-11} m^2$	Phase change model
1-0-0	10^6	0	0	No
1-1-1	10^6	0.56 (5K)	5.56	Yes
1-1-2	10^6	0.56 (5K)	27.8	Yes
1-2-1	10^6	0.28 (2.5K)	5.56	Yes
1-2-2	10^6	0.28 (2.5K)	27.8	Yes
2-0-0	10^8	0	0	No
2-1-1	10^8	0.56 (61K)	5.56	Yes
2-2-1	10^8	0.28 (30.5K)	5.56	Yes

Problem formulation and conditions. The internally heated fluid (corium) was contained in square cavity, with adiabatic top, bottom, and left-hand wall. The right-hand wall was kept at a constant equal temperature, namely, liquidus temperature for a test case without phase change, and solidus temperature for cases with phase change. Such a configuration was chosen due to the fact that it provides simplicity in analyzing calculated results. More importantly, this configuration is believed to be able to capture all major features of flow and heat transfer in the near-wall region of an internally heated corium pool. A non-uniform computational mesh 100x120 was generated and utilized in the finite-difference numerical treatment.

In this work, sensitivity study was performed with respect to Ra number, temperature interval of the mushy phase ΔT_{mushy}, and its permeability coefficient Φ_o (Table 1). Calculations were first performed for two basic cases with $Ra_1 = 10^6$ and $Ra_2 = 10^8$, and without phase change. The calculated melt superheats ($\Delta T_{pool} = T_{max} - T_{liq}$) and surface-average Nusselt numbers are summarized in Table 2. As can be seen from this table, the numerically determined Nusselt numbers are in a reasonable agreement with those, calculated from empirical correlation (6) [5] [9]. Constant a varies in the range from 0.4851 (pp.234-235, [9]) to 0.6 (fig.5, [5]), while constant b is about

0.19 (0.20) from different sources [4].

$$Nu_{exp} = a \cdot Ra^b \tag{6}$$

Table 2: *Calculated heat transfer characteristics. No phase change.*

Cases	Ra	ΔT_{pool}, K	Nu_{ave}	Nu_{exp}
1-0-0	10^6	8.94	6.69	6.69-8.28
2-0-0	10^8	109.1	16.2	16.09-19.87

In other cases with phase change, ΔT_{mushy} was selected to be equal to 56% and 28% of the pool superheat ΔT_{pool}, obtained for the corresponding basic case without phase change. Such proportions between ΔT_{mushy} and ΔT_{pool} are typical for prototypic reactor case. The permeability coefficient Φ_o is a constant, which depends on the specific multiphase region morphology. Since no information about Φ_o of mushy-phase corium is available to us, two values of Φ_o were arbitrarily selected for case studies. The permeability Φ itself is assumed to vary with liquid volume fraction (porosity) ξ according to the Kozeny-Carman equation (7); see e.g. [10].

$$\Phi = \Phi_o \frac{\xi^3}{(1-\xi)^2} \tag{7}$$

III.2.2. Results and analysis

Fig.5 presents the results of numerical modeling, performed for case with $Ra = 10^6$, $\overline{\Delta T}_{mushy} = \frac{\Delta T_{mushy}}{\Delta T_{pool}} = 0.56$, and $\Phi_o = 5.56 \cdot 10^{-11} m^2$. It was found that, besides the flow in the mushy region, general picture of temperature and velocity fields in the molten corium pool in this case is quite similar to those obtained in case without phase change. As can be seen from the focused flow field in the phase-change zone, the mushy region serves as both an expanded crust layer and boundary flow sublayer. The lower the stress level in the mushy-phase boundary layer, the higher the critical Weber number We_{cr}, at which the sideward crust might break due to hydrodynamic instability mechanisms.

Table 3 presents heat transfer results of numerical simulations [5]. It was found that the heat transfer characteristics are sensitive to the mushy-phase permeability (coefficient) Φ_o. The higher the permeability coefficient is, the higher the Nusselt number is (compare cases 1-0-0, 1-1-1, 1-1-2 in Table 3). It is because the higher permeability of the mushy region provides less friction to the flow in the porous medium and, hence, enhances the heat transfer between the corium fluid and solid structure. Consequently, the melt superheat over the liquidus temperature decreases with the increase of the permeability. Apparently, this effect is suppressed, when the thermal resistance in the mushy region becomes much smaller than that in the liquid pool, i.e. $\Delta T_{mushy} << \Delta T_{pool}$. This point can be illustrated by the results $(T_{max} - T_{liq})$, obtained for the cases with reduced temperature ratio, $\overline{\Delta T}_{mushy} = 0.28$ (see cases 1-0-0, 1-2-1, 1-2-2 in Table 3). Furthermore, an increase in Rayleigh number makes the pool temperature less sensitive to the mushy temperature difference ΔT_{mushy} (cases 2-1-1, 2-2-1, Table 3). It is because the mushy region becomes relatively thinner at higher Rayleigh numbers. Similarly, the Nusselt number increases with the decrease of the mushy-phase temperature difference ΔT_{mushy} and, as in a limiting case ($\Delta T_{mushy} \to 0$), the Nusselt number approachs Nu_{ave} of the corresponding basic case without phase change. However, the relative change of Nusselt number $\frac{Nu_{ave}}{Nu^{mod}_{ave}}$ was found to be independent of Rayleigh number and temperature ratio $\overline{\Delta T}_{mushy}$. As shown in Table 3, the relative change of Nusselt number is a function of the permeability coefficient Φ_o.

Fig.6 depicts the local distribution of Nusselt number Nu for the cases with $Ra = 10^6$. The effect of the phase change (mushy region) is more noticeable in the upper portion of the cavity, where the Nusselt number is highest. As can be seen from the picture, the relative Nusselt number distributions $Nu^* = \frac{Nu}{Nu_{ave}}$ are almost coinciding for all the considered cases with and without phase change. Since no local deteriorations were observed, the above described dependencies and physical picture, obtained by analyzing integral data,

[4] An excellent agreement between numerical results and Jahn's empirical correlation [5], obtained for water, $Pr = 6$, could be achieved, if Richards's correction for fluid Prandtl number effect, $\left(\frac{Pr}{0.952+Pr}\right)^{1/5}$ [9], is added to eq.(6).

[5] In order to compare with the phase-change cases, which have ΔT_{mushy}, the Nusselt number in the corresponding basic case was re-calculated to account for a solid crust layer, temperature difference over which is equal to ΔT_{mushy}. From heat conduction solution, it can be shown that

$$Nu^{mod}_{ave} = Nu_{ave} \frac{\Delta T_{pool}}{\Delta T_{pool} + \Delta T_{mushy}} \sqrt{1 + \frac{2\kappa \Delta T_{mushy}}{q_v H^2}}$$

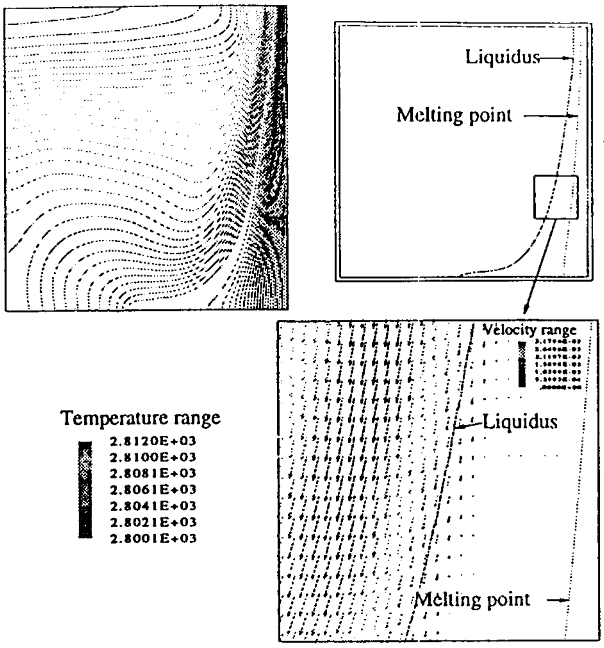

Figure 5: *Isotherms. Configuration of the mushy region. Flow in the mushy region. Case 1-1-1.*

Table 3: *Effects of mushy-phase properties on heat transfer characteristics.*

Cases	$T_{max} - T_{liq}$	Nu_{ave}	$\frac{Nu_{ave}}{Nu_{ave}^{mod}}$
1-0-0	8.94	4.63 (Nu_{ave}^{mod})	1
1-1-1	7.04	4.97	1.07
1-1-2	5.74	5.70	1.23
1-0-0	8.94	5.44 (Nu_{ave}^{mod})	1
1-2-1	7.8	5.81	1.07
1-2-2	6.9	6.39	1.17
2-0-0	109.1	10.74 (Nu_{ave}^{mod})	1
2-1-1	92.6	11.5	1.07
2-0-0	109.1	12.87 (Nu_{ave}^{mod})	1
2-2-1	96.9	13.86	1.08

remain in force.

Although these findings are preliminary, they do indicate that accounting for flow dynamics and convective heat transfer in the mushy region causes higher heat removal rates. This effect is mainly determined by the permeability coefficient Φ_o, which is the major uncertain mushy-phase parameter of the binary oxidic (urania-zirconia) core melt system under consideration.

Finally, it is perhaps instructive to note that the mushy region seems to affect, differently, heat transfer from the corium pool to the upper surface and different segments of the curved downward surface. For given ΔT_{mushy} and Φ_o, the mushy-phase induced heat transfer enhancement is believed to be more significant in convection-controlled portions of the pool, i.e. on the upper surface and pool corner segment. This may, on the first hand, decrease the fraction of downward heat removal, and, on the other hand, result in higher peaking factor in local heat flux distribution on the curved downward surface.

IV. CONCLUSION

In this paper, the thermal hydraulic behavior of the crust layer, which envelops the decay-heated molten corium pool, was investigated in terms of its potential influence on the pool heat transfer and the thermal margin for in-vessel melt retention. Based on results of numerical simulation and the sensitivity study, important phenomena were identified and analyzed. They are: the transient thermal interaction between the upper crust layer and unsteady melt flow; the convection in the vertical molten vessel steel layer; the heat transfer and flow in the mushy zone of the crust. These phenomena are needed to be further experimentally

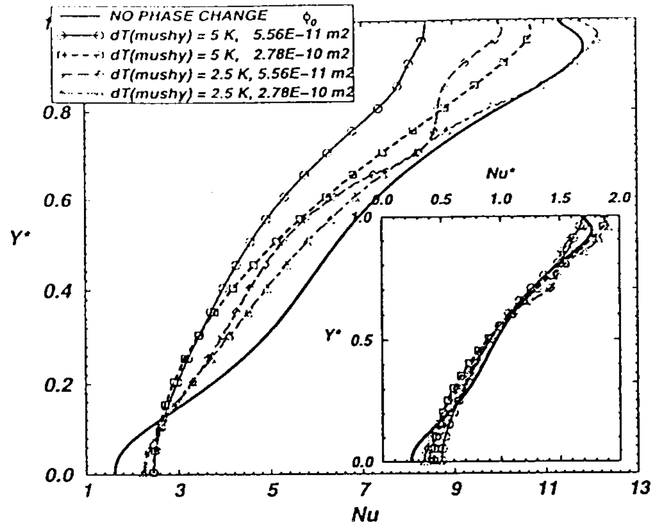

Figure 6: *Local heat flux distribution on the cooled wall.*

investigated.

It was found that the upper crust, though thin, is thermally stable, whereas the sideward crust existence and stability are sensitive to the convective heat transfer in the vertical molten vessel steel layer. The flow and convective heat transfer in the mushy zone of the crust layer are found to have both the stabilizing (from the hydrodynamic point of view) and destabilizing influence (from the thermal point of view) on crust dynamics. The significance level of these effects in reactor case is, however, uncertain, since they strongly depend on a corium property, namely the mushy-phase permeability coefficient.

NOMENCLATURE

<u>*Arabic*</u>

Fo	Fourier number, $Fo = \frac{\alpha \cdot t}{H^2}$
g	Gravitational acceleration, m/s^2
Gr	Grashof number, $Gr = \frac{g\beta(T_{int}-T_{mp,w})\delta^3_{mw}}{\nu^2}$
h	Heat transfer coefficient, W/(m.K)
H	Fluid layer or cavity (pool) height, m
H_{fus}	Heat of fusion, J/kg
Nu	Nusselt number, $Nu = \frac{q \cdot H}{\kappa(T_{pool}-T_w)}$
Nu_m	Mushy-zone Nusselt number, $Nu_m = \frac{q_s \delta_{mushy}}{\kappa \Delta T_{mushy}}$
Pr	Prandtl number, $Pr = \nu/\alpha$
q_v	Volumetric heat generation rate, W/m^3
q	Heat flux, W/m^2
Ra	Rayleigh number, $Ra = \frac{q_v H^5}{\alpha \kappa \nu} g\beta$
t	Time, s
T	Temperature, K
U	Velocity, m/s

<u>*Greek*</u>

α	Thermal diffusivity, m^2/s
β	Coefficient of thermal expansion, 1/K
δ	Size or thickness, m
κ	Heat conductivity, W/m·K
ν	Kinematic viscosity, m^2/s
ρ	Density, kg/m^3
τ	Time scale, s
ξ	Porosity
Φ_o	Permeability coefficient, m^2

<u>*Subscripts*</u>

ave	Surface-average
cr	Crust
dn	Curved (downward) surface
int	Internal surface
l, liq	Liquid, liquidus
$m, mushy$	Mushy
mp	Melting point
mw, w	Molten wall, wall
s, sol	Solid, solidus
up	Upper surface

References

[1] T.G. Theofanous et.al., *In-Vessel Coolability and Retention of a Core Melt*, DOE/ID-10460 (July 1995).

[2] F.B. Cheung, "Periodic Growth and Decay of a Frozen Crust over a Heat Generating Liquid Layer," *ASME J. Heat Transfer*, Vol.103, pp.369-375 (1981).

[3] R.R. Nourgaliev and T.N. Dinh, "An Investigation of Turbulence Characteristics in an Internally-Heated Unstably-Stratified Fluid Layer," *ANS Proc. 1996 National Heat Transfer Conference*, Houston, Texas, August 3-6, 1996.

[4] F.A. Kulacki and A.A. Emara, "Steady and Transient Thermal Convection in a Fluid Layer with Uniform Volumetric Energy Sources", *J. Fluid Mechanics*, Vol.83, part 2, pp.375-395 (1977).

[5] U. Steinberner and H.H. Reineke, "Turbulent Buoyancy Convection Heat Transfer with Internal Heat Sources," *Proc. 6th Int. Heat Transfer Conference*, Toronto, Canada, Vol.2, pp.305-310 (1978).

[6] Y. Jaluria, *Natural Convection Heat and Mass Transfer*, Pergamon Press (1980).

[7] V.R. Voller and C. Prakash, "A Fixed Grid Numerical Modelling Methodology for Convection-Diffusion Mushy Region Phase-Change Problems," *Intern. J. Heat Mass Transfer*, Vol.30, pp.1709-1719 (1987).

[8] *"CFDS-FLOW3D User Guide"*. Release 3.3. User Manual. AEA, UK. 1994.

[9] F.A. Kulacki and D.E. Richards, "Natural Convection in Plane Layers and Cavities with Volumetric Energy Sources", in: *Natural Convection: Fundamentals and Applications*, ed. S. Kakas, W. Aung, and R. Viskanta, Hemisphere Pub. Corp., Washington, pp.179-255 (1985).

[10] W.D. Bennon and F.P. Incropera, "A Continuum Model for Momentum, Heat and Species Transport in Binary Solid-Liquid Phase Change Systems - II. Application to Solidification in a Rectangular Cavity", *Intern. J. Heat Mass Transfer*, Vol.30, pp.2171-2187 (1987).

Paper No. 5

IN-VESSEL MELT POOL FORMATION DURING SEVERE ACCIDENTS

V.A. Bui, T.N. Dinh, and B.R. Sehgal
Division of Nuclear Power Safety, Royal Institute of Technology
Brinellvägen 60, 10044 STOCKHOLM, SWEDEN
Fax (46)(8) 790 76 78.

ABSTRACT

In this paper, the formation of a melt pool in the lower head of an LWR vessel from the initial state of a uniform composition, dried out, debris bed is investigated. The simplified model developed here employs a two-dimensional finite-difference numerical scheme for the solution of a temperature-based energy-conservation equation, which accounts for phase change. The natural convection heat transfer from the melt pool to the boundaries is modeled by an effective convectivity-conductivity approach, which is validated against data from the UCLA and COPO experiments. The heat-up model developed is applied to a BWR scenario, and some of the insights gained are reported in the Summary and Conclusion section.

I. INTRODUCTION AND BACKGROUND

The in-vessel melt progression scenario entails a gradual relocation of the contents of the core into the lower head. During this process of molten core relocation, there are many intense energy transfer processes occuring, as the melt interacts with the large amount of water and heat sinks in the lower head, which are present in all severe accident scenarios. There may be e.g.,(a) the break up and quenching of a melt jet, as happened in the TMI-2 accident (b) possible steam explosions in which the melt may be converted into a very fine debris, while producing much energy in a very short time. These energy transfer processes will occur when the molten core material drops into the lower head water. In time, it is very probable that a debris bed will be formed, whose composition will be based on not only the original core contents but also on some of the contents of the lower head and, perhaps, of the core bottom plate.

Each of the energy transfer processes, occuring during the molten core relocation phase of the in-vessel accident progression, depletes the water in the lower head. In some scenarios, particularly for the PWR, there may not be enough water to completely quench the core melt; and the debris bed formed may contain regions of partially molten core material.

In the event the water supply to the vessel can not be resumed the water in the debris bed formed in the lower head will eventually evaporate. The initially cooled (or fully quenched) debris bed, which is still generating decay heat, will start to re-heat, remelt, and eventually thermally attack the vessel wall. This phase of the accident is of vital importance, since there may be sufficient time available to initiate accident management measures (e.g., restore water supply to the vessel) before the thermal attack on the vessel wall leads to the failure of the latter. The vessel wall is, also, a barrier, which could be employed, with new design, or accident management, approaches, to confine the melt within the vessel. Such a design approach is the vessel external flooding [1][2], which should be able to remove the heat imposed on the vessel wall by the debris bed, and prevent the vessel wall failure.

The heat-up phase of a debris bed to the formation of a melt pool, and potential vessel failure, is the subject of this paper. The general goals are to determine (i) the thermal loading on the vessel wall, as a function of time during this phase, (ii) the time to vessel failure, and (iii) the melt mass and melt superheat that could be available for discharge into the containment, upon vessel failure. The paper is not concerned with the progression of events before the formation of a dried-out debris bed.

II. OBJECTIVES AND ASSUMPTIONS

The specific objective of this paper is to develop a relatively simple methodology for the melt pool formation process, which accounts for some of the key phenomena occuring in the debris bed. We have concentrated on the representation of heat addition, conductive heat transport, debris melting, mushy zone formation, melt pool natural convection, crust dynamics, vessel wall melting, and vessel failure due to melt-through. We have not considered the possibility of vessel failure due to structural and creep loadings prior to its failure due to the wall melt-through.

The transient thermal processes considered are by themselves very complicated. To simplify the model development, we have not considered (i) the chemical heat generation due to zirconium oxidation and its addition-timing during the melt pool formation interval (ii) bed porosity, thereby the change in the volume due to the melting process. Thus, the physical basis for the modeling is as follows:

a) initial state of a zero porosity, spatially uniform composition, particulate, quenched debris bed,

b) spatially uniform decay heat generation in the bed,

c) no chemical heat generation in the bed

d) bed physical properties: thermal conductivity, and specific heat, change with phase change as the bed goes from the particulate to mushy (between solidus and liquidus) and to liquid state,

e) the natural convection process starts as the melt pool is formed, and heat is transfered to the surrounding mushy zone and the particulate bed,

f) the attack of the melt pool (with its crust) on the vessel wall starts when the temperature reaches the wall melting point,

g) the vessel fails due the wall melting process, at which time a certain fraction of the original debris bed is in molten state with a known superheat.

III. PREVIOUS WORK

The most known models for melt pool formation are those incorporated in the codes SCDAP/RELAP [3] and MAAP [4]. The MAAP model employs the lumped-parameter approach with transient pool development controlled by energy balances. It employs chemical heat generation and models the hypothesized in-vessel coolability mechanism. The pool natural convection heat transfer at its boundaries is through chosen correlations.

A model named COUPLE has been added to SCDAP-RELAP, which performs a two-dimensional finite element calculation for the conduction and natural convection processes. Since COUPLE is strictly a heat conduction code, the convective heat flux at the phase change interface is simulated by means of effective conductivities. However, the modeling of natural convection is performed by assigning a large value for thermal conductivity to all liquefied elements, combined with an effective conductivity to the phase change elements at the boundary of the liquefied pool. It is worth noting that the thickness of the phase-change (mushy) region may vary in time and, in the case of a fine computational grid, it is difficult to allocate a unique mushy node to specify the effective heat conductivity.

IV. THERMAL MODEL

The thermal model is based on the solution of the energy conservation equation derived for a two-dimensional general curvilinear coordinate system (cartesian and cylindrical axisymmetric). The equation includes the convective term, which is modeled by means of a new effective convectivity approach, and the diffusive term, which takes into account the anisotropic heat diffusion in the horizontal and vertical directions (different heat conduction coefficients in each direction). The effective diffusive term is then combined with the effective convective term to model the natural convection in the developing core melt pool. The reactor vessel and debris bed are divided into several computational domains, which are "sewed" together by some special treatments. The computational domains can be connected directly, or indirectly through a layer, with definite heat transfer coefficient, lying between them.

A. Natural Convection Heat Transfer Model

In the core melt pool, natural convection is the most important mechanism of heat transfer, which determines the major direction of heat removal. Therefore, correct modeling of the natural convection heat transfer is essential to assess the portion of heat directed to the vessel wall. In the reactor melt pool, due to its large size and high internal heat flux, the Rayleigh number is very high and may range up to 10^{16}. At such Rayleigh numbers, the convection flows are highly turbulent, and the application of traditional approaches, like $k-\epsilon$ models, have limited success. Recently, a new method for modeling natural convection heat transfer, named as effective diffusivity-convectivity approach, has been developed and successfully applied to describe the heat in heat generating fluid layers and pools [5]. In general, the model-

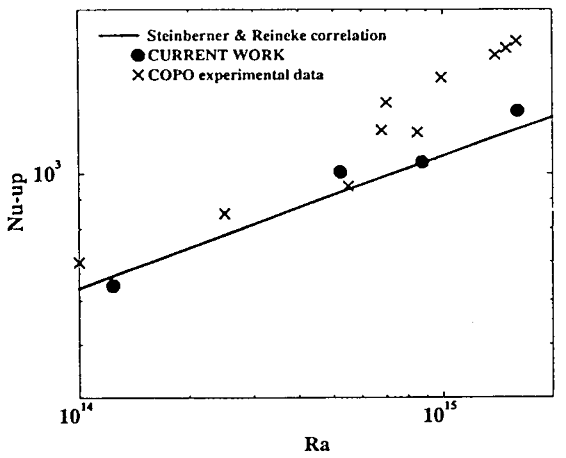

Figure 1: Variation of upward heat fluxes with Rayleigh number.

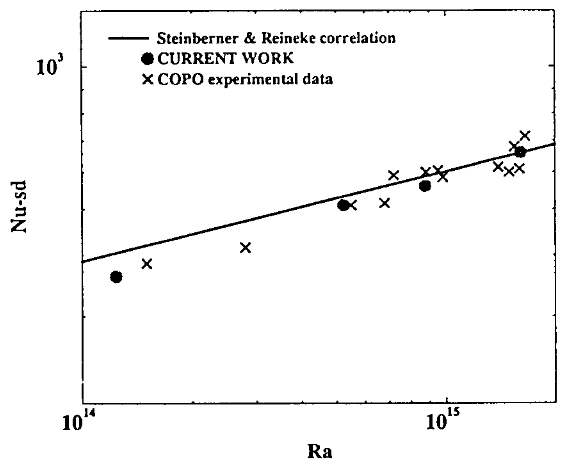

Figure 2: Variation of the heat fluxes on the vertical boundary of the pool with Rayleigh number.

ing approach is based on an effective treatment of the convective and diffusive terms of the energy conservation equation without solving the momentum equation. Natural convection is modeled by means of a "pseudo-convective" term (effective velocities) and effective heat conduction coefficients. The heat-driven effective flow velocities are determined using a heat-balance treatment and empirical, as well as, analytical correlations for boundary heat transfer coefficients. More details about the method can be found in Appendix A.

B. Validation of the Natural Convection Heat Transfer Model

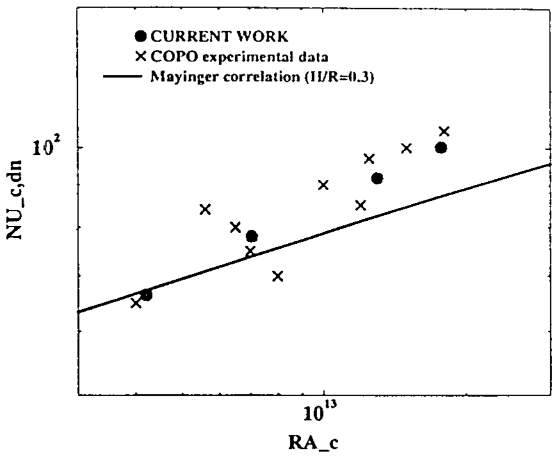

Figure 3: Variation of downward heat fluxes with Rayleigh number.

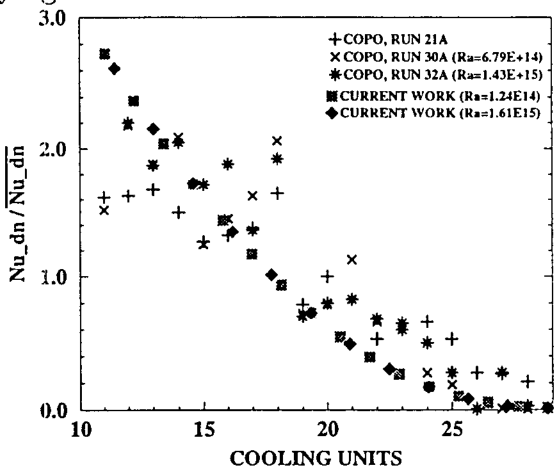

Figure 4: Distribution of heat flux on the lower curved pool boundary.

The proposed natural convection heat transfer model is relatively simple and is based on correlations obtained with relatively low Rayleigh number flow fields. The effective convectivity-diffusivity model is tested against the COPO and the UCLA experiment data, in order to validate it for the high Rayleigh number flow conditions.

COPO and UCLA experimental studies were performed in order to investigate the natural convection heat transfer inside internally-heated liquid pools at the high range of Rayleigh numbers ($1.34 \cdot 10^{14}$-$1.61 \cdot 10^{15}$ in COPO, and 10^{11}-10^{14} in UCLA experiments). The COPO experiments [8] used a two-dimensional "slice" of the Loviisa lower head (including a portion of the cylindrical vessel wall) and $ZnSO_4 - H_2O$ solution, as simulant. The pool was heated by electrical current between flat wall-electrodes. In the UCLA experiments [9], the pool had spherical form and contained Freon-113, which was volumetrically heated using microwave energy.

The calculations were performed for the conditions corresponding to some of the COPO tests: runs No.32f and No.29a with 80cm-depth pool, and runs No.40a and No.42c with 60cm-depth pool. The computational results of Nu_{up}, Nu_{sd}, and $Nu_{C,dn}$ are presented in figures (1-3) together with COPO data and the data given by the correlations for Nu_{up} and Nu_{sd} (Steinberner and Reineke)

$$Nu_{up} = 0.345\, Ra^{0.233} \quad (1)$$

$$Nu_{sd} = 0.85\, Ra^{0.19} \quad (2)$$

and for Nu_{dn} (Mayinger et al.)

$$Nu_{dn} = 0.54\, Ra^{0.18} \left(\frac{H}{R}\right)^{0.26} \quad (3)$$

where H is the pool depth and R is the radius of curvature of the segment.

The predicted heat flux on the side wall (vertical portion) is almost uniform, as confirmed by COPO experimental data. The distribution of the calculated heat flux on the curved portion of the pool is shown in figure 4 and is in good agreement with experimental data.

For comparison with the UCLA experimental data,

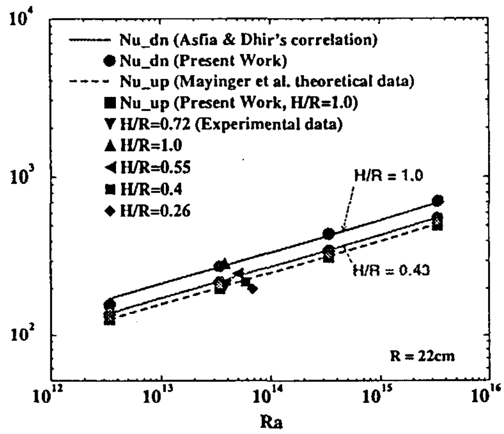

Figure 5: Comparison of the calculated data with other analytical and experimental results.

calculations were performed for hemisphere pools cooled both from flat and curved surfaces with geometrical ratio H/R set equal to 1.0 and 0.43, respectively. The computational results of Nu_{up} and Nu_{dn} are presented in figure 5 in comparison with Asfia and Dhir 's experimental data [9] and Mayinger et al.'s calculations. As reported in Asfia and Dhir's study as well as in studies by other authors, large variation in heat transfer coefficient along the pool curved surface has been observed. The heat transfer coefficient is lowest at the stagnation point and increases almost linearly along the curved surface. The computational result of the heat transfer ratio $Nu_{dn}/\overline{Nu_{dn}}$ is presented in figure 6 along with the measured data of Asfia and Dhir. As seen in the figures, the proposed effec-

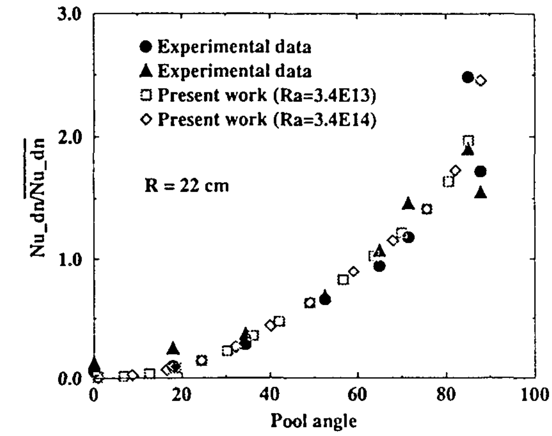

Figure 6: Ratio of local to average Nusselt numbers on the curved wall.

tive convectivity-diffusivity model can, reasonably, describe the portions of heat removed at different cooled surfaces, the distribution of heat flux on the curved boundary, and the average pool temperature for all the cases investigated. We believe that this model will provide adequate heat transfer estimations for the prototypic accident conditions.

C. Phase Change Modeling

In order to model the melting process due to external, or internal heating, the fixed grid enthalpy approach is used. This approach does not trace the exact position of the phase-change interface, thus avoiding the complexity related to grid modification in the numerical scheme. The approach is a single region formulation, wherein one set of governing equations can describe both phases [6]. The enthalpy formulation is based on the assumption of total enthalpy as a dependent variable, along with the temperature, in contrast to the approaches, in which the temperature is the sole dependent variable. In this formulation at a temperature θ around the melting temperatue θ_m, the phase change material is assumed to become mushy. The temperature θ satisfies

$$\theta_m - \delta\theta \leq \theta \leq \theta_m + \delta\theta \quad (4)$$

From a single enthalpy conservation equation, which is common for the solid, liquid, and mushy regions, the following heat transfer equation can be derived [7]

$$\frac{\partial(\rho c^o \theta)}{\partial t} = \nabla \bullet k \nabla \theta - \frac{\partial(\rho c^o \theta_m)}{\partial t} - \frac{\partial(\rho S^o)}{\partial t} + S_c \quad (5)$$

where S_c, the source term, includes the convective term. The heat capacity $c^o(\theta^*)$ and the heat of fusion $S^o(\theta^*)$ are determined from (figure 7)

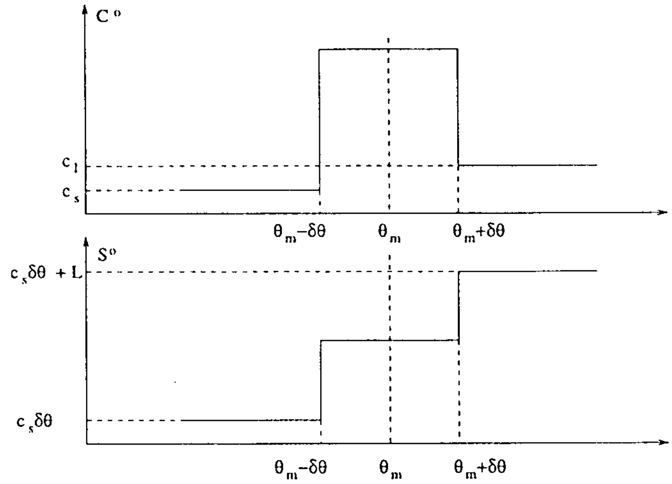

Figure 7: The change of c^o and S^o over mushy region.

$$c^o(\theta^*) = \begin{cases} c_s & (\theta^* < -\delta\theta) \\ c_m + \frac{L}{2\delta\theta} & (-\delta\theta \leq \theta^* \leq \delta\theta) \\ c_l & (\theta^* > -\delta\theta) \end{cases} \quad (6)$$

$$S^o(\theta) = \begin{cases} c_s\delta\theta & (\theta^* < -\delta\theta) \\ c_m\delta\theta + \frac{L}{2} & (-\delta\theta \leq \theta^* \leq \delta\theta) \\ c_s\delta\theta + L & (\theta^* > -\delta\theta) \end{cases} \quad (7)$$

where $c_m = (c_s + c_l)/2$. It is worth noting that equation 5 is similar to the energy conservation equation listed in Appendix A, except for additional source terms and the definition of specific heat. Thus, an energy conservation equation in general form (see Appendix A) can be used to describe the temperature distribution in all regions: solid, mushy, and liquid (while taking into account additional effects of natural convection) by modifying the local properties accordingly.

There is uncertainty about the heat transfer in the mushy region due to its unknown material structure (between solid and liquid). We have assumed that heat conduction is the only prevailing mechanism in the mushy region, with an effective heat conductivity equal to the average of those for the solid and the liquid phases.

V. MELT POOL FORMATION IN A BWR VESSEL

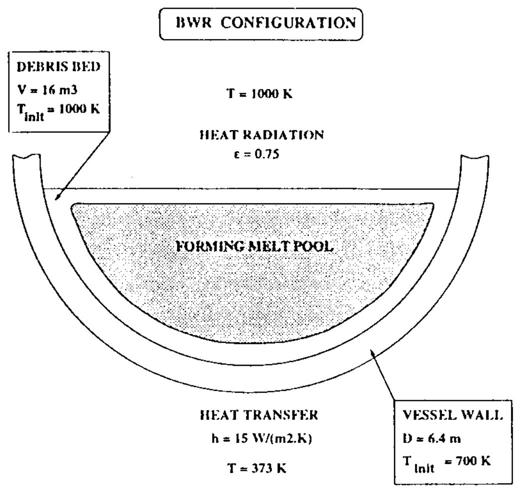

Figure 8: BWR configuration.

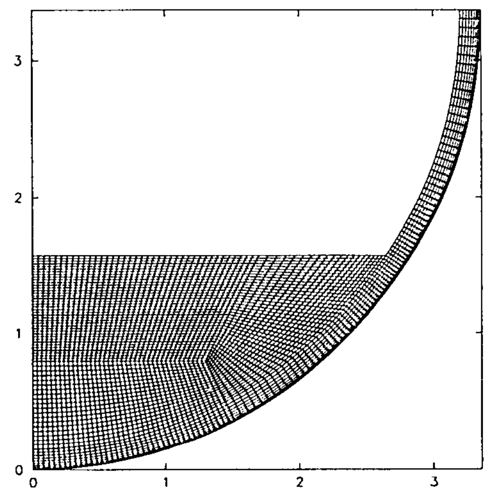

Figure 9: Computational grid.

The BWR core melt pool formation is studied as an example application of the model developed here. The BWR melt progression scenario, in general, should lead to a quenched debris formation in the vessel lower head, since (a) the water volume is large, (b) the melt drop may not be coherent, and (c) the individual flow areas available for melt drop are quite small. The

BWR lower head contains a forest of control rod guide and instrumentation tubes, which will serve as heat sinks during the quench and the debris heat up process. They will also add a substantial amount of metallic melt material to the melt pool, which mey separate from the oxidic melt and form a metallic layer on top of the oxidic melt pool. Additionally, the relocation of the molten material from the original core region to the lower head may be in stages, wherein quenched debris layers of different composition are formed, which on melting may rearrange themselves. There may also be various eutectics formed, whose melting points are quite different from the components forming the eutectics.

The above described complicated picture of the state of the debris bed in the BWR vessel lower head is amenable to analysis, however, our purpose here primarily is to understand the process of melt pool formation in the BWR vessel and to test the application of the models developed above. For this purpose we assume that approximately 135 tonnes of uniform composition, a 1000K-temperature corium debris, whose physical properties are showed in Appendix B, resides in the BWR vessel lower head, and is about to undergo the heat up process. The vessel wall properties are also shown in Appendix B.

Calculations were performed for the BWR lower head with the boundary conditions shown in figure 8. The main purpose of the calculations is to investigate the timing of the heat up transient in the system: core debris-vessel wall until the vessel melt-through.

The physical geometry of the debris bed and the

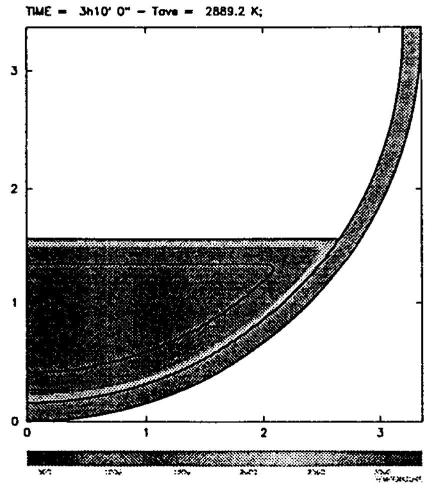

Figure 10: Initial BWR melt pool, $time = 3h15'$ ($q_v = 1.0\,MW/m^3$).

reactor vessel is presented by six computational domains (three for the debris bed and three for the vessel wall). The total number of computational nodes is about 5000 (figure 9).

The timing of the thermal transient in the debris bed and vessel wall, before the melt pool formation, depends on the initial temperature, the decay heat generation rate, and the boundary conditions. It is interesting to note that, because of the large size of the debris bed, and its relatively low heat conductivity, the effect of the cooled boundaries is small; and the debris bed heats up almost uniformly. As a result, a large part of the debris bed reaches the melting temperature at approximately the same time, whence the melt pool occupies a large part of the debris bed.

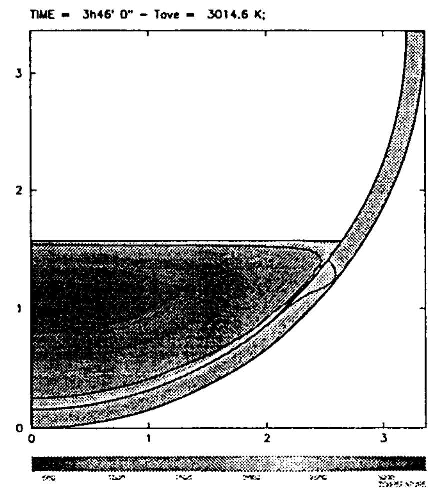

Figure 11: Temperature field at melt-through ($q_v = 1.0\,MW/m^3$).

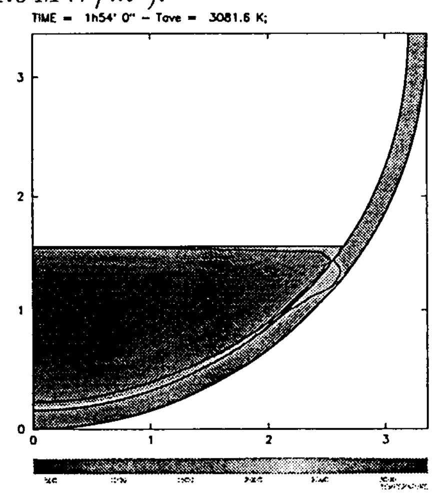

Figure 12: Temperature field at melt-through ($q_v = 2.0\,MW/m^3$).

In the case of a debris bed containing a melt pool, one may expect that the ratio of the magnitude of the heat removed from the debris bed from its top surface to that from the vessel wall, is defined by the heat fluxes on the boundaries of the formed melt pool, and by the thicknesses of the top and side crust. The computational results show that the ratio of the side heat flux to the top heat flux is almost equal to its value for the case of a convective melt pool with constant boundary temperature, and of the same geometry without crust, i.e. the bounding crust has small effect on the energy split of the debris bed. In case the upper crust becomes unstable, or, if it disappears at some places, the melt pool will be exposed and the upper boundary condition will change. In this case, a shift of the energy split with a higher upward heat flux can be expected.

The heat flux distribution on the external surface of the vessel wall is defined by the heat flux distribution on the side boundary of the enclosed melt pool and the diffusive effect of the crust and the vessel wall. A distribution of heat flux, similar to that on the side boundary of a heat generating liquid pool, can be expected. The results of the calculation for the BWR with internal heat generation rate $q_v = 1.0\,MW/m^3$ (total decay power of 16 MW) are shown in figure 10, in terms of the melt pool configuration at 3 hours 15 minutes, when a substantial portion of the initial debris has remained unmelted. Another calculation was performed with $q_v = 2.0\,MW/m^3$ (total decay power of 32 MW), which may represent a faster core meltdown scenario. The end states for these heat input rates, and for an initial debris temperature of 1000 K, are shown in figures 11-12; wherein the melt-through of the reactor vessel wall occurs, respectively, at 3 hours 46 minutes and 1 hour 54 minutes for the values of $q_v = 1.0\,MW/m^3$ and $q_v = 2.0\,MW/m^3$. The pool configurations in figures 11-12 show the vessel failing near the top boundary of the melt pool, where the heat flux has the highest value. The crust at the pool upper surface for the case $q_v = 2.0\,MW/m^3$ is very thin and may, in fact, melt near the middle of the pool. However, in the present calculation, crust is assumed to be stable even if it is very thin. The characteristics of the core melt pool at the time of vessel wall melt through are shown in table 1 for the two BWR cases calculated. It shows that of the initial 135 tonnes of debris material approximately 109 and 118 tonnes are available for discharge to the containment with $q_v = 1.0\,MW/m^3$ and $q_v = 2.0\,MW/m^3$, respectively. The superheat are in the range of 165 K to 232 K.

The above analysis for the BWR ignores the possibility of vessel failure through structural and/or creep loading prior to the melt-through. Ideally, the thermal analysis presented here should be combined with the structural and creep analyses.

Table 1: Characteristics of core melt pool at vessel wall melt-through.

q_v, MW/m^3	Melt mass, *tons*	Superheat, K
1.0	109.07	164.6
2.0	118.07	231.6

VI. SUMMARY AND CONCLUSIONS

In this paper a model to describe the debris bed heat-up process, occuring in the lower head of an LWR vessel, during the course of a severe accident is presented. The model treats the case of a uniform composition, initially quenched, debris bed of zero porosity, which is slowly converted into a melt pool. The hemispherical lower head wall is included in the modeling and its melt-through due to the thermal attack of the melt pool is calculated. The model is based on the solution of the two-dimensional, general curvilinear geometry, energy equation. The anisotropic heat diffusion is modeled, and the heat transport in, and at the boundaries of, the developing melt pool, undergoing natural convection, is described in a subsidiary model. In this sub-model, the heat transport to the upper boundary is through the upward movement of plumes (or layers), whose average velocity is calculated to deliver the requisite heat flux at the upper boundary. The heat transport to the hemispherical boundary is through conduction and then through a boundary layer created by the downward flow along the curved wall from the upper part of the pool. Thus, the temperatures within the pool are calculated. A melt pool is created after the liquidus temperature (appropriate for the melt composition) is exceeded. The vessel melting and melt-through is calculated by following the temperatures in the vessel wall.

The model was applied to a BWR lower head melt pool formation, and vessel melt-through, scenario as an illustration. The heat sinks of the control rod guide and instrumentation tubes were ignored. Also ignored was the presence of any Zircaloy in the BWR debris, which may lead to chemical energy addition.

The calculation showed that due to the relatively low heat conductivity of the core debris, the effect of the cold boundaries does not extend far into the debris bed. Thus, the heat up process is quite coherent for the debris bed. First, a mushy state is reached and, then, a molten state is reached, almost simultaneously, for a substantial fraction of the debris bed volume. The heat-up process would be coherent for a larger fraction of the debris volume in a PWR, since it has a relatively smaller surface/mass ratio than for the BWR lower head.

It was found that the thickness of the crust (debris) around the pool does not affect the split of the heat generation into fractions going to the top and sideward boundaries. It confirms the physically-intuitive observation that the heat flows to the boundaries are directed by the natural convection processes in the melt pool. The crust simply acts as a boundary condition at the liquidus temperature to the melt pool.

There are, currently, many simplifications and assumptions in our models e.g., no chemical reactions, zero porosity, uniform composition etc., which will affect the results calculated here. We envision further development of this model to remove some of the assumptions and approximations made. The models developed here, nevertheless, represent the thermal hydraulic processes quite well and could be incorporated in the codes describing the overall progression of a severe accident.

NOMENCLATURE

Arabic

H	Pool height, m
L	Characteristic length, m; Latent heat, J/kg
Nu	Nusselt number, $Nu = \frac{h \cdot L}{k}$
Pr	Prandtl number, $Pr = \nu/\alpha$
R	Pool radius, m
Ra	Rayleigh number, $Ra = \frac{q_v L^5}{\alpha k \nu} g\beta$
c	Specific heat, $J/(kg.K)$
h	Heat transfer coefficient, $W/(m^2.K)$
k	Coefficient of thermal conductivity, $W/(m.K)$
q_v	Volumetric heat generation rate, W/m^3

Greek

α	Thermal diffusivity, m^2/s
β	Coefficient of thermal expansion, $1/K$
ν	Kinematic viscosity, m^2/s
ρ	Density, kg/m^3
θ	Temperature, K
θ^*	$= \theta - \theta_m$

Subscripts

dn	Downward or bottom boundary
sd	Sideward boundary
up	Upward or upper boundary
l	Liquidus
m	Melting point
s	Solidus

References

[1] T.G. Theofanous, C.Liu, S. Additon, S. Angelini, O. Kymäläinen, T. Salmassi, *In-Vessel Coolability and Retention of a Core Melt.* DOE/ID-10460.

[2] R.E. Henry and H.K. Fauske, *External Cooling of a Reactor Vessel under Severe Accident Conditions.* Nucl. Eng. and Design, 139, 31, 1993.

[3] SCDAP/RELAP5 /MOD 3.1 Code Manual: Damage Progression Model Theory. NUREG/CR-6150 EGG-2720, Vol.2.

[4] MAAP 4 Users Manual, Vol.2, Fauske Associated Inc., 1994.

[5] V.A. Bui and T.N. Dinh *Modeling of Heat Transfer in Heat-Generating Liquid Pools by an Effective Diffusivity-Convectivity Approach.* Proc. of 2nd European Thermal-Sciences Conference, Rome, 1996.

[6] N. Shamsundar and E.M. Sparrow, *Analysis of Multidimensional Conduction Phase Change Via the Enthalpy Model.* J. Heat Transfer 97(3), pp.333-340, 1975.

[7] Y. Cao and A. Faghri, *A Numerical Analysis of Phase-Change Problems Including Natural Convection.* J. Heat Transfer 112, pp.812-816, 1990.

[8] O. Kymäläinen, H. Tuomisto, O. Hongisto, T.G. Theofanous, *Heat Flux Distribution from a Volumetrically Heated Pool with High Rayleigh Number.* Proc. of NURETH-6, vol.1, pp.47-53, Grenoble, France, 1993.

[9] F.J. Asfia and V.K. Dhir, *Natural Convection Heat Transfer in Volumetrically Heated Spherical Pools.* Proc. of the Workshop on Large Molten Pool Heat Transfer, OECE - NEA, pp.229-252, Grenoble (France), 1994.

[10] F.B. Cheung, S.W. Shiah, D.H. Cho, and M.J. Tan, *Modeling of Heat Transfer in a Horizontal Heat-Generating Layer by an Effective Diffusivity Approach.* ASME HTD-Vol.192, pp.55-62, 1992.

[11] F. Mayinger, M. Jahn, H.H. Reineke, and V. Steinbrenner, *Examination of Thermalhydraulic Processes and Heat Transfer in a Core Melt.* BMFT RS 48/1, Institut fur Verfahrenstechnik der T.U., Hanover FRG, 1976.

[12] T.C. Chawla and S.H. Chan, *Heat Transfer From Vertical/Inclined Boundaries of Heat-Generating Boiling Pools.* J. Heat Transfer, Vol.104, pp.465-473, 1982.

APPENDIX A: The Effective Convectivity-Diffusivity Model for the Natural Convection Heat Transfer in Liquid Pools.

The major features of the modeling approach can be stated as follows. The heat transfer inside a natural-convection liquid (melt) pool with volumetric energy source is assumed to be driven by two mechanisms: (a) the *vertical upward* movement of plumes delivering heat to the upper boundary; and (b) the *horizontal* heat transfer to the cooled side wall through the liquid boundary layer developing downwards along the cooled curved wall.

In the present work, the first mechanism is modeled using a new method (named as *effective convectivity* approach), in which the convective heat transfer is defined directly by using the heat transfer coefficients on the boundaries of the melt pool. For the decay-heated melt pools of interest, the effective horizontal velocity is neglected and the effective upward velocity is estimated by the simple correlation

$$\rho c U \simeq h_{up}$$

where h_{up} is the mean upward heat transfer coefficient, which is obtained from the results of numerical study by Mayinger et al. [11]:

$$h_{up} = 0.40 \frac{k}{R} Ra^{0.2}$$

The effective upward velocity U is that of the movement of layers of fluid to the upper boundary. Its value is of the order of 10^{-4} m/s for $Ra \simeq 10^{15}$.

The second mechanism is modeled by means of *the effective diffusivity* approach (Cheung et al.[10]), in which the horizontal heat conduction coefficient k_x for a vertical position y is obtained from the following correlation

$$-k_x \left.\frac{\partial \theta}{\partial x}\right|_w cos\gamma(y) + k_y \left.\frac{\partial \theta}{\partial y}\right|_w sin\gamma(y) = h(\tilde{\theta} - \theta_w)$$

where $\gamma(y)$ is the angle of inclination of the pool side boundary from vertical direction at vertical location y and the vertical heat conduction coefficient k_y is assumed to be unchanged. The heat transfer coefficient h is a function of boundary-layer development length y', counted from the upper edge of the pool side wall. In this work the Eckert-type correlation proposed by Chawla et al.[12] is applied to define h

$$h = 0.508 \frac{k}{y'} Pr^{1/4} \left(\frac{20}{21} + Pr\right)^{-1/4} Ra_{y'}^{1/4}$$

where $Ra_{y'}$ is the local Rayleigh number based on characteristic length y':

$$Ra_{y'} = \frac{\beta \Delta \theta_w g y'^3 cos\gamma(y)}{\nu^2} \frac{\nu}{\alpha}$$

The temperature distribution in the pool is considered to be axisymmetric, two dimensional, and governed by the energy conservation equation, while taking into account homogeneous-orthotropic anisotropic heat conduction

$$\frac{\partial}{\partial t}(x^n \rho c \theta) + \frac{\partial}{\partial x}(\rho c U \theta) + \frac{\partial}{\partial y}(\rho c V \theta)$$
$$= \frac{\partial}{\partial x}(x^n q_x) + \frac{\partial}{\partial y}(x^n q_y) + x^n S(x,y)$$

with $q_x = -k_x \cdot grad\theta$, $q_y = -k_y \cdot grad\theta$, k_x, and k_y are the heat fluxes and heat conductivities on the vertical (x) and horizontal (y) directions, respectively; U, V are the vertical and horizontal velocities; n has the value 0 in the Cartesian coordinate system and 1 in the axisymmetric, cylindrical coordinate system. This equation is then rewritten for a general curvilinear coordinate system (ξ, η) in order to account for the geometry of the debris bed and the reactor vessel.

In general, the approach can provide a reasonable temperature distribution inside the melt pool, a good distribution of heat flux on the curved part of the melt pool, and, more importantly, a satisfactory ratio of heat removed from the top and the curved cooling surfaces.

APPENDIX B: Debris and Wall Properties Used in Calculations.

Property	Debris Solid	Debris Liquid	Wall Solid	Wall Liquid
Density, kg/m^3	8430		7810	
Conductivity, $W/(m.K)$	2.88		32	
Specific Heat, $J/(kg.K)$	445	565	519	
Latent Heat, J/kg	$0.362 \cdot 10^6$		$0.26 \cdot 10^6$	
Melting Point, K	2850		1780	

Paper No. 6

1995-05-15

Experiments on Vessel Hole Ablation During Severe Accidents

B. Raj Sehgal, Jonas Andersson, Nam Dinh, Anh Bui and Timo Okkonen
Nuclear Power Safety, Royal Institute of Technology
100 44 STOCKHOLM Sweden

Abstract

A program of simulant material experiments has been initiated at the Division of Nuclear Power Safety, to investigate the physical processes that occur during the core melt attack on the reactor vessel, and the containment, during the progression of a severe accident. The simulant materials are mixtures of oxides, which melt from 900 K to 1500 K, form crusts and have low viscosity. Specific experiments planned, in the initial program, are on (a) the interaction of melt and vessel and (b) interactions of melt and water.

The first set of experiments on melt vessel interactions, performed with a simulant melt mixture containing Pb0 and $B_2\,0_3$, employ a lead plate as a simulant for vessel wall. The process studied is that of ablation, as the melt is discharged to the containment through the vessel failure location. Preliminary data have been obtained for plates of 20, 30 and 40 mm thickness each with an initial hole of 10 mm diameter. Scaling analysis has been performed and a one dimensional code HAMISA has been completed. A two dimensional code has also been prepared, since it has been observed that the ablation process is two dimensional.

A preliminary set of experiments on melt-water interaction were performed with small quantities of molten Pb0, and water at several values of subcooling. The fraction of melt fragmented varied with the subcooling magnitude.

1. Introduction and Background

Much research has been performed in the last ten years on the phenomenology of the severe accidents in light water reactors (LWRs). Much has been learned and some of the issues relating to containment performance (1) have been resolved. Some areas of the phenomenology, which have received much attention, but have not yet been adequately resolved are; (a) the interaction of corium melt with the lower head vessel wall in the presence, or absence, of water, (b) interaction of the melt jet, on its release from the vessel, with water pools, which may be present in the containment. The major questions of concern here are, (1) the extent of the ablation of the vessel failure location, since that determines the melt jet diameter and the mass rate of corium discharged to the containment, (2) the fraction of the melt jet that will fragment and cool, and the fraction which will not fragment and deposit as a melt pool under water to attack the concrete basemat, (3) coolability of the melt pool under water, (4) the coolability of the particulate debris bed if sub-millimeter size particles are formed and (5) the potential for large steam explosions, which may generate much hydrogen and produce large dynamic loads on the containment.

Several large scale experimental programs have, or are, addressing the issues listed above. These include, FARO (2) and MACE (3), which have used corium materials and had to be supported by a consortium of several nations due to their high cost. The favourite simulant of iron-aluminium has been used at various scales ranging from a few kg, as in the Sandia hole ablation experiments (4), to several hundreds of kg, as in the CORVIS Project (5). The thermite melt suffers from the disadvantages of (a) segregation due to the different densities of Al_20_3 and Fe and (b) the different superheats for Al_20_3 and Fe. Separation of Fe and Al_20_3 has been attempted but the technology is difficult and not always successful.

Our choice for a corium simulant are the oxidic mixtures, which melt from 900 to 1500 K. Several mixtures are feasible, including e.g. mixtures of lead oxide, iron oxide, boron oxide, silicon oxide and others. Since corium melt has been known to have low viscosity, our search led to a mixture of Pb0 and B_20_3. Figure 1 shows the measured viscosities (6) of Pb0 and B_20_3 mixtures, as a function of temperature. It is seen that it is possible to tailor a composition with these two oxides, which would simulate a prescribed temperature variation of viscosity. Our chosen mixture with $\approx$ 75w% Pb0 melts at $\approx$ 950 K, at which temperature the radiation heat transfer and film boiling phenomena, important in the interactions of melt with water, would be active. Oxidic mixtures are generally inert, cheap and easy to handle, and there is an experience base and infrastructure in Sweden for melting large quantities of such mixtures and working with the melt. Additionally, we believe that the development work, necessary to perform the envisaged experiments successfully, will not be expensive and long lasting.

We have not found a data base on corium physical properties vs. temperature. Such a data base would be very helpful in tailoring our oxidic melt compositions to model the corium properties.

2. Objectives of the Overall Research Program

The objectives of the overall research program are to obtain data on the melt-structure-water interactions that occur during the progression of a severe accident, after a core melt has occurred in a LWR and the water in the lower head has been boiled off. Specifically, in the initial three-year program, data will be obtained for,

(a) the ablation process which increases the size of a failure in the reactor pressure vessel, as the melt is discharged into the containment,

(b) the melt fragmentation process that occurs when the melt jet is discharged into a water pool in the containment, as in the Swedish BWRs, or in the simplified boiling water reactor (SBWR). This data could also apply to the case of an in-vessel melt jet-water interaction.

The subsequent research program may be directed to obtain data for,

(1) the spreading process of the melt jet, discharged from the vessel, into a PWR cavity, with, or without, the presence of a water layer,

(2) the coolability process of the unfragmented jet that collects, as a melt pool, at the bottom of the ex-vessel water pool and attacks the concrete basemat,

(3) the coolability process of the fragmented jet that collects as a particulate debris bed, at the bottom of the ex vessel pool and attacks the concrete basemat,

(4) the coolability process of a fragmented debris bed lying on top of the unfragmented melt pool with the latter attacking the concrete basemat. Both the fragmented bed and the melt pool are under water. This configuration is, perhaps, the most likely result of the melt jet and the water pool interaction process.

The melt pool and the particulate debris bed in the experiments investigating the processes (2) to (4) will be heated electrically, as in the MACE tests (3).

An important objective of the experimental program is to gain insight into the physics of the complex phenomena by performing many experiments while changing the controlling parameters. In particular, the emphasis will be to delineate the role of the melt properties e.g. viscosity, thermal conductivity, crust formation, crust strength, liquidus-solidus temperature differences etc.

3. Approach

The approach of the research program is experimental, but coupled with model development based on observations. Scaling relationships will be established, so that the experimental results obtained are appropriate for model validation, and could be applied to prototypical situations. Phenomenological models will be developed for the melt-structure-water interaction processes, and they will be validated against the data obtained. Representative applications of the validated models to the prototypic accident situations will be performed.

The melt employed in the experiments will be an appropriate oxidic mixture melt. The controlling parameters for each interaction studied will be varied systematically. For example, for the hole ablation experiments, the parameters to vary would be (1) the melt superheat, (2) melt volume, (3) wall materials, (4) initial hole size and (6) melt compositions. Similarly for the melt jet-water interaction, the parameters of interest are (i) melt superheat, (ii) melt velocity, (iii) melt jet diameter, (iv) water depth, (v) water subcooling, (vi) melt compositions (to vary the melt viscosity and surface tension). Lists of controlling parameters for the other processes will be developed as those experiments are prepared.

4. Facility

The facility currently used to perform experiments is based in the Metal-Casting division of the Royal Institute of Technology, where there is a small resistance furnace and an induction furnace having capacity of $\approx$ 15 litres of melt. The induction furnace can be raised and tilted to pour the melt into the test apparatus. For heating the oxidic mixtures, a graphite crucible lined with Al_2O_3 is employed. The scoping experiments for hole ablation, described later, have employed $\approx$ 5 litres or $\approx$ 35 kg of melt.

A new laboratory is being developed in the Nuclear Power Safety division, with the procurement and installation of a $\approx$ 5 liter capacity resistance furnace and a $\approx$ 15 liter capacity induction furnace. Later on, a large induction furnace with capacity of approximately 1 tonne of oxidic melt will be obtained, so that relatively large scale experiments can be performed to reduce scale distortions. A concrete-walled cell will be built to contain the melt jet-water interaction experiments.

5. Hole Ablation

The increase in the size of a failure location in a LWR vessel has not received as much attention as it deserves. We believe, that the mass rate of melt discharge and the melt jet diameter are determined primarily by the hole ablation process. Since, the time constant for the flow-caused ablation process is tens of seconds, this process should determine the final size of the vessel failure for all causes of vessel failure, be it a penetration failure, or the global creep rupture (7). An initial opening in the creep-rupture process will be increased very rapidly by the ablation process, thereby the creep process will essentially terminate due to the pressure relief.

Recently, experiments and scaling analysis on hole ablation have been performed at Sandia National Laboratories (SNL), as reported by Pilch in the Appendix J of the Zion PWR direct containment heating (DCH) evaluation report (8). The analysis based on one-dimensional formulation was anchored to the measured data to produce a curve from which the ablated hole diameter was derived for the DCH events. The analysis considered the presence of a crust, however the effect of the crust was not evaluated. The THIRMAL code (9), developed at Argonne National Laboratory (ANL) incorporates a one-dimensional model for hole ablation, with, and without, presence of a crust between the melt and the vessel wall. It was found that the presence of a crust, if sustained, would lead to much lower ablation of the initial failure location (hole).

We believe that the main question in the hole ablation process is whether a crust, formed on the melting vessel wall and subjected to a melt flow, will remain stable or not. Periodic sweeping out and reforming of the crust could be the operative phenomena. A primary objective of our hole ablation experiments will be to delineate the role of the crust.

6. Scaling Analysis for the Hole Ablation Experiments

A scaling analysis, based on that developed by Pilch in the Zion DCH report (8) was applied to the hole ablation experiments envisaged. The scaling parameter is τ_m/τ_D where τ_m is the time required to discharge the melt, resident in the vessel, through the original-size hole and τ_D is the time required to increase the size of the hole by a factor of two. Table 1 compares the values of the scaling parameter for the prototypic reactor accident situations to those for the experiments with the $PbO + B_2O_3$ simulant melt, and a lead plate. It is seen that experiments can be constructed with $\approx$ 10 to 100 l of the simulant melt to obtain the proper values for the scaling parameter. The final hole size for the reactor cases is affected strongly by the presence of the corium crust. The simulant materials (melt and the vessel wall) will be varied to obtain the same effect, as of the corium crust in the reactor cases.

7. Scoping Hole Ablation Experiments

The scoping hole ablation experiments have been performed with $\approx$ 35 kg of the mixture of PbO and B_2O_3 heated in an Al_2O_3 lined graphite crucible placed in the induction furnace. The test section is a steel cylinder $\approx$ 160 mm inside diameter and $\approx$ 400 mm height with a lead plate as the base. A hole of 10 mm diameter is placed at the center of the base plate. Three different lead plates of 20 mm, 30 mm and 40 mm thickness have been employed in these initial experiments. The melting point of lead is 600 K and the melt temperature employed has been ≈ 1150 K. Thus the temperature difference is ≈ 550 K, which is not too different from that prevalent in the reactor accident situations. The melt crystallisation has been measured to begin at ≈ 900 K, when the melt viscosity also rises sharply. Although this can not be signified as solidus temperature, the melt heat transfer and flow behaviour is much like that of a slurry with high solid content.

The induction furnace, the test section and the three lead plates with the ablated holes, are shown in Figure 2. Figure 3 shows the shapes of the ablated holes in the 40, 30 and 20 mm plates after the passage of ≈ 35 kg of melt. It is seen that the ablation process is two-dimensional and that the final size of the hole is a function of the thickness of the plate.

Some pertinent details of the experimental equipment should be mentioned. The cylinder test section is heated, however the lead base plate is thermally isolated and its temperature before the pouring of the melt into the cylinder is kept below 350K. The hole is filled with tin, which melts after all of the simulant melt is poured in the test section. The melt is poured in the cylinder on the top of an umbrella type structure, so that the melt jet does not hit the base plate. The base plate is instrumented with thermocouples placed along 3 radial directions at different depths to obtain data on heat transfer rates and the speed of the ablation front. The lead base plate is cast with the thermocouples in place. The whole apparatus is placed on a weighing machine, so that the mass rate of melt, discharged from the ablated hole, is recorded on the data acquisition system.

8. Preliminary Melt Fragmentation Experiments

A set of very preliminary experiments were performed to observe the feasibility of performing melt fragmentation experiments with the oxidic melt mixtures under our consideration. Small quantities (200 to 300 grams) of Pb0 powder were melted and brought to the temperature of 1050°C (superheat of ≈ 170°C) and dropped into a small tank of water, maintained, at atmospheric pressure, in turn, at subcoolings of 5°, 15°, 25°, 35°, 45° and 93°C. Different magnitudes of the melt fragmentation were observed as the subcooling was increased. The fraction of the melt that fragmented was found to be very small at 5°C subcooling, while all of the melt fragmented at subcooling of 93°C. For the experiment at 35°C subcooling a mild steam explosion was observed, which occurred in the stratified configuration. The melt fragmentations for the subcoolings of 5°, and 93°C are shown in Figure 4. The large amount of steam produced for the 5°C subcooling case resulted in almost spherical particles of millimeter size. The particle sizes for the 93°C subcooling case were of millimeter size; only for the stratified steam explosion event, sub-millimeter size particles were obtained.

9. Hole Ablation Analysis Development

A dynamic analysis of the hole ablation process has been developed and a code HAMISA-1D (hole ablation modeling in severe accidents)has been written. This code solves the melt flow equations in one dimension and performs the heat transfer calculation in cylinerical geometry for melting of the plate, and tracks the ablation front. Thus, the code provides the hole ablation rate and the melt mass discharge rate, as a function of time both of which could be compared to the data obtained in our experiments. The code varies the melt physical properties e.g. viscosity and thermal conductivity as a function of temperature. The equation for melt pool level and the equation for the volume-averaged melt pool temperature are treated

as transient conservation equations. These equations are included in the set of non-linear ordinary differential equations, which are integrated within each time step, using the fourth-order Runge-Kutta method. The accuracy of the numerical solution has been examined through comparisons to analytical solutions, available for limiting cases.
The HAMISA code was used to analyse the hole ablation experiments conducted at SNL (4). The comparison is shown in Table 2, where δ is the ratio of the change in the hole diameter, during the test, to the original diameter of the hole. In general, the comparison is quite good.

Extensions of the one-dimensional treatment in HAMISA have been prepared to model the flow-ablation process as observed in our tests. The version HAMISA-2D includes models for (1) melt flow in two dimensions, (2) crust formation, sweepout and re-formation, (3) hole entrance effects and (4) a two-dimensional moving boundary melt front. A number of separate-effect analytical studies, on the extensions mentioned above, were also performed. The results of a two-dimensional calculation for the hole ablation experiment on the 40 mm thick plate are shown in Figures 5 and 6. Figure 5 shows the transient development of the ablation front and Figure 6 shows the average ablation rate and the radius of the hole at the leading edge as a function of time. The analysis results compare very well with the data obtained. A paper on this analysis development will be presented at the NURETH-7 Conference (10)

10. Near Future Activities

The experiments on hole ablation will be moving into the realm of scalable experiments, as we employ larger quantities of melt and start to systematically vary the controlling parameters. We have initiated scaling analysis for melt-water interactions for the design of the scoping experiments. We will construct a cell, where the melt-water interaction experiments will be conducted. The hole ablation experiments will logically precede the melt-jet-water interaction experiments, to provide the data base for establishing the range of melt jet characteristics (diameter, mass flow rate, temperature etc.).

Analysis development activities will continue for the dynamic processes of melt interactions with vessel and water.

11. Summary

A capability to perform relatively large scale experiments investigating the melt-structure-water interactions that occur after a core melt attacks the vessel, is being developed at the Royal Institute of Technology in Stockholm. The experiments will employ oxidic mixtures, which may be tailored to have temperature dependence of physical properties similar to that of the $U0_2$+$Zr0_2$ mixture of corium. The first set of melt-vessel interaction tests performed are related to the ablation of a vessel failure-location due to the melt discharge from the vessel. In these tests, the reactor vessel wall is simulated by a lead plate. The observations from these tests point to the two-dimensional nature of the ablation process. The first set of melt-water interaction tests performed are related to the extent of melt fragmentation, as a function of the magnitude of subcooling of water

A code HAMISA has been written for describing the hole ablation process. It has been validated against data obtained from experiments performed at SNL. A two-dimensional version, with proper modeling of the crust behaviour, entrance effects and a moving-boundary melting front has being developed, and has been compared against the data obtained in the experiments. Scaling analysis of the melt-water interaction process has been initiated.

References

(1) B.R. Sehgal, "Some outstanding Issues in Severe Accident Containment Performance", Proceedings of the Fourth International Topical Meeting on Nuclear Thermal Hydraulics, Operations and Safety, Taipeh, Taiwan (April 7-8, 1994)

(2) D. Magallon, H. Hohmann, "High Pressure Corium Melt Quenching Tests in FARO", CSNI Specialist Meeting on Fuel Coolant Interactions, Santa Barbara, CA. (5-8 January, 1993); to be published in Nuclear Engineering and Design

(3) B.R. Sehgal et.al., "ACE Program Phase D: Melt Attack and Coolability Experiments (MACE)", Proceedings of the second OECD/CSNI Specialist Meeting on Core Debris Concrete Interaction, Karlsruhe, Germany (April 1-3, 1992) and M. Farmer, B. Spencer and B.R. Sehgal, "MACE Core Coolability Test M1B",Transactions of the Twentieth Water Reactor Safety Information Meeting, Washington D.C., USA, NuREG/CP-0125 (October 1992)

(4) M.M. Pilch, Private Communication. See also reference 8

(5) P. Hosemann, H. Hirschmann, "Corium Vessel Interaction Studies - Status of the CORVIS Project", Transactions of the Twenty-First Water Reactor Safety Information Meeting, Washington D.C., USA, NuREG/CP-0132 (October 25-27, 1993)

(6) Eijima, Kameda, 1967 data, quoted in Mazurin et.al., "Handbook of Glass Data", Part B page 243, Elsevier (1985)

(7) J.L. Rempe et.al., "Light Water Reactor Lower Head Failure Analysis", NuREG/CR-5642, EGG-2618, (October 1993)

(8) M.M. Pilch, "Continued Enlargement of the Initial Failure Site in the Reactor Pressure Vessel", Appendix J in the Report: M.M. Pilch, H. Yan and T.G. Theofanous, "The Probability of Containment Failure by Direct Containment Heating in Zion", NuREG/CR-6075; SAND 93-1535 (June 1993)

(9) J.J Sienicki, S.K. Wang and B.W. Spencer. "Analysis of Melt Arrival Conditions on the Lower Head in U.S. LWR Configurations", Proceedings of the the Fifth International Topical Meeting on Reactor Thermal Hydraulics, NURETH-5, Salt Lake City, Utah, September 21-24, 1992 and J.J. Sienicki et.al. "Ex-Vessel Melt Coolant Interactions in Deep Water Pool": "Studies and Accident Management for Swedish BWRs". Proceedings of the OECD/NEA/CSNI Specialists Meeting on Fuel-Coolant Interactions, Santa Barbara, California, January 5-8, 1993. NUREG/CP-0127. NEA/CSNI/R(93)8.

(10) T.N. Dinh, V.A. Bui, R.R. Nourgaliev, T. Okkonen and and B.R. Sehgal "Modeling of Heat and Mass Transfer Processes During Core Melt Discharge From a Reactor Pressure Vessel", to be presented at NURETH-7 Conference, New York U.S.A (September, 1995)

Table 1: Reactor vs. experimental cases (without crust).

Reactor cases

m_m (tonnes)	V_m (m^3)	h_o (m)	D_m (m)	Δp (bar)	D_h^0 (cm)	τ_m (s)	τ_D (s)	τ_m/τ_D (-)	t_d (s)	$\Delta D_h/D_h^0$ (−)	$D_{h,f}$ (cm)
10	1.25	0.39	2.0	2	2.5	580	1.3	460	13.	10.	28.
				10		270	0.66	400	6.4	9.7	27.
				2	5	140	2.7	53.	12.	4.5	27.
				10		67.	1.4	47.	6.0	4.2	26.
				2	15	16.	8.0	2.0	7.3	0.91	29.
				10		7.4	4.3	1.7	3.6	0.84	28.
150	18.75	1.6	3.9	2	2.5	7900	1.2	6600	31.	26.	68.
				10		3900	0.66	6000	17.	25.	65.
				2	5	2000	2.6	770	31.	12.	66.
				10		980	1.4	700	17.	12.	64.
				2	15	220	7.7	28.	26.	3.4	66.
				10		110	4.2	26.	14.	3.3	64.

2.5 *cm*	PWR or BWR Instrumentation Guide Tube Penetration (average)
5 *cm*	U.S. BWR Drain Line Penetration (if fully open)
15 *cm*	BWR Control Rod Drive Assembly Penetration (if fully open)

Experimental cases

m_m (kg)	V_m (l)	h_o (cm)	D_m (cm)	Δp (bar)	D_h^0 (cm)	τ_m (s)	τ_D (s)	τ_m/τ_D (-)	t_d (s)	$\Delta D_h/D_h^0$ (−)	$D_{h,f}$ (cm)
70	10	25	23.	0	0.5	770	0.91	850	11.	13.	7.1
				2		110	0.43	260	3.4	8.5	4.8
				0	1	190	1.9	100	11.	5.9	6.9
				2		27.	0.90	30.	3.1	3.6	4.6
				0	2	48.	4.0	12.	9.3	2.4	6.7
				2		6.9	2.0	3.6	2.5	1.3	4.5
700	100	50	50.	0	0.5	5400	0.96	5600	23.	26.	14.
				2		1100	0.52	2100	8.7	19.	9.8
				0	1	1400	2.0	700	23.	12.	13.
				2		270	1.1	250	8.5	8.4	9.4
				0	2	340	4.2	81.	22.	5.4	13.
				2		67.	2.3	31.	7.9	3.6	9.1

m_m	Initial melt mass in the vessel
V_m	Initial melt volume in the vessel
h_o	Initial melt pool height above the discharge hole
D_m	Equivalent melt pool diameter
Δp	Vessel gas over-pressure
D_h^0	Initial discharge hole diameter
τ_m	Melt discharge time without hole growth
τ_D	Doubling time of the initial discharge hole diameter
t_d	Melt discharge time
ΔD_h	Increase of the discharge hole diameter ($D_{h,f} - D_h^0$)
$D_{h,f}$	Final discharge hole diameter

Table 2 Comparison of 1D-HAMISA Code Predictions with the Experimental Data from Sandia National Laboratory

N^o	Test	$\bar{\delta}_{exp}$	$\bar{\delta}_{HAMISA}$	deviation,%
1	MICE-6	1.18	1.358	15.0
2	MICE-7	1.56	1.382	-11.4
3	MICE-8	2.37	1.539	-35.0
4	MICE-10	1.65	1.488	- 9.8
5	MICE-11	2.00	1.496	-25.2
6	MICE-12	1.41	1.287	- 8.7
7	MICE-13	1.90	1.492	-21.5
8	MICE-14	1.15	1.208	5.0
9	MICE-16	1.72	1.473	-14.4
10	MICE-17	1.19	1.363	14.5
11	SNL/HIPS-2C	1.48	1.229	-16.9
12	SNL/HIPS-3J	1.56	1.300	-16.6
13	SNL/DCH-1	0.125	0.163	30.0
14	SNL/TDS-4	0.256	0.393	53.5
15	SNL/LFP-1A	0.355	0.354	0.3
16	SNL/LFP-2B	0.244	0.235	- 3.6

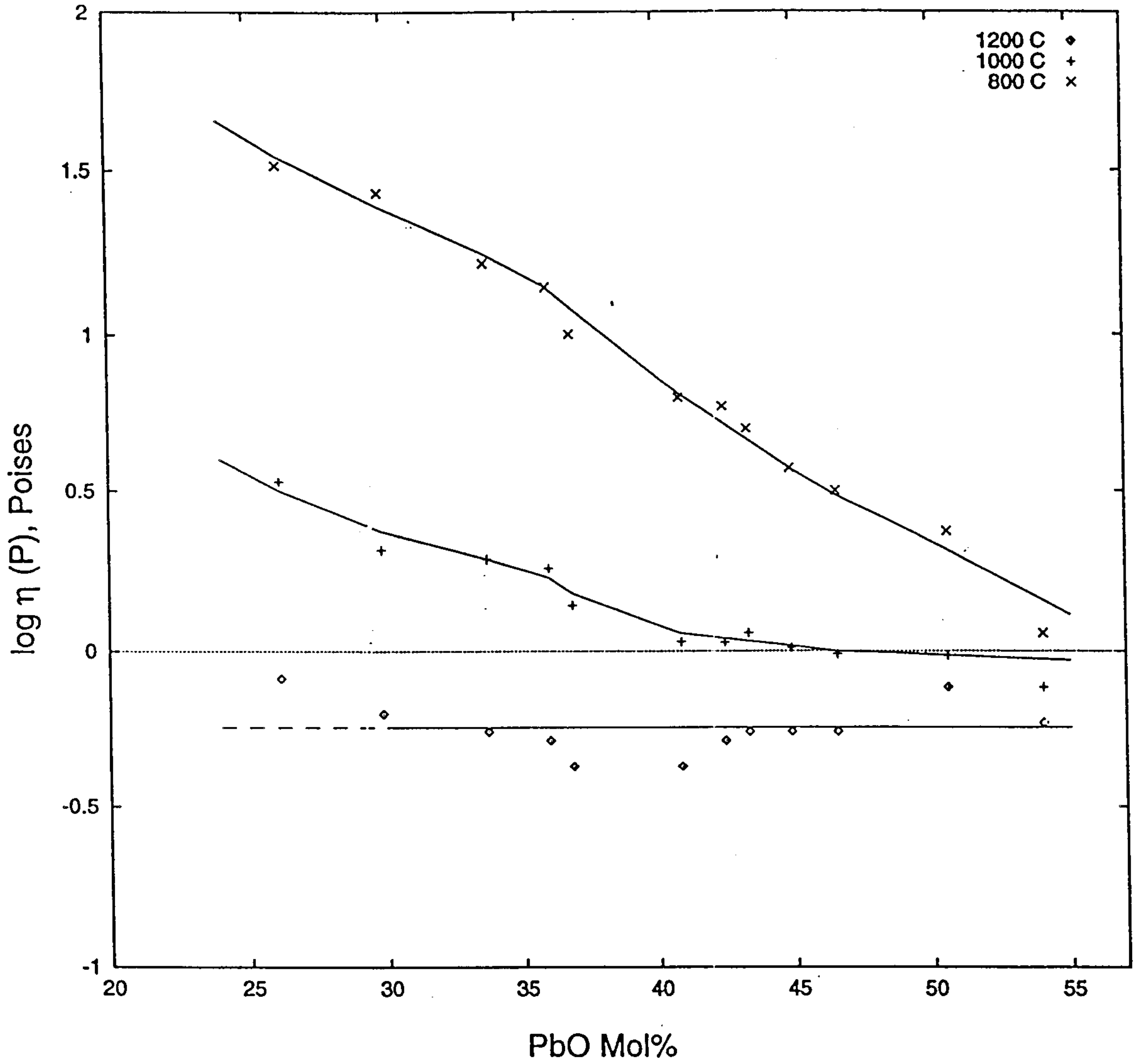

Figure 1. Viscosity of PbO + B_2O_3 Mixtures.

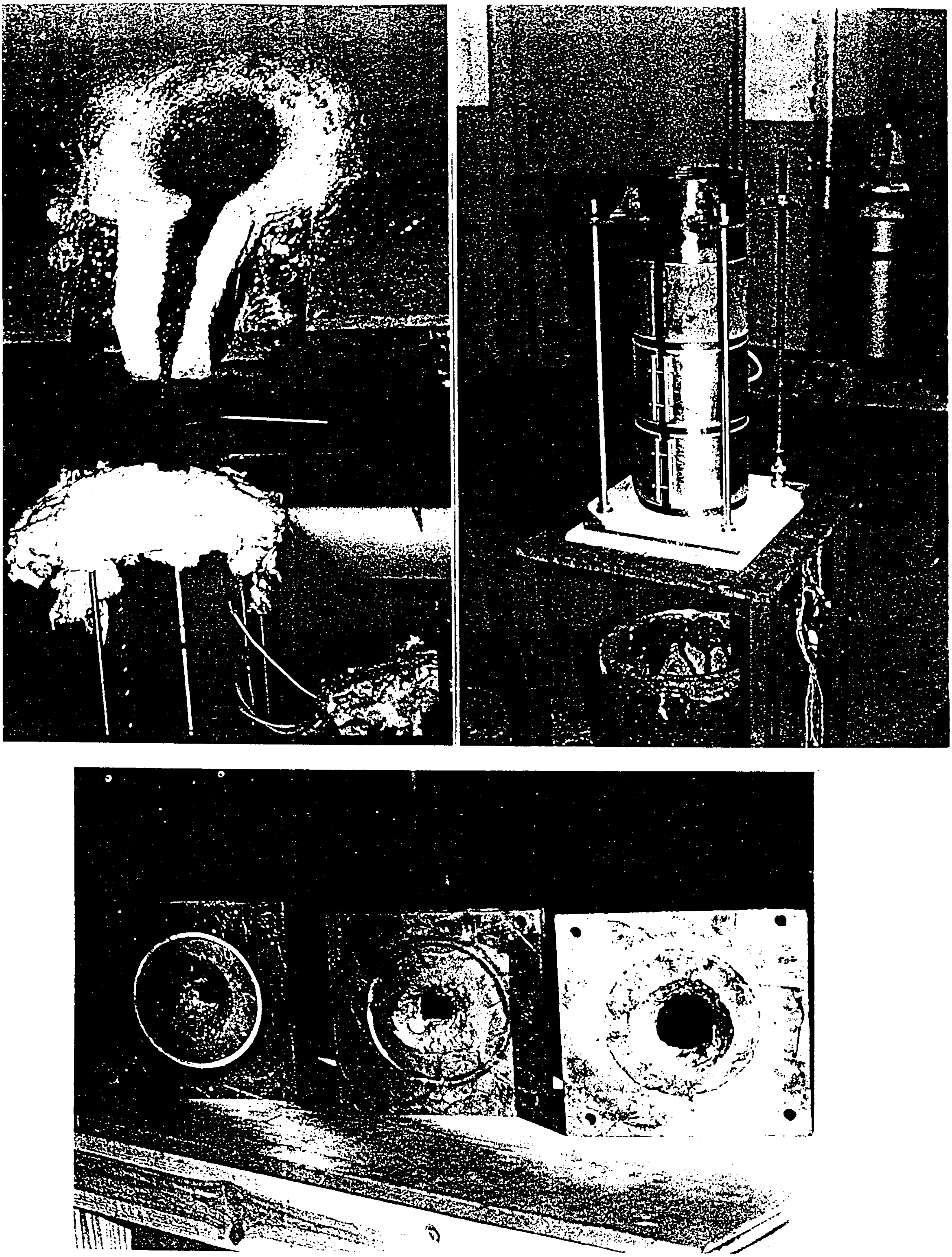

Figure 2   The Furnace, the Test Section and the Ablated Plates

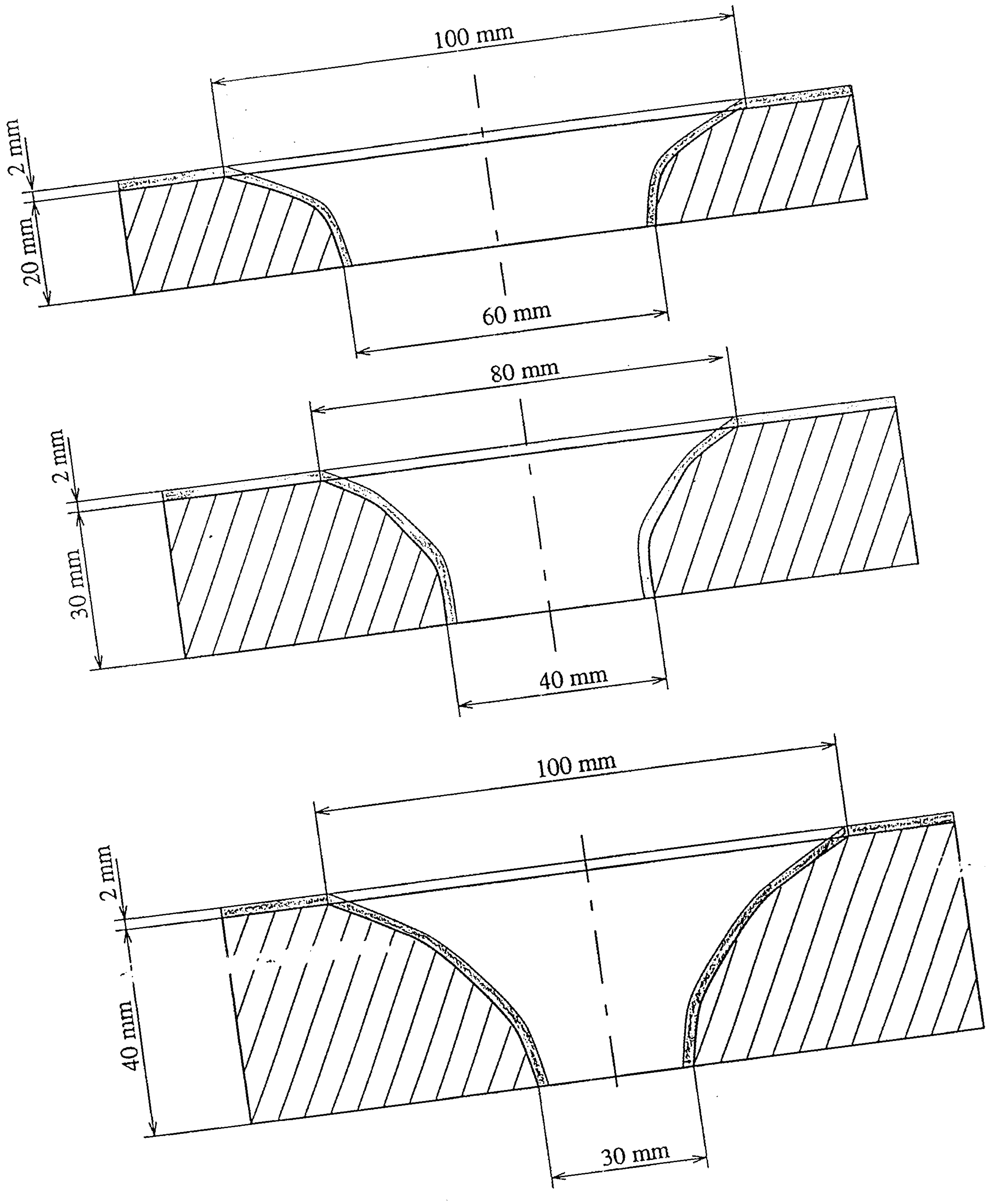

Figure 3. The Shape of the Ablated Holes in the 40, 30 and 20 mm Lead Plates

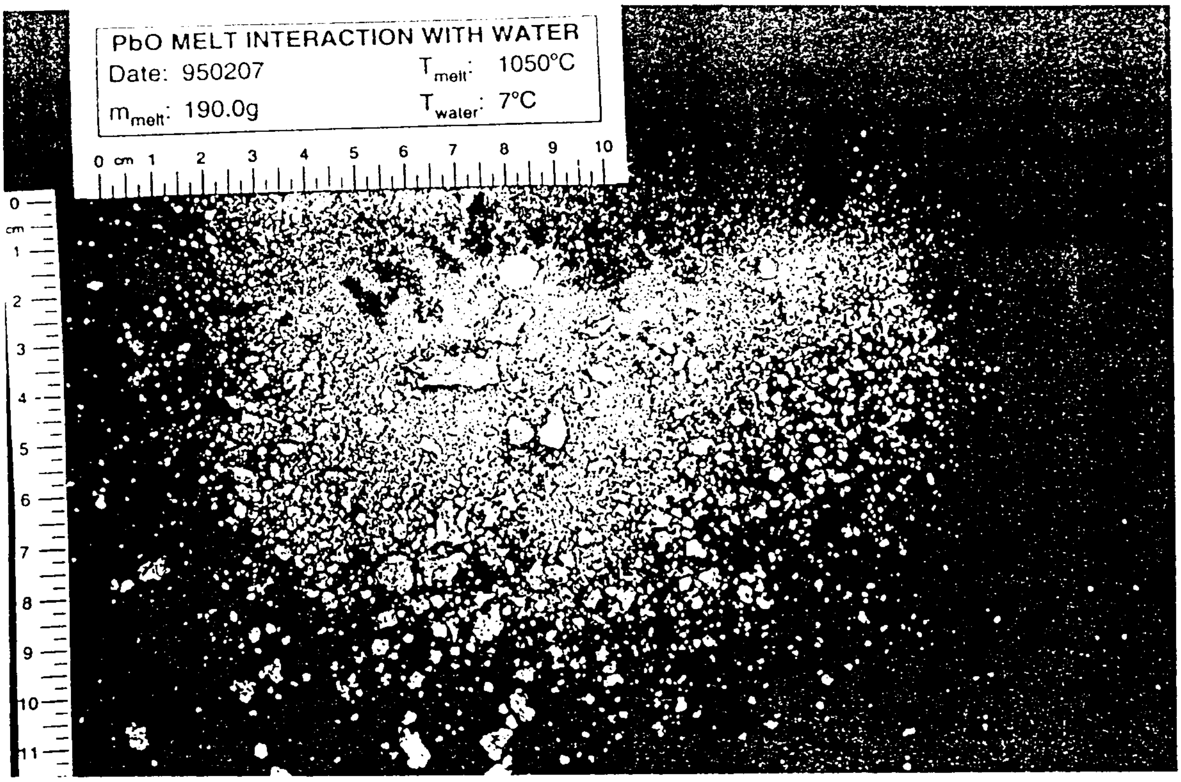

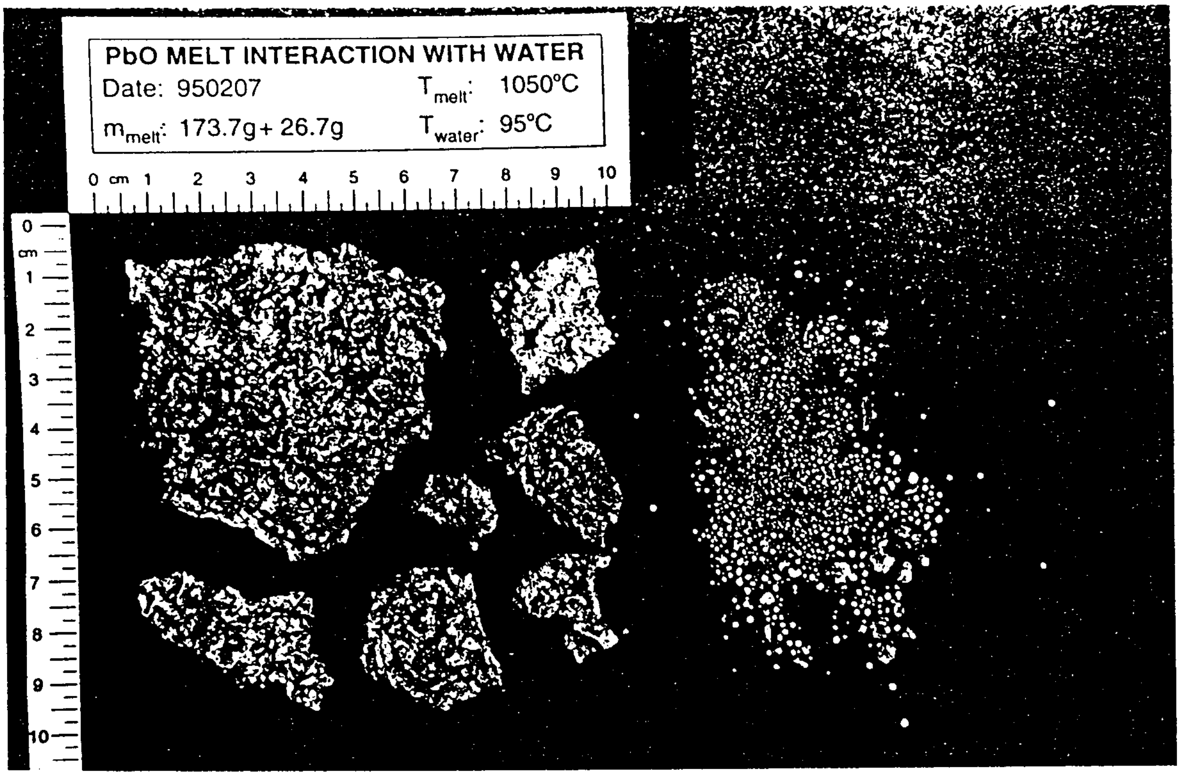

Figure 4. The Melt Fragmentation at Two Different Subcoolings of Water

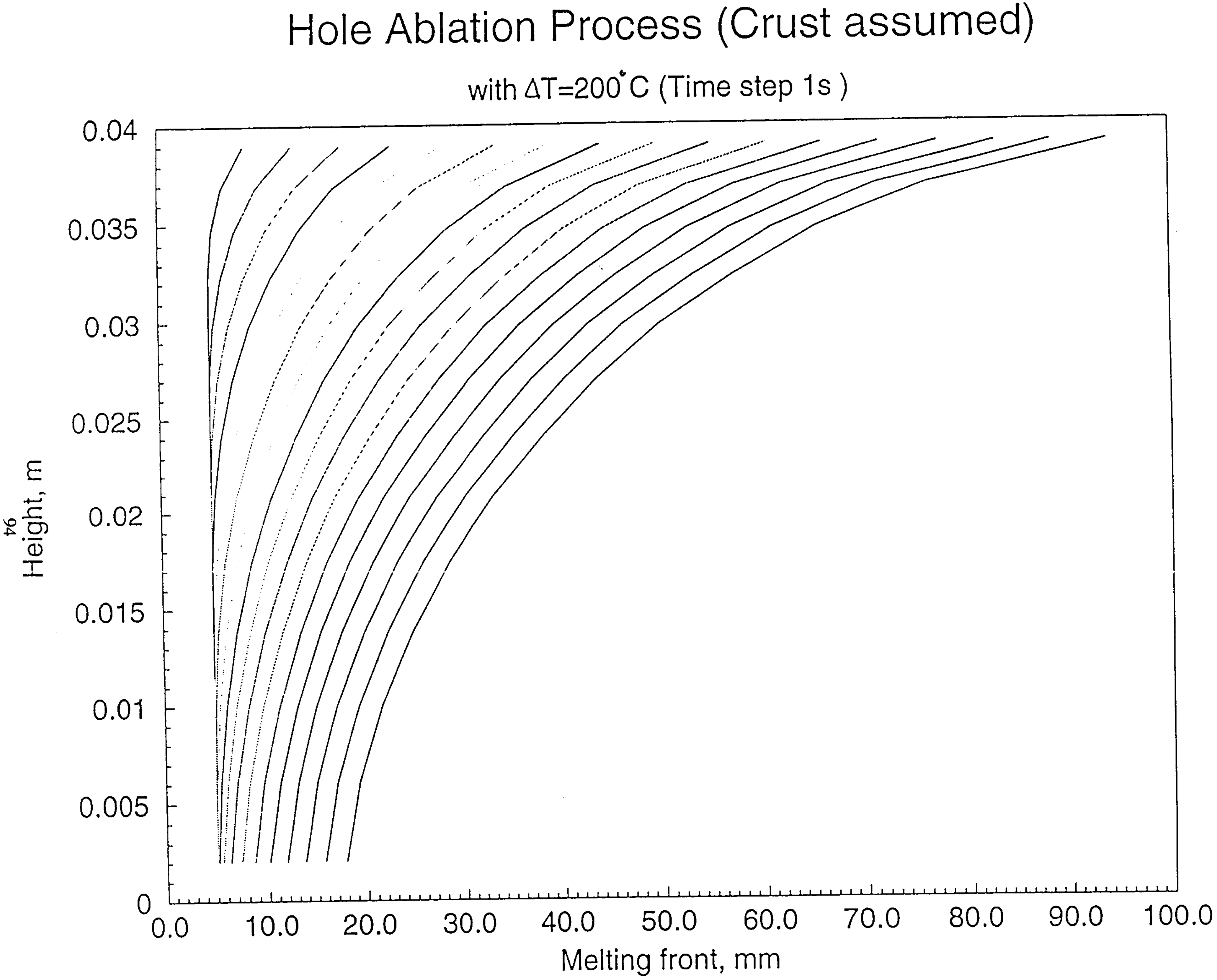
Hole Ablation Process (Crust assumed)
with ΔT=200°C (Time step 1s)
Height, m
0.04
0.035
0.03
0.025
0.02
0.015
0.01
0.005
0
0.0
10.0
20.0
30.0
40.0
50.0
60.0
70.0
80.0
90.0
100.0
Melting front, mm

Figure 5

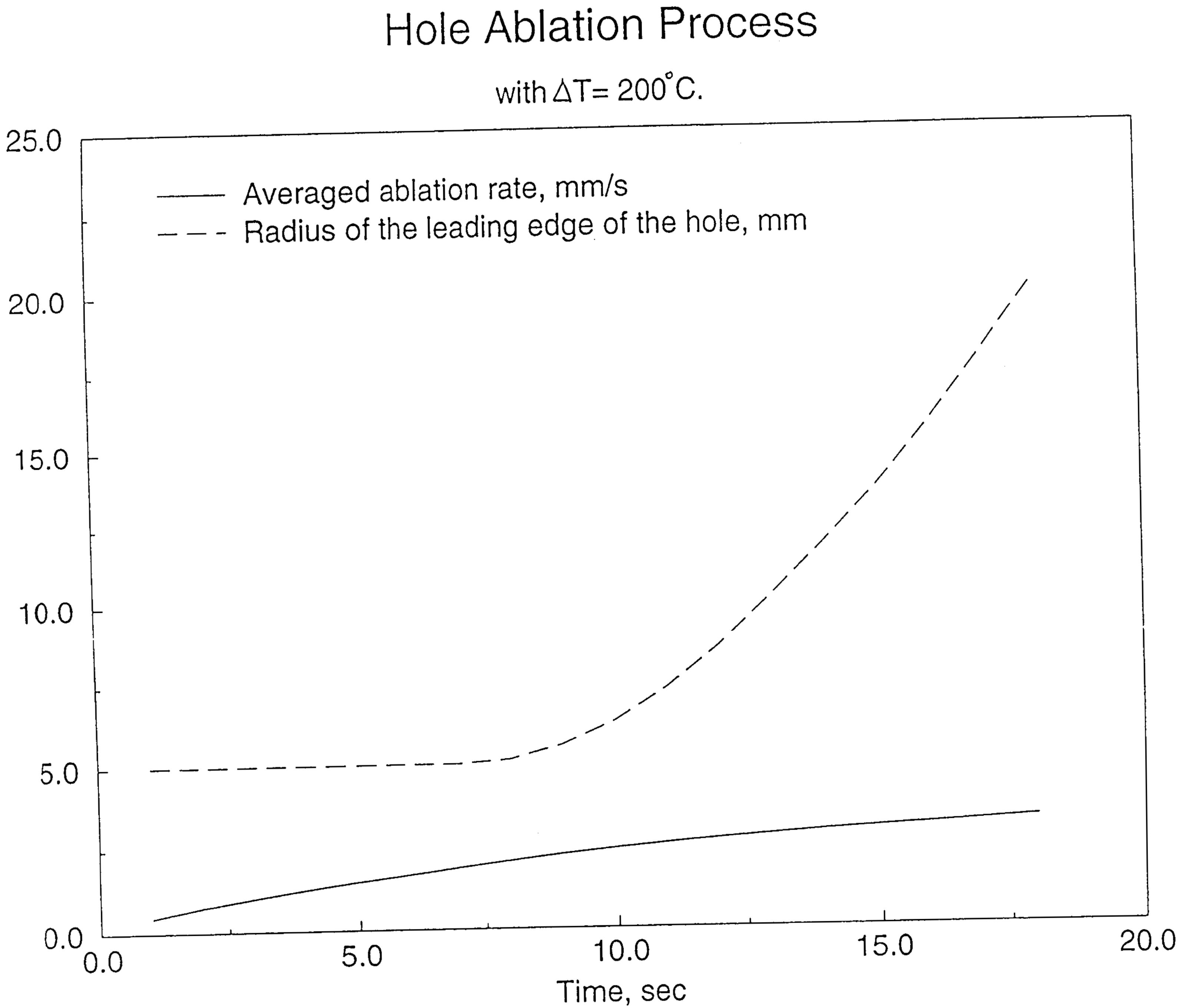
Hole Ablation Process
with ΔT= 200°C.
Averaged ablation rate, mm/s
Radius of the leading edge of the hole, mm
25.0
20.0
15.0
10.0
5.0
0.0
0.0
5.0
10.0
15.0
20.0
Time, sec

Figure 6

Paper No. 7

MODELING OF HEAT AND MASS TRANSFER PROCESSES DURING CORE MELT DISCHARGE FROM A REACTOR PRESSURE VESSEL

T.N. Dinh, V.A. Bui, R.R. Nourgaliev, T. Okkonen and B.R. Sehgal

Royal Institute of Technology, Division of Nuclear Power Safety
Brinellvägen 60, 10044 STOCKHOLM, SWEDEN
Fax:(46) (8) 790-76-78, e-mail: nam@ne.kth.se

Abstract

The objective of the paper is to study heat and mass transfer processes related to core melt discharge from a reactor vessel in a light water reactor severe accident. The phenomenology modeled includes (1) convection in, and heat transfer from, the melt pool in contact with the vessel lower head wall; (2) fluid dynamics and heat transfer of the melt flow in the growing discharge hole; and (3) multi-dimensional heat conduction in the ablating lower head wall. A research program is underway at the Royal Institute of Technology to (i) identify the dominant heat and mass transfer processes determining the characteristics of the lower head ablation process; (ii) develop and validate efficient analytical/computational models for these processes; (iii) apply models to assess the character of the melt discharge process in a reactor-scale situation, and, (iv) determine the sensitivity of the melt discharge to structural differences and to variations in the in-vessel melt progression scenarios. The paper also presents comparison with the recent results of the vessel hole ablation experiments, with a melt simulant.

1 Introduction and Background

In a light water reactor core meltdown accident (severe accident), the molten core material could cause a failure of the lower head of the reactor pressure vessel (RPV), if sufficient internal or external cooling of the vessel could not be provided. Depending on the vessel design and accident sequence in question, the lower head integrity could be lost due to a global or local creep rupture of the lower head wall or - if the lower head had penetrations - a local penetration failure [1]. The initial failure site will enlarge rapidly, due to heat transfer from the ejected melt (corium) which is at a much higher temperature than the vessel melting point. Melt-induced loads on the containment and any further accident progression - involving interactions between core melt and the coolant, structures and atmosphere in the reactor cavity of a pressurized water reactor (PWR) or in the pedestal (lower drywell) or suppression pool of a boiling water reactor (BWR) - would largely depend on the melt ejection characteristics.

Previous work on melt interactions with the vessel wall has been largely analytical [1], except for the experiments conducted at SNL; for a relevant review, see [2]. These experiments, on hole ablation, were performed with iron-alumina thermite and covered a limited hole enlargement range. In fact, the analytical relationships have shown that the past experiments did not cover the range of characteristic numbers typical for either local penetration failures or a circumferential vessel creep rupture [3]. The experimental data obtained have been used by Pilch to develop a one dimensional model [2], equating the energy required to melt the wall material to the energy transferred from the molten fuel passing through the orifice. Comparing to former studies [4],[5], the Pilch's model employed the difference between the temperature of the molten fuel (T_f) and the melting temperature of the wall ($T_{w,mp}$), instead of the difference between the temperature of the molten fuel (T_f) and its melting point ($T_{f,mp}$). However, it is not clear how the assumptions on physical mechanisms and correlations made in different models of the hole ablation process will hold for reactor-scale situations. The lack of experimental evidence supporting or contradicting the applied melt ejection and hole growth models was emphasized also in the recent DCH study for the Zion PWR [3].

Melt ejection and lower head ablation experiments, using an oxidic melt material ($T_f \sim 1000-1500K$) discharged from a vessel with a low-melting-point, metallic lower head ($T_{w,mp} \sim 600-900K$), are underway at the Royal Institute of Technology (KTH), Stockholm. Up till now we have been working with the oxidic melt mixture $PbO - B_2O_3$ (80-20 wt%). It has a melting point of about 900K and its melt-phase viscosity of about 0.1 Pa.s increases with freezing, a characteristic of the core melt as well. In the scoping tests on vessel ablation, pure lead with a melting point of 600K has been used as the lower head wall material. The integral scaling is based on the analysis by Pilch [2]. It was found that we need melt volumes of the order 10-100 liters to reach prototypic characteristics, where the initial lower head failure site flow rate is small compared to the vessel melt contents. In the scoping experiments that we have performed, so far, with melt volumes of about 3-7 liters, the melt has a substantial superheat and the lead plate thickness varied in the range of 2-4 cm [7]. A detailed analytical model is being developed to support experimental design, and to analyse the results obtained. In the present paper, we will describe the physical modeling.

For reactor safety analyses and accident management considerations, the primary interests are the *hole growth dynamics* [$D_{hole}(t)$] and *melt discharge flow parameters* (melt flow rate, superheat, composition). The phenomenological considerations are built around three key elements: the thermal-hydraulic behavior of the core melt in the vessel lower head, the fluid dynamics and heat transfer of the melt flow in the ablating hole, and the thermal and physical (phase-change, mass-transfer) response and feedback of the lower head wall; see Fig.1.

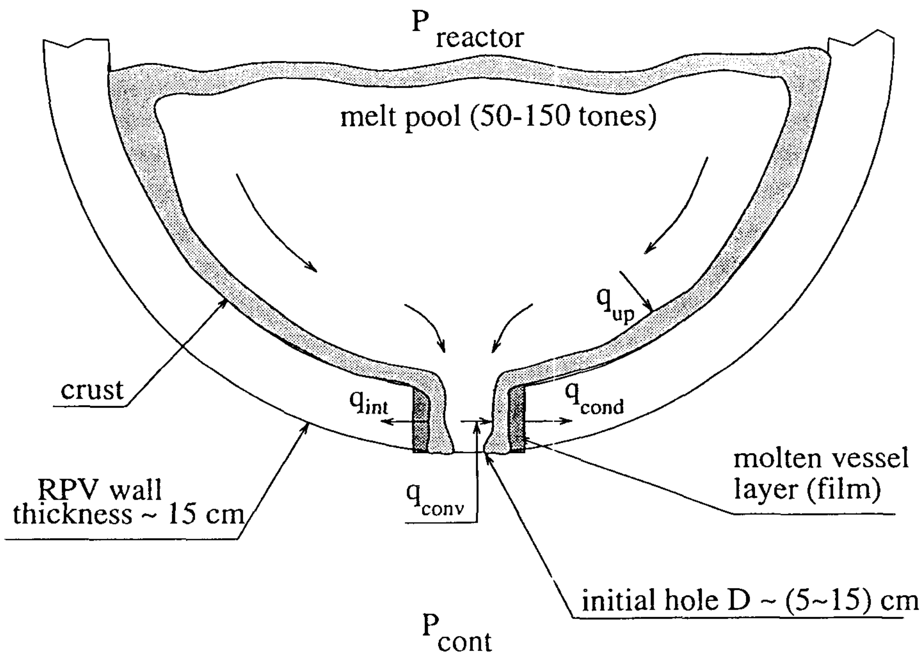

Figure 1: Overall scheme of the hole ablation phenomenology.

During the core melt discharge, the convective heat fluxes (from melt flow to discharge hole boundaries) are the driving mechanisms for vessel ablation. Thus, the heat transfer characteristics of a laminar entry region in experiments, and those of a turbulent entry region in prototypic situations, have to be analysed in an accurate manner. Based on a tentative identification, ranking and evaluation of related physical mechanisms, the most important phenomena are considered to be (1) crust formation and relocation dynamics, (2) temperature dependence of melt properties, and (3) the multi-dimensional heat conduction and ablation front propagation in the vessel wall beneath the crust.

The basic objective of model development is to study the scalability of experimental results and the uncertainties inherent in such extrapolation due to those in the modeling and the data. In order to ensure direct applicability of the data obtained, the prototypicality of the experimental behavior of the melt flow, heat transfer, wall behavior and crust integrity has to be established. Since this is hard to achieve, we must address the scaling distortions in our tests and their relevance to the reactor case. Analytical modeling helps considerably in this task. Separate effects data are employed to validate analytical modeling. The models described below employ - whenever reasonable - only first-principle formulations, or well-supported assumptions on physical mechanisms. Calculated results guide the applicability of available correlations for heat transfer and friction, under prototypical and experimental conditions of interest. Furthermore, new or modified correlations can be introduced in the integrated model HAMISA (Hole Ablation Modeling In Severe Accidents) developed in this work.

2 Modeling of Melt Discharge and Vessel Wall Ablation

The modeling efforts emphasize *integrated thermal hydraulics* of the melt ejection and lower head ablation processes. A model named HAMISA.1D was developed to perform scaling analysis and support the experimental facility design. The model considers two basic cases: (1) hole ablation in and core melt discharge from the RPV in the prototypic case; and (2) experimental cases with some metallic material as the lower head and an oxidic mixture as the corium simulant. The mathematical models of the HAMISA.1D include transient mass and energy conservation in the melt pool, a set of transient, one-dimensional equations of mass, momentum and energy conservation of melt flow in the growing discharge hole, as well as the closure correlations required. These equations form a set of non-linear differential equations integrated within a time loop and along the hole. The fourth-order Runge-Kutta method is applied for numerical solution. The discharge flow rate is determined from the so-called P-SOLUTION algorithm. The vessel wall melting calculations are performed in an axisymmetric geometry while tracking the ablation front. Thus, the model provides the hole ablation rate, $\dot{D}_{hole}(t,z)$, and the melt mass discharge rate, $U_{ejection}(t)$, as function of time, which can then be compared to the data obtained in the experiments. The melt properties, e.g., viscosity and thermal conductivity, are varied as function of temperature. The accuracy of the numerical methods employed has been tested against analytical solutions available for limiting cases. The HAMISA.1D model has been used to describe the Sandia National Laboratories (SNL) tests [6], with reasonable agreement between prediction and data. This comparison was presented elsewhere [7].

In general, the results obtained from the 1-D *dynamic analysis* are similar to the results obtained with simplified models [2]. This fact can be explained by the short time period of the discharge process analysed and the similar approach applied to define the ablation rate. For the SNL tests the large melt superheats and small temperature differences between melting points of the thermite melt and vessel wall metal may have precluded crust formation. Calculations performed for reactor-specific situations demonstrate significant bifurcations of ablation dynamics depending on whether a stable crust layer exists or not. The presence of the crust leads to much lower rates of vessel wall ablation in the initial phase, amplifying thereby the roles of pre-heating and heat conduction in vessel wall and test plates. Due to such spatial and temporal complications, detailed multidimensional and dynamical modeling has been performed to support experimental design and interpretation, as well as the application of the measured data to prototypic reactor accident conditions.

2.1 Melt pool thermal hydraulics

The objectives of the modeling the thermal hydraulics of the melt pool for the hole ablation process are (i) to evaluate the thickness/composition of the crust lying on the lower head prior to the discharge process, and (ii) to model the forced convection heat transfer during the melt discharge process from the RPV. For the purpose of this study, a model was developed and employed to describe the two-dimensional fluid flow and heat transfer [8]. The modified low-Reynolds-number turbulence model was applied to predict the heat transfer characteristics from the melt pool to its frozen boundaries [9]. The heat fluxes obtained were, then, employed to calculate the quasi-static thickness of the crust between the melt pool and the vessel wall [1]. During the melt discharge process, heat flux from melt flow to the crust-vessel wall q_{up} can remelt the crust (solidified melt) layer. Calculations performed show that under both experimental and prototypical conditions, the melt flow during the discharge processes is mostly laminar. This is due to the low vessel overpressurization in our experiments, and the large ratio between the melt pool radius and the discharge hole radius in reactor cases.

2.1.1 Heat transfer results

The laminar flow model was used to analyse geometry and regime effects on heat transfer to the top surface of the vessel wall during the melt discharge process in small-scale experiments and in prototypical situations. Both the oxidic melt simulant and core melt were employed as respective working fluids, with temperature dependent viscosity. For the experimental conditions the Nusselt number on the upper surface of the crust layer above the vessel wall, Nu_{up}, was found to depend on the Reynolds number, Re_{hole}, the ratio between the pool radius and the discharge hole radius $(\frac{r_{pool}}{r_{hole}})$, and the dimensionless distance from the hole inlet, r^*, as follows:

$$Nu_{up} \simeq 1.2 \cdot Re_{hole}^{1/2} \left(\frac{r_{pool}}{r_{hole}}\right) \cdot (r^*)^{-2/3} \tag{1}$$

A limited number of calculations also have been performed for reactor-specific conditions. In general, the Nusselt number, Nu_{up}, obeys eq.(1). The correlation developed (±20% for near-hole regions) can be applied to assess the remelting process of crust overlying the top surface of the vessel wall and the experimental test plate.

2.1.2 Gas blowthrough

We are not aware of extensive computational efforts in predicting gas blowthrough dynamics and believe that it would be very difficult to develop a reliable computational scheme to describe this process. Several correlations have been obtained through the past studies, which have

[1]In this section, the crust refers to solidified melt on the inside of the RPV lower head.

been derived mainly from dimensional analysis and fitting of the experimental data; see e.g. [10]. Gluck et al. proposed a correlation for gas blowthrough onset in flat and hemispherical bottomed cylinders [11],[12],

$$\frac{H_{pool,gb}}{D_{hole}} = 0.43\frac{D_{pool}}{D_{hole}}tanh\left(Fr^{1/2}\frac{D_{hole}}{D_{pool}}\right) \tag{2}$$

Recently, Pilch and Griffith [13] have collected and examined a number of correlations describing gas blowthrough with respect to their applicability to core melt discharge from RPV. They found that only the Gluck correlation embodies the effects of tank diameter, and the data base of this correlation spans the range of the Froude number $Fr = \frac{U_{ejection}}{\sqrt{g \cdot D_{hole}}}$ and the D_{pool}/D_{hole} values needed for reactor applications. Therefore, the Gluck correlation was recommended for use in DCH analyses. However, it was found that there were no significant effects of the ratio $\frac{D_{pool}}{D_{hole}}$ for the RPV hole ablation and melt discharge conditions (i.e. D_{pool} ~3.6m and D_{hole} in the range 0.05-0.5m).

In the present study, we are interested in the onset of gas blowthrough, rather than the annular gas-liquid discharge flow dynamics. For this purpose, a quasi-steady 2-D formulation is used to calculate flow and pressure fields in the experimental crucible and RPV lower plenum with melt discharge through holes of different sizes. It can be shown that the boundary layer thickness in the hemispherical pool is so small that the whole flow field could be treated as potential flow. Nevertheless, the grid independence of numerical solutions has been examined, based on the results obtained with computational meshes of different refinements. Calculations employing a low-Reynolds-number turbulence model indicate that the shear-induced turbulence generation takes place only near the hole inlet and does not affect the pressure field in the large. The laminar model is thus, applied to calculate flow and pressure fields.

Fig.2 describes the calculated velocity field in a hemispherical lower head during the core melt discharge process. The calculated results of dynamic pressure field were analysed to evaluate the potential "crater formation" in the melt pool. First, dynamic pressure distributions at various heights from the lower plenum bottom are compared to hydraulic heads of the respective melt columns; see Fig.3. Our hypothesis is that at the critical pool depth the dynamic pressure variation above the discharge hole is equal to the corresponding hydraulic head, thereby inducing enough deformation of the free surface that gas entrains in the discharge flow. Fig.4 depicts the technique used to determine the blowthrough onset. Comparison of numerically determined critical pool depth with the experimental correlation of Gluck et al. for the hemispherical bottom cylinders is given in Fig.5. It is seen that good agreement is achieved for the parameter ranges of interest.

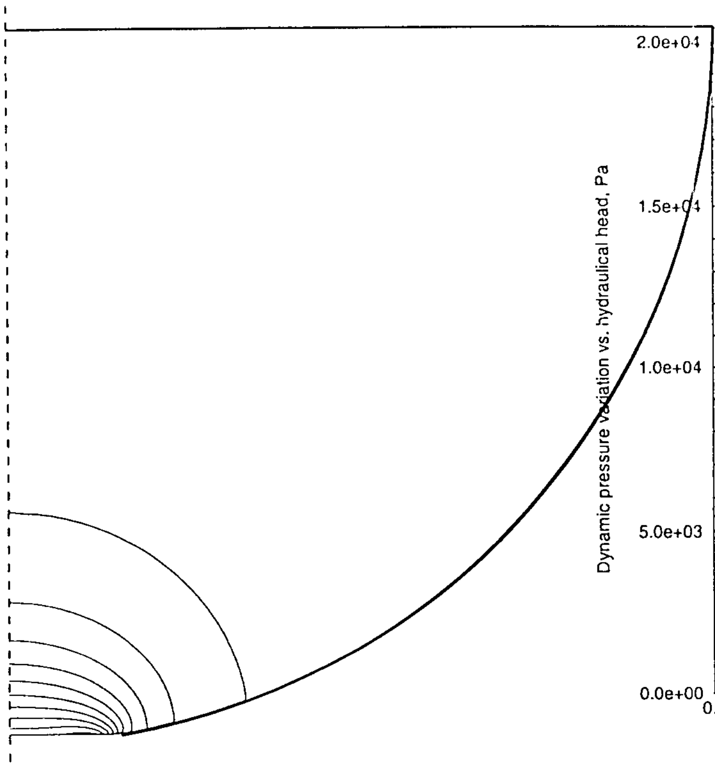

Figure 2: The velocity field during the core melt discharge process: $U_{ejection} = 10\text{m/s}$, $D_{hole} = 0.5\text{m}$, $D_{RPV} = 3.6\text{m}$. The computational mesh for the lower plenum section 50x50.

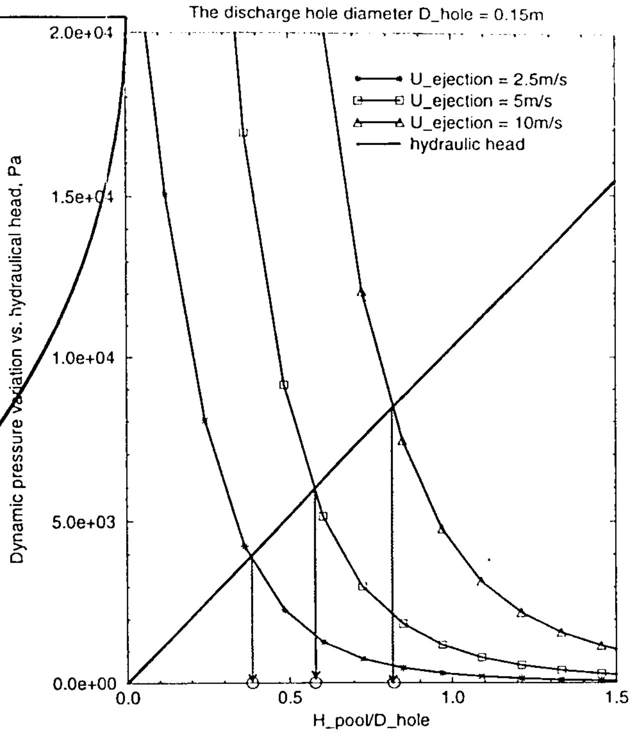

Figure 4: Determination of gas blowthrough onset from the dynamic pressure and hydraulical head of the liquid column above the hole (○ corresponds the critical pool depths).

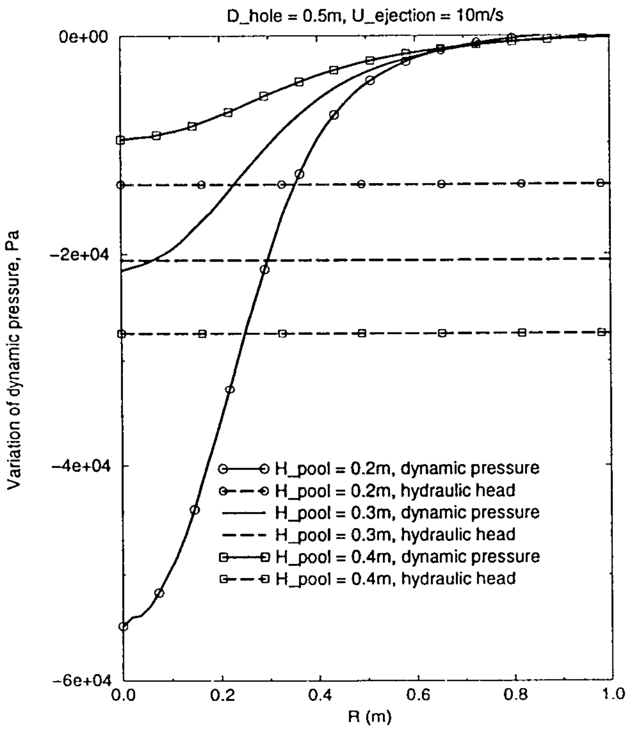

Figure 3: Calculated radial distributions of the dynamic pressure in core melt pool.

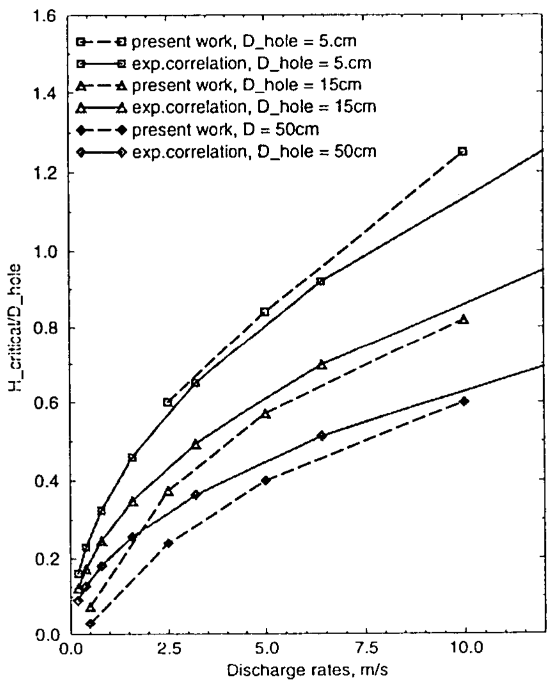

Figure 5: Comparison with the experimental correlation of Gluck et al.

It is worth noting here that the present work assumes (at least partial) depressurization of the reactor coolant system prior to the melt discharge, i.e. the discharge flow rates are in the intermediate range of 3-10m/s. The moment when a melt pool crater starts to dominate the flow patterns, in reactor cases, can be evaluated in the integrated HAMISA model using the Gluck correlation. In addition, the relative critical pool depth ($k_{crater} = \frac{H_{pool,gb}}{D_{hole}}$) decreases with increasing discharge hole diameter. It is found that annular-type discharge flow regimes can occur only at the very end of the ablation and discharge process. For an initial melt mass of 100 tonnes, fractions of melt mass discharged in annular-type regime have been evaluated to be in the ranges 2-5% and 4-10% for the cases with and without crust, respectively [2].

2.2 Discharge hole thermal hydraulics

In this section, we present some results on the core melt ejection process through a circular hole in the RPV lower head. A control-volume based model was previously developed to solve the Navier-Stokes and energy equations in 2-D axisymmetric, narrowing channels with a constant wall-temperature boundary condition [8], while accounting for axial diffusion of both momentum and heat as well as viscous dissipation. Additionally, a low-Reynolds-number model of turbulence was employed, due to the presence of laminar, transition-to-turbulence and turbulent regimes in the reactor-scale applications.

By employing the first-principle-modeling approach, it is possible to examine the effects of following set of specific variations of viscosity and conductivity across the boundary layer due to freezing of the core melt near the wall, of velocity/temperature profiles at the hole inlet, of (narrowing) channel geometry, and of fluid Prandtl number. For limiting cases of interest, the calculated results compare satisfactorily with previous boundary layer solutions, and the measured data found in the literature.

2.2.1 Experimental conditions

Since Reynolds numbers in the experiments are sufficiently low, laminar flow is the most probable experimental regime. That is why detailed analysis of thermal hydraulics within the discharge hole under experimental conditions must be carried out in order to address the relevance of experiments to the prototypical reactor conditions.

Pressure drop.

The apparent Fanning friction factor corresponds to pressure drop in a certain flow length through the duct. In a tube with a frictionless infinite upstream section ($-\infty < z < 0$), the apparent Fanning friction factor is defined as follows:

$$f_{app}(z_*) = \frac{P(-\infty) - P(z_*)}{2Re_{hole}z_*} \tag{3}$$

The results presented in Table 1 assume that the viscosity varies strongly in the sublayer ($0.95 < \frac{r}{r_{hole}} < 1$). The maximum value of the viscosity at the wall is 25 times greater than the bulk viscosity. It can be seen that in the vicinity of the hole entrance, the viscosity variation

[2] Note that crust affects the hole growth and the hole size.

leads to more than two times higher values of the apparent Fanning friction factor. Note that the thickness of the metallic plate, and thereby the hole length Δz, in the experiments corresponds to z_* in the range of $10^{-4} - 10^{-3}$. It is seen that friction factors are sensitive to the viscosity variations in that region.

Table 1: The apparent Fanning friction factor.

$z_* = \Delta z/(D_{hole} \cdot Re_{hole})$	Apparent friction factor μ_{fs} = var	Apparent friction factor μ_{fs} = const
$3.138 \cdot 10^{-4}$	464.3	222.8
$1.256 \cdot 10^{-3}$	170.9	102.9
$7.034 \cdot 10^{-3}$	60.9	44.7
$9.166 \cdot 10^{-1}$	19.4	16.3

The Nusselt number.

Table 2 presents results of heat transfer calculations for four cases. The first case is the standard case without property variation. The second case shows effects of the above-described variation of viscosity across the sublayer on the heat transfer. The third and fourth cases include variations of both viscosity and conductivity across the sublayer. The conductivity is decreased parabolically near the wall. Values of the fluid conductivity in the wall-fluid interface are two and ten times smaller than that of the bulk conductivity, for the third and fourth cases, respectively. Values of the Reynolds number are constant for four cases, and equal to 500. In fact, the effects of property variations on heat transfer are even greater than those shown in Table 2, due to the fact that the discharge mass flow rates are also reduced due to increased wall friction (see Table 1 for the apparent Fanning friction factor). Similar calculations have also been performed for the reactor cases by employing the low-Reynolds-number turbulence model. Most notably, there is also the development of a laminar boundary-layer flow in the very short section of the discharge hole ($z_+ \sim 10^{-6}$). However, there are two different factors determining the effects of temperature dependence of fluid properties on heat transfer rates. First, the lower are the values of z_+, the more significant are the effects of fluid properties, due to the smaller thickness of the boundary layer with property variations. Second, the Reynolds numbers are higher under prototypical conditions, which limit the properties variations along and across the flow sections.

In the present range of applications, one can conclude that the temperature dependence of transport properties needs to be accounted for in evaluation of the pressure drop and the heat transfer coefficients inside the discharge hole. However, it is not known how the properties vary in the temperature range near the corium melt solidus point. We believe, experimental data, employing melt simulants with temperature-dependent viscosity, are required at relatively high Reynolds numbers to reduce uncertainties in the assessments of convective heat fluxes and in the formulation of boundary conditions for the prototypic melt flow with a wide mushy region [$\Delta T_{mushy} = (T_{liquidus} - T_{solidus}) \sim$ (150-200)K].

Analyses performed for converging ducts show dual effects of such geometry: narrowing channels cause a flow laminarization but can also subject channel walls to the hotter melt entering from the pool into the hole-wall boundary layer. Such aspects require further model development e.g., coupling melt thermal hydraulics in the hole and the pool. Another analysis development issue is whether the core melt and its oxidic simulant behave as with Newtonian fluids, especially for cases with small melt superheats above the melt solidus point.

Table 2: The Nusselt number in laminar flows.

$z_+ = \Delta z/(D_{hole} \cdot Pe_{hole})$	Nusselt numbers			
	μ, k = const	μ = var	μ, k = var; $\frac{k_w}{k_b}$=0.5	μ, k = var; $\frac{k_w}{k_b}$=0.1
$3.138 \cdot 10^{-4}$	22.21	15.81	14.47	11.70
$1.256 \cdot 10^{-3}$	11.56	9.82	9.34	8.19
$7.034 \cdot 10^{-3}$	5.82	5.39	5.26	4.92
$9.166 \cdot 10^{-1}$	3.65	3.44	3.37	3.21

Discharge coefficient.

In most scaling studies and previous models, velocities of melt ejected from the vessel are calculated by means of Bernoulli's equation [eq.(4)] with discharge coefficient C_D, in the range of (0.6-1).

$$U_{ejection} = C_D\sqrt{\frac{2\Delta P_{hole}}{\rho_f}} \tag{4}$$

where $\Delta P_{hole} = \rho_f g H_{pool} + P_{reactor} - P_{containment}$. The results obtained for melt ejected through holes (in a 2-D axisymmetric steady-state formulation) show the general applicability of eq.(4) for conditions of interest. Specifically, eq.(4) applies to the prototypical situations, due to the low viscosity of core melt, $\mu_f \sim 0.005$ Pa.s, and the relatively small thickness of the vessel wall, L_{wall}, compared to discharge hole diameters, D_{hole} ($L_{wall}/D_{hole} < 1$ soon after the melt flow starts through the discharge hole. However, in our experiments, oxidic melt simulant has a higher viscosity ($\mu_{fs} \sim 0.1$ Pa.s), and the vessel overpressure is smaller. For this case, the fluid-wall friction along the hole, ξ_{f-w}, must be taken into account. In order to facilitate the development of the fast-running HAMISA model, the pressure drops in an orifice [eq.(5)] is calculated with the use of a loss coefficient ($K_{loss} = 1/\sqrt{C_D}$), whereas the discharge flow velocity is determined from the solution of momentum equation along the hole [eq.(6)].

$$\Delta P_{orifice} = \frac{K_{loss}\rho_f U_{f,ave}^2}{2} \tag{5}$$

$$\begin{aligned}\frac{dP_f}{dz} = -\rho_f U_f \frac{dU_f}{dz} - \rho_f \frac{dU_f}{dt} - \rho_f g - \frac{\xi_{f-w}(z)\rho_f U_f(z) \mid U_f \mid}{2D_{hole}} - \frac{2 \cdot P_f}{D_{hole}}\frac{dD_{hole}}{dz} \\ -U_f\rho_f\left[\frac{dU_f}{dz} + \frac{2U_f}{D_{hole}}\frac{dD_{hole}}{dz}\right] - \frac{2\rho_f U_f}{D_{hole}}\frac{dD_{hole}}{dt}\end{aligned} \tag{6}$$

with $\Delta P_{f-w,hole} = \Delta P_{hole} - \Delta P_{orifice}$ as the given pressure drop in the hole. These equations together with mass conservation equation comprise a method to calculate melt ejection rates from a vessel that is more general than the conventional Bernoulli's equation. As already mentioned, the method is crucial when analysing oxidic simulant flow through a hole in the experimental test plates.

Calculations performed for reactor-scale melt discharge processes show an increase in hole pressure drop due to the temperature dependence of melt viscosity. However, as shown above (see section 2.2.1), the fluid-wall friction inside the hole has a minor effect on the ejection rates.

2.2.2 Prototypical conditions

In typical accident scenarios, the core melt flows in the discharge hole at high Reynolds numbers (Re in the range 10^5 - $5 \cdot 10^6$), depending, primarily, on the reactor system overpressurization and the size of local failure site (hole diameter). The flow within the discharge hole may be characterized by development of laminar boundary layer at the very entry region and its transition to turbulent. Nusselt numbers in the laminar flow region and turbulent region may be determined by Schlichting's correlation [eq.(7)] and von Kármán's correlation [eq.(8)], respectively [15].

$$Nu = 0.332 \cdot z_+^{-1/2} \cdot Pr^{-1/6} \tag{7}$$

$$Nu = \frac{0.0288 \cdot Re^{3/5} \cdot z_+^{-1/5} \cdot Pr^{4/5}}{1 + 0.85 \cdot Re^{-1/5} \cdot z_+^{-1/10} \cdot Pr^{-1/10}\left\{Pr - 1 + ln[1 + \frac{5}{6}(Pr - 1)]\right\}} \tag{8}$$

The Eqs.(7-8) were obtained, originally, for boundary layers over the flat plate, they are used here with Nu numbers based on the channel diameter. These correlations are compared to the results of this study employing numerical solutions for the fluid flow and heat transfer within the hole in Figs.6-8. One can see that the method of two-dimensional turbulent flow modeling employed in the present work is able to reproduce heat transfer laws related to boundary-layer development. Correlations of Dittus-Boelter and Petukhov et al. [16] for heat transfer in developed flows are also given for comparison.

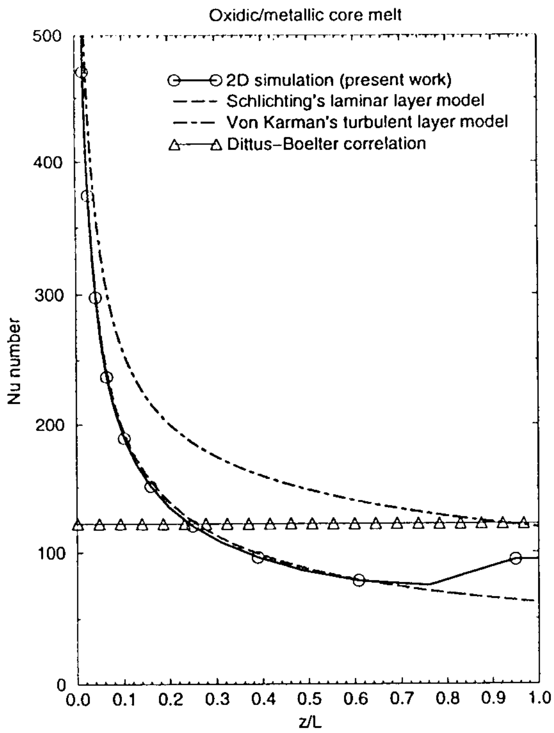

Figure 6: Forced convection heat transfer within the discharge hole: $Re_{hole} = 10^5$, $Pr = 0.2$, L is the hole length.

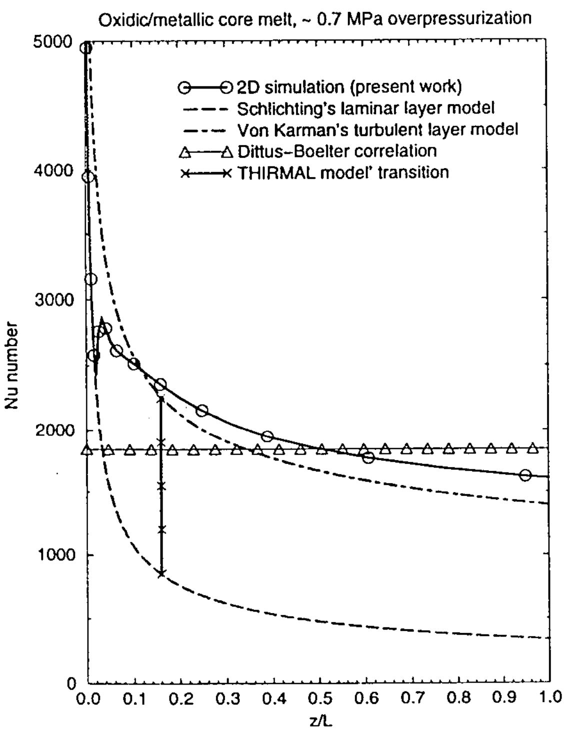

Figure 7: Forced convection heat transfer within the discharge hole: $Re_{hole} = 3 \cdot 10^6$, $Pr = 0.2$, L is the hole length.

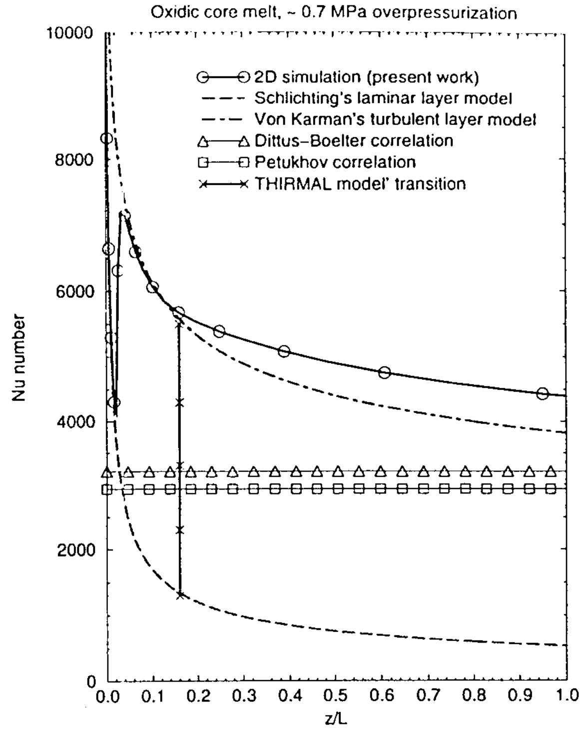

Figure 8: Forced convection heat transfer within the discharge hole: $Re_{hole} = 3 \cdot 10^6$, $Pr = 0.82$, L is the hole length.

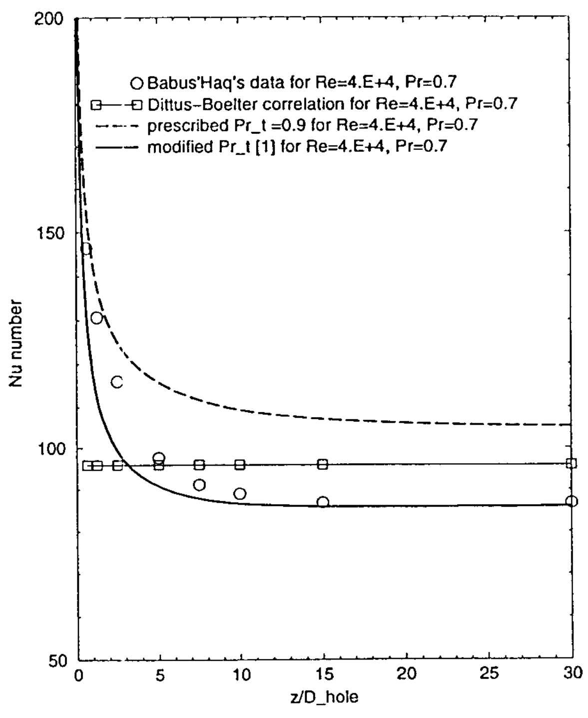

Figure 9: Local Nusselt number in the thermal entrance region: $Re_{hole} = 4 \cdot 10^4$, $Pr = 0.7$.

Despite of the quantitative agreement achieved between computational results and experimental correlations, it is worth noting that there exist significant difficulties in turbulence modeling of the thermally and hydrodynamically developing flows. An attempt has been made towards accounting for anisotropic effects in the thermally developing and developed flows [14]. However, the absence of experimental data for $z_+ < 10^{-5}$ still renders uncertainties of predicting heat transfer in the very entry region of high-Reynolds-number flows (Re numbers up to 10^7 and z_+ in the range $10^{-7} - 10^{-5}$). Thus, further work on validation and application of the model developed must focus on effects of Re and fluid Pr numbers, as well as possible effects of temperature dependence of physical properties in the thermal boundary layer.

Eqs.(7-8) have also been used in the THIRMAL code [17]. However, the criterion for laminar-to-turbulence transition was taken as $Re_{z,trans} = \rho_f U_{ejection} Z_{trans}/\mu_f = 5 \cdot 10^5$. This selection of $Re_{z,trans}$ is, perhaps, based on previous measurements on small diameter channels or flat plates. Reference [17] reports that the minimum heat transfer coefficient will be either at the channel exit or at the location where the laminar-to-turbulent transition occurs. As shown in Figs.7-8 the THIRMAL model produces very sharp variation of the Nusselt numbers. We believe that this choice of $Re_{z,trans}$ provides relatively smaller final hole sizes determined by the local erosion rate.

Our two-dimensional model for heat transfer in the developing turbulent flow, however, indicates that the transition might occur at much smaller $Re_{z,trans}$. Results obtained for Reynolds number ranging from 10^4 up to $7.5 \cdot 10^6$ indicate $Re_z = 10^5$ as the most probable value of $Re_{z,trans}$ for the large-diameter (more than 5cm ID) circular channels. It was found that the fluid Prandtl number has a minor effect on $Re_{z,trans}$, while ranging from $Pr = 0.2$ to $Pr = 1$. In the prototypic range of Re numbers ($Re \sim 10^6$), the laminar-to-turbulent transition would take place near the hole entry. Furthermore, one has to account for turbulence in melt flow coming to the hole inlet. In such a case, the boundary layer may become turbulent from the inlet leading edge of the discharge hole. This may be seen in Fig.9, which depicts a monotonic decrease of Nusselt numbers for hydrodynamically developed flows (in the thermal entrance region) at low Re numbers ($Re = 4 \cdot 10^4$). This is related to the fact that upstream turbulence is able to cause reductions in $Re_{z,trans}$. Presuming forced convection heat transfer as the governing mechanism, the present analysis indicates that the axial profile of heat transfer coefficient, and, therefore, also of the wall ablation rate, will decrease monotonically towards the hole exit.

2.3 Crust behavior within the discharge hole

In the hole ablation process, the crust formation and dynamics play a very important role. The unsteady growth and decay of a frozen layer (crust) in a liquid flowing past a non-melting wall was studied by Epstein [18], who developed an integral method, employing second-order polynomials for temperature profile. This method was, later, applied to calculate the process characteristics in a tube flow, with solidification in the liquid flow, and melting in the initially solid wall [19]. So far, no direct observations or measured data on the dynamic behavior of the crust and molten wall layer within the discharge hole have been reported from simulant (say, Freon-ice wall system) or prototypic melt material experiments.

The crust formation and existence determine the rate of vessel wall ablation. If there is a stable crust, the melt superheat (say, 10-200K in reactor cases) forms the heat-driving temperature difference ($\Delta T_{ref} = T_f - T_{f,mp}$), while without crust the wall ablation would be much more rapid, since the driving temperature difference is that between the melt temperature and the wall melting point (i.e, $\Delta T_{ref} = T_f - T_{w,mp} = 2700\text{-}1700 \sim 1000\mathrm{K}$). If the factor in melt-wall heat transfer was about ten, as it could be between the limiting cases, the relative growth of an initially small hole ($\propto \Delta T_{ref}^{1/3}$ [2]) could differ by a factor of two or more.

In order to assess the dynamics of the crust formation, growth and existence during the melt discharge process in both prototypic and experimental conditions, we have considered a set of phenomena, including conduction-controlled crust growth, crust remelting due to the convective heat flux from melt flow, q_{conv}, convection-induced crust sweep-out by melt flow and the falling film of molten vessel wall beneath the crust. It was found that, although, the remelting time periods, $\tau_{cr,remelt}$, are rather short for the characteristic values of crust thickness, the remelting times are as much as 3-5 times larger than the characteristic times of the conduction-controlled crust growth, $\tau_{cr,growth}$, for the given values of crust thickness, $\delta_{f,crust}$; see Table 3. At the hole outlet, the heat transfer rates are relatively small, especially in the initial phase of the discharge process. Hence, the crust growth and existence are dominant. Further, the limiting mechanisms of convection-induced crust dynamics were considered to evaluate typical values of the crust thickness. Order-of-magnitude assessments for crust-related parameters in reactor situations and in the KTH experiments are given in Table 4. It can be seen that the values of the crust thickness are about 0.5 mm for both prototypic and experiment conditions. Such crust thicknesses are applied to the outlet of the discharge hole. The time characteristics related to the hole ablation process (ablation time, convection-controlled crust life time) for the prototypic and the experiment conditions are similar to each other. *******************

Table 3: Crust formation and remelting.

PARAMETERS	REACTOR				EXPERIMENTS (KTH)		
$\rho_{f,crust}$, kg/m^3	8000				6000		
H_{fusion}, J/kg	$3 \cdot 10^5$				$2.5 \cdot 10^5$		
q_{conv}, MW/m^2	1	5	10	20	3	6	9
$\frac{\partial \delta_{f,crust}}{\partial t}$, mm/s	0.4	2	4	8	2.4	4.8	7.2
$\delta_{f,crust}$, mm	1	0.2	0.1	0.05	0.5	0.25	0.1
$\tau_{cr,remelt}$, s	2.5	0.1	0.025	0.006	0.2	0.06	0.015
$\tau_{cr,growth}$, s	0.5	0.04	0.01	0.0025	0.06	0.015	0.005

A number of models were developed to describe the crust formation and wall melting processes. Originally, a separate-layer model was proposed to model the thicknesses of the crust, $\delta_{f,crust}$, and of the molten wall layer, $\delta_{w,ml}$. Previous studies (e.g. [19]) have employed a three-layer model with heat conduction and heat balance across the layers of crust, molten wall and solid wall to represent their transient behavior. We believe that heat conduction is not the only operative mechanism, as has been assumed in most previous studies (including [19]) for the dynamics of the crust and vessel wall molten layer. There are other mechanisms active e.g. the shear force from melt flow through the crust layer and the falling film of the molten vessel wall. Therefore, a simplified approach to the treatment of the crust within the discharge hole has been taken, by assuming that heat conduction is the dominant process in the initial ablation phase when the thickness of the molten wall layer is less than a critical value ($\delta_{w,ml} < \delta^*_{w,ml}$), say $\delta^*_{w,ml} = 1$mm for experimental conditions. There the two equations of heat conduction and phase change in crust and molten wall layers are applied

$$\rho_{f,crust} H_{fusion,crust} \frac{d\delta_{f,crust}}{dt} = -\kappa_{f,crust} \frac{T_i - T_{f,mp}}{\delta_{f,crust}} - q_{conv} \qquad (9)$$

Table 4: Dynamics of the crust within the discharge hole.

PARAMETERS	REACTOR		EXPERIMENTS (KTH)	
Film-driven crust dynamics				
Typical ablation rate, V_{ab}, mm/s	3-10 (ave: 6)		1-6 (ave: 3)	
Vessel/plate thickness, L_{wall}, m	0.15		0.02-0.05	
$\delta_{w,ml}$, mm	1	0.5	1	0.5
$U_{film} = V_{ab}L_{wall}/\delta_{w,ml}$, m/s	0.9	1.8	0.06 - 0.15	0.12 - 0.3
$\tau_{film,conv} = L_{wall}/U_{film}$, s	0.16	0.08	0.25	0.10
Melt flow-driven crust dynamics				
$U_{ejection}$, m/s	3 - 10		0.3 - 1	
Re_{hole}	(0.7-2.3)$\cdot 10^6$		900-3000	
ξ_{f-cr}	$0.3164 \cdot Re_{hole}^{-1/4}$		$16/Re_{hole}$	
$U_{fbl} = U_{ejection}\sqrt{\frac{\xi}{8}}$, m/s	0.1 - 0.3		0.02 - 0.1	
$\tau_{fbl,conv} = L_{wall}/U_{fbl}$, s	1.5 - 0.5		1.5 - 0.2	
$\tau_{cr,res} = min(\tau_{film,conv}, \tau_{fbl,conv})$, s	0.1		0.15	
$\delta_{f,crust}$, mm (for $\tau_{cr,growth} = \tau_{cr,res}$)	0.5		0.6	

$$\rho_w H_{fusion,w} \frac{d\delta_{w,ml}}{dt} = -\kappa_w \frac{T_i - T_{w,mp}}{\delta_{w,ml}} - q_{cond} \tag{10}$$

where

$$T_i = \frac{\frac{\kappa_{f,crust} T_{f,mp}}{\delta_{f,crust}} + \frac{\kappa_w T_{w,mp}}{\delta_{w,ml}}}{\frac{\kappa_{f,crust}}{\delta_{f,crust}} + \frac{\kappa_w}{\delta_{w,ml}}}$$

Should the thickness of molten wall layer reach its critical value, $\delta^*_{w,ml}$, the thickness of the crust layer is calculated from eq.(11), and the heat flux imposed on the phase-change interface, q_{int}, is defined byeq.(12).

$$\rho_{f,crust} H_{fusion,crust} \frac{d\delta_{f,crust}}{dt} = -q_{conv} + \frac{T_{f,mp} - T_{w,mp}}{\frac{\kappa_{f,crust}}{\delta_{f,crust}} + \frac{\kappa_w}{\delta^*_{w,ml}}} \tag{11}$$

$$q_{int} = -\kappa_w \frac{T_{w,mp} - T_i}{\delta^*_{w,ml}} \tag{12}$$

In the present study, the calculated values of q_{int} are employed as the boundary condition for the vessel wall heat conduction and ablation analysis below; see, e.g., eq.(13). These crust-related assumptions need to be verified, when more experimental observations and data become available.

2.4 Vessel wall heat conduction and ablation

In this section we will examine effects of preheating and multi-dimensional heat conduction in the vessel wall and test plate. Preliminary assessments for experiments employing lead (as well as aluminum and tin) as simulants for the vessel wall show significant transients in the test plate's temperature field prior and during melt discharge. As it takes time (15-30s) for melt discharge process to start after the first melt-wall contact, the thermal front could already penetrate through the relatively thin metallic layers (2-4cm) of the test plate due to large values of thermal diffusivity ($\alpha = 20 - 40 \cdot 10^{-6} \mathrm{m}^2/\mathrm{s}$) of vessel materials (metals) used. The HAMISA.2D/WALL model has been developed to describe *two-dimensional heat conduction with phase change.* An efficient numerical technique has been developed to solve two-dimensional heat conduction equation with moving phase-change boundary. The idea of the numerical method developed is to have a dominant direction of boundary movement, that is the ablation front along the hole. The heat conduction in the other direction is taken into account in a semi-implicit manner. The moving rate of phase-change boundary of a given strip (horizontal layer) in cylindrical coordinate system (r, z) is defined through the difference between the heat flux imposed on the interface, q_{int}, and that taken away by heat conduction, q_{cond}, as follows (see also Fig.1)

$$V_{ab}(z,t) = \frac{\sqrt{r_o^2 + \frac{2(q_{int} - q_{cond}) r_o \Delta t}{\rho_w H_{fusion,w}}} - r_o}{\Delta t} \tag{13}$$

where r_o is the position of the melting front at time t_o, and Δt is time step, $\Delta t = t - t_o$. Calculated values of V_{ab} are then used to track the phase-change interface.

3 Analysis of the KTH Hole Ablation Experiments

A set of scoping experiments on hole ablation were performed at KTH in 1994 [7] in which a melt of $PbO + B_2O_3$ oxidic mixture at $\simeq$ 1100K was ejected through an initial hole of 10 mm dia. drilled in three lead plates of 20, 30 and 40 mm. The melt volume employed in each case was $\simeq$ 5 liters (approximately 35 kg). The final sizes and shapes of the ablated holes are shown in Fig.14, which depict the two-dimensional character of the hole ablation process. It was also observed during the hole ablation process that the rate of hole ablation at the hole exit increased markedly after an initial period during which, perhaps, a certain portion of the plate in the vicinity of the ablating hole heated up to near the melting temperature.

Analysis of these scoping experiments was performed using the HAMISA.2D/WALL model. Results of the for cases with and without crust are presented, respectively, in Figs.10-11 and Figs.12-13.

It can be seen from Figs.11,13 that roughly similar diameters for the final hole were predicted for two cases. Nevertheless, transient temperature fields in the test plate during melt discharge process are *sensitive* to the boundary conditions, i.e. crust presence (18s process; see Fig.10) or absence (7s process; see Fig.12). Therefore, data of thermocouples installed inside the test plate and the reduced data for ablation dynamics could be used to assess heat fluxes from melt flow to the test plate. Consequently, existence of the crust could be evaluated. Large openings of the hole at its inlet can be ascribed to entrance effects on heat transfer and the pre-heating of the test plate prior to melt front propagation. Qualitatively, the calculated results of final hole size (Figs.10) and ablation dynamics (Figs.11) agree with observations from the KTH scoping experiments on vessel hole ablation (Fig.14). The observation that the hole growth rate has accelerated towards the end of the process supports the assumption of crust existence, at least, at the hole exit (compare cases 1 and 2 in Figs.11,13. However, in order to observe, more decisively, crust existence from measurement data in future experiments, we have to provide small ratios for $\frac{T_{fs}-T_{fs,mp}}{T_{fs}-T_{w,mp}}$, i.e. the melt superheat has to be much less than the difference between the melt temperature and the wall melting point. Under such conditions, the identification of the influence of the crust could be readily delineated. Analyses performed with the help of the HAMISA.2D/WALL model help us to design the experiments, e.g., define the initial thermal state of the test plate, set requirements for melt pouring times, and design the test plates.

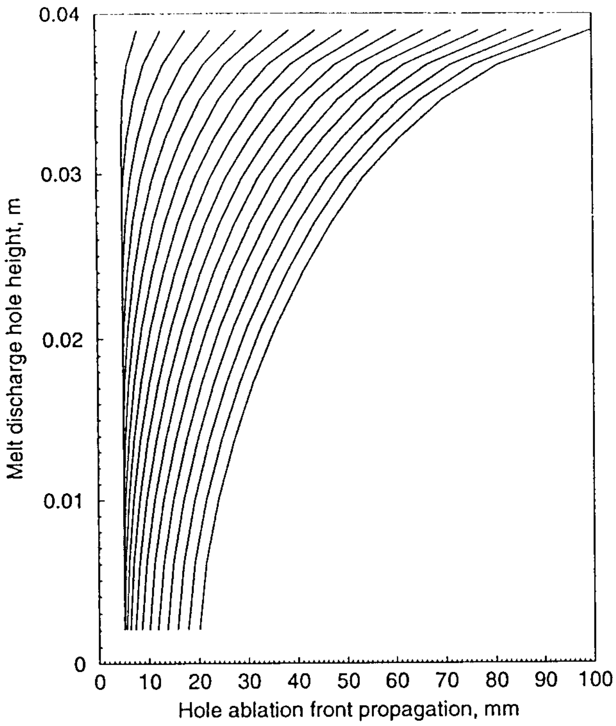

Figure 10: Case 1: $T_f - T_{f,mp} = 200\text{K}$.

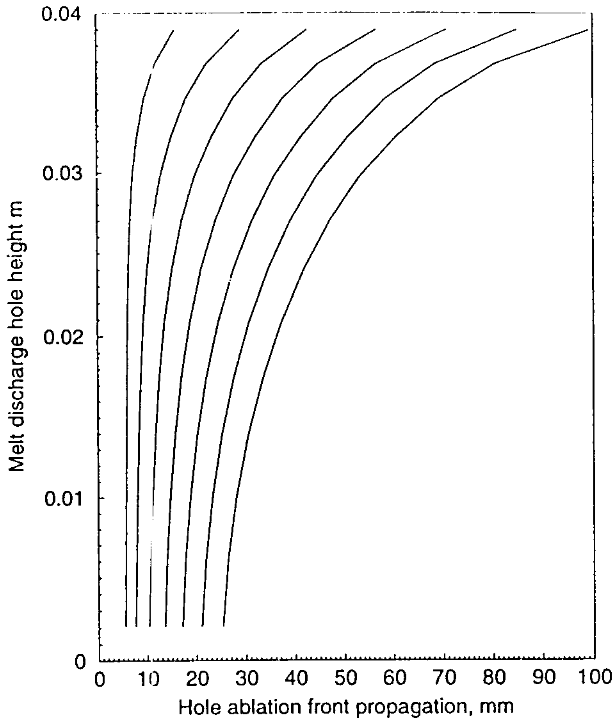

Figure 12: Case 2: $T_f - T_{w,mp} = 500\text{K}$.

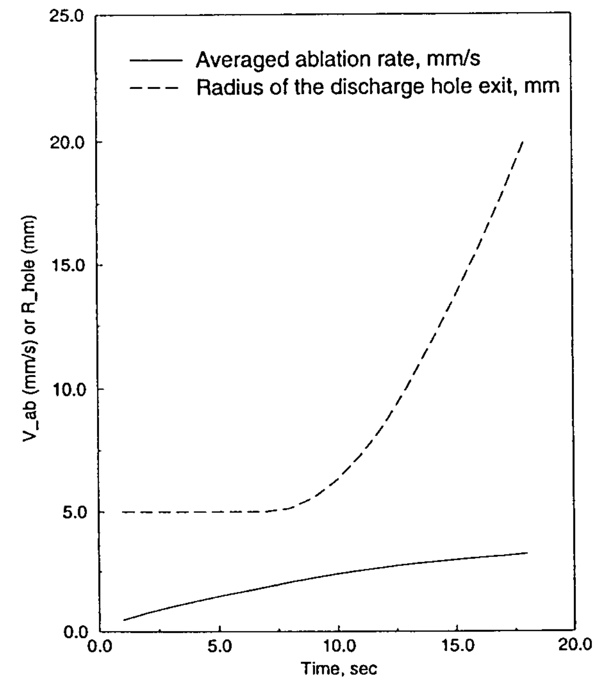

Figure 11: HAMISA simulation of KTH hole ablation experiment: case 1.

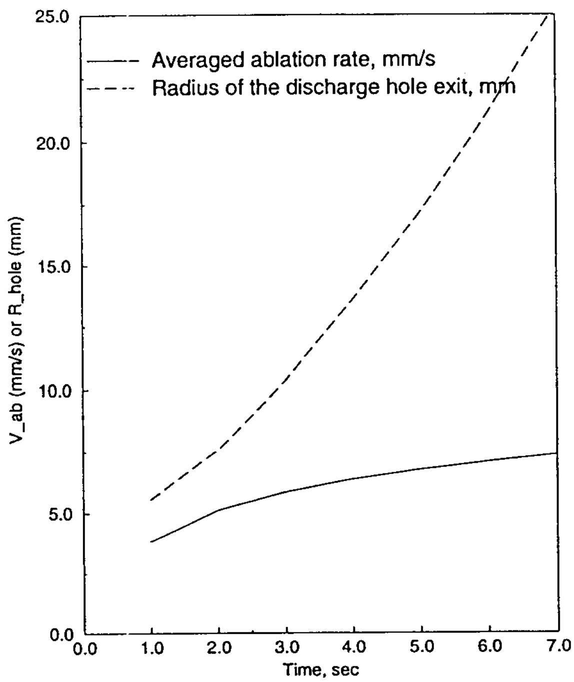

Figure 13: HAMISA simulation of KTH hole ablation experiment: case 2.

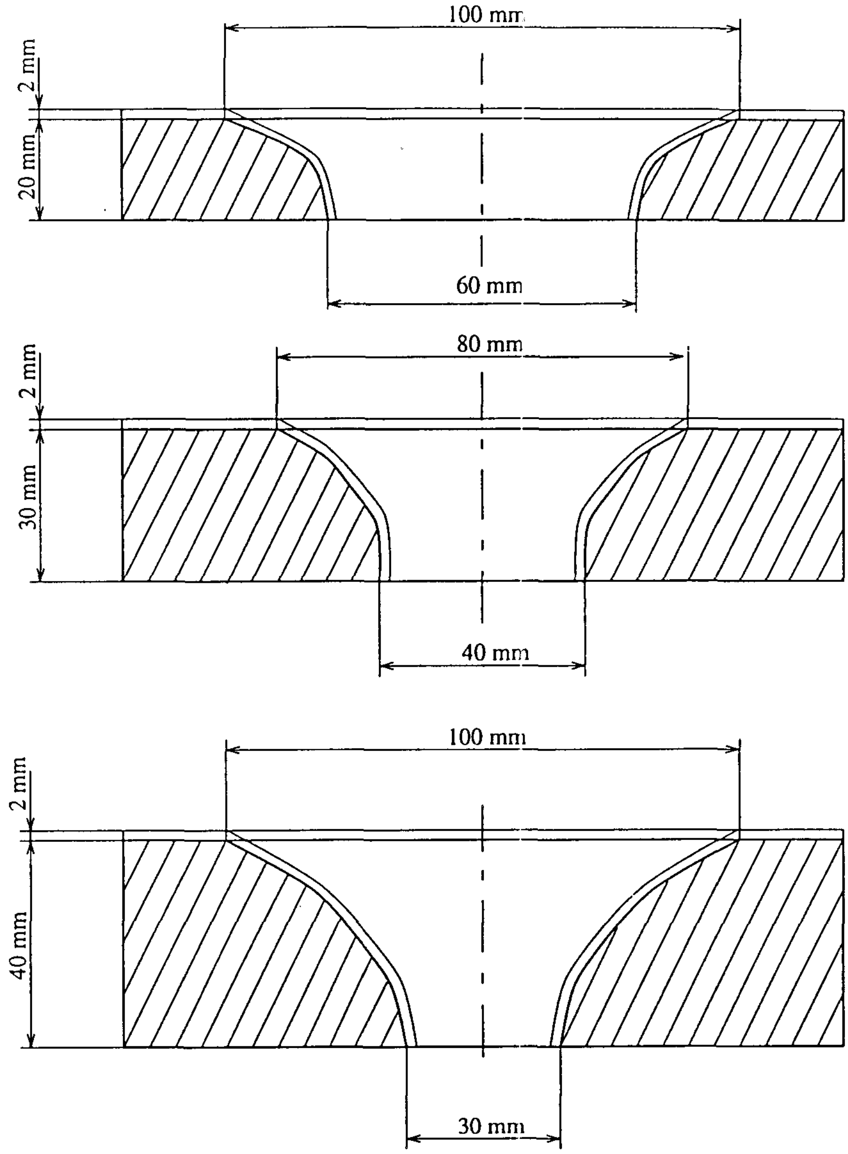

Figure 14: Final hole geometry in the KTH scoping hole ablation experiments: observations on 3 plates.

4 Summary

This paper describes the model development work performed at the Royal Institute of Technology, Stockholm, to study the core melt discharge and reactor pressure vessel (RPV) lower head ablation. The objective of the study is to provide understanding of the physics of these complicated melt-structure interaction processes. Phenomenological and computational models were developed to treat together the dynamically-coupled processes of melt flow, heat transfer to vessel wall, and the hole ablation. The most difficult, and the most uncertain, part of the modeling is the thermal and mechanical behavior of the crust, which can limit the ablation in severe light water reactor accidents. Other significant phenomena e.g., hole flow entrance effects, multi-dimensional heat conduction phase change in lower head wall, and melt pool thermal hydraulics also have been discussed in some detail. By taking advantage of these developments, we believe, it is possible to reduce the uncertainties in the quantification of the continued enlargement of the initial failure site in the RPV lower head.

Calculations, using the mechanistic models developed, have confirmed the effects of core melt momentum and heat transport properties (μ, κ) and their temperature dependence. The current modeling has also highlighted the importance of the wall thickness and thermal properties in the scaling considerations for the hole ablation experiments. Further progress in model development and validation relies on analysis of further hole ablation experiments. The HAMISA model, when validated, will form the basis be valid for prediction of the hole ablation dynamics during the melt discharge process in reactor accidents of interest.

ACKNOWLEDGEMENT

The authors would like to thank Dr. M.M. Pilch of Sandia National Laboratories for the information he provided us on the Sandia experiments. Special thanks are due to Mr. J. Andersson , who performed the scoping hole ablation experiments at KTH.

NOMENCLATURE

Arabic letters

C_D	Discharge coefficient (-), see eq.(4)
D	Diameter (m)
f_{app}	Apparent friction factor (-), see eq.(3)
Fr	Froude number, $Fr = \frac{U_{ejection}}{\sqrt{g \cdot D_{hole}}}$ (-)
g	Gravitational acceleration (9.81 m/s^2)
h	Heat transfer coefficient (W/m^2·K)
H	Melt pool level (m)
H_{fusion}	Heat of fusion (J/kg)
L, L_{wall}	Given thickness of the RPV wall (m)
Nu	Nusselt number, $Nu = \frac{hD_{hole}}{\kappa_f}$
Nu_{up}	Nusselt number, $Nu_{up} = \frac{q_{up}(r^*)D_{hole}}{\kappa_f(T_f - T_{f,mp})}$ (-)
P	Pressure (Pa)
Pe_{hole}	Peclet number, $Pe_{hole} = Re_{hole} \cdot Pr_f$ (-)
Pr	Prandtl number, $Pr = \mu C_p/\kappa$ (-)
r	Radius or distance from the hole symmetry line (m)
r^*	Dimensionless radius, $r^* = \frac{r - r_{hole}}{r_{pool} - r_{hole}}$ (-)
Re_{hole}	Reynolds number based on D_{hole}, $Re_{hole} = \rho_f U_{ejection} D_{hole}/\mu_f$ (-)
Re_z	Reynolds number based on Z, $Re_z = \rho_f U_{ejection} Z/\mu_f$ (-)
q	Heat flux (W/m^2)
t	Time (s)
U	Velocity in z-direction (m/s)
V	Velocity in r-direction (m/s)
z, Z	z-coordinate (m)
z_+	Dimensionless z for heat transfer data, $z_+ = \Delta z/(D_{hole} \cdot Pe_{hole})$ (-)
z_*	Dimensionless z for friction data, $z_* = \Delta z/(D_{hole} \cdot Re_{hole})$ (-)

Greek letters

δ	Thickness of layers (m)
κ	Heat conductivity (W/m·K)
μ	Dynamic viscosity (Pa·s)
ρ	Density (kg/m^3)
τ_{growth}	Solidification time scale (s)
τ_{remelt}	Remelting time scale (s)

τ_{conv}	Convection time scale (s)
τ_{res}	Residence time scale (s)
ξ	Friction coefficient
ΔP	Pressure difference (Pa)
Δt	Time step (s), see eq.(13)
Δz	Distance from the discharge hole inlet (m)

Subscripts

ab	Vessel wall ablation
cond	Conduction
conv	Convection
cr,crust	Crust of core melt or simulant material
f	Core melt flow
fbl	Boundary layer of discharge flow
film	Falling film characteristics of the molten wall layer
fs	Simulant material of core melts
gb	Gas blowthrough
hole	Discharge hole
int	Interface
ml	Molten layer
o	Reference value
pool	In-vessel melt pool
t	Turbulent
transition	Laminar-to-turbulent transition
up	Upper surface of the crust overlying the vessel wall
w	Vessel lower head wall or its model

References

[1] J.L.Rempe et al., Light Water Reactor Lower Head Failure Analysis, NUREG/CR-5642. USNRC. 1992.

[2] M.M. Pilch, Continued Enlargement of the Initial Failure Site in the Reactor Pressure Vessel, Appendix J of [3].

[3] M.M. Pilch, H. Yan and T.G. Theofanous, The Probability of Containment Failure by Direct Containment Heating in Zion, NUREG/CR-6075, SAND93-1535. June 1993.

[4] Zion Probabilistic Safety Study, Commonwealth Edison Co., Chicago, IL. 1981.

[5] J.J. Sienicki and B.W Spencer, Superheat Effects on Localized Vessel Breach Enlargement During Corium Ejection, Trans. ANS, Vol. 52 (1986), pp.522-524.

[6] M.M. Pilch, Personal Communications, April 1995.

[7] B.R. Sehgal, J. Andersson, T.N. Dinh and T. Okkonen, Scoping Experiments on Vessel Hole Ablation During Severe Accidents, Proceedings of the Workshop on Severe Accident Research in Japan, SARJ-4, Japan, Oct.-Nov., 1994, pp.230-236.

[8] T.N. Dinh and A.A. Popov, Molten Corium - Reactor Vessel Interaction: Scaling and Other Aspects, ASME 1993 Winter Annual Meeting, New Orleans, Louisiana,

USA. December 1993. Section 14C: Advanced Nuclear Power Plants, ASME paper 93-WA/HT-81, 1993.

[9] T.N. Dinh and R.R. Nourgaliev, On Turbulence Modeling of Large Volumetrically Heated Liquid Pools, Nucl. Eng. Des., 1995, to appear.

[10] C. Smoglie and J. Reimann, Two-Phase Flow Through Small Branches in a Horizontal Pipe with Stratified Flow, Intern. J. Multiphase Flow, Vol.12 (1986), N.4, pp.609-625.

[11] D.F. Gluck, J.P. Gille, D.J.Simkin and E.E. Zukowski, Distortion of the Liquid Surface under Low g Conditions, Aerospace Chemical Engineering, ed. D.J. Simkin, Vol.62 (1966), No.61, p.150, AIChE, NY.

[12] D.F. Gluck, J.P. Gille, E.E. Zukowski, and D.J.Simkin, Distortion of a Free Surface during Tank Discharge, J. Spacecraft, Vol.3 (1966), p.1691

[13] M.M. Pilch and R.O. Griffith, Gas Blowthrough and Flow Quality Correlations for use in the Analyses of High Pressure Melt Ejection (HPME) Events, SAND91-2322, Sandia National Laboratories, Albuquerque, NM, 1992.

[14] V.A. Bui and T.N. Dinh, An Approximation of Turbulent Prandtl Number in Thermally Developing Flows, Proceedings of the Second CFD Colloquium on Process Simulation, Helsinki University of Technology, Espoo, Finland, June 1995, pp.149-163.

[15] H. Schlichting, Boundary Layer Theory, Sixth Edition, McGraw-Hill Book Company, 1968.

[16] F.P. Incropera and D.P. de Witt, Fundamentals of Heat and Mass Transfer, Third Edition, John Willey & Sons, 1990.

[17] J.J. Sienicki, C.C. Chu, B.W. Spencer, W. Frid, and G. Löwenhielm, Ex-Vessel Melt-Coolant Interactions in Deep Water Pool: Studies and Accident Management for Swedish BWRs, Proceedings of the CSNI Specialist Meeting on Fuel-Coolant Interactions, Santa Barbara, January 5-8, 1993, NUREG/CP-0127, NEA/CSNI/R(93)8.

[18] M. Epstein, The Growth and Decay of a Frozen Layer in Forced Flow, Intern.J. Heat Mass Transfer, Vol.19 (1976), pp.1281-1288.

[19] A. Yim, M. Epstein, S.G. Bankoff, G.A. Lambert, and G.M. Hauser, Freezing-Melting Heat Transfer in a Tube Flow, Intern. J. Heat Mass Transfer, Vol.21 (1978), pp.1185-1196.

Paper No. 8

INFLUENCE OF MELT FREEZING CHARACTERISTICS ON STEAM EXPLOSION ENERGETICS

Timo Okkonen and Bal Raj Sehgal
Royal Institute of Technology (KTH)
Division of Nuclear Power Safety
Brinellv. 60, S-10044 STOCKHOLM, Sweden
Phone +46-8-7906587, Fax +46-8-7907678

ABSTRACT

This paper examines the freezing process of distinct melt particles interacting with water. Approximate time scales of freezing are estimated for some high-temperature melt materials that are of interest in experimental and reactor situations. Transient conduction calculations are performed to clarify the special freezing characteristics of oxidic melt materials (low conductivity) and binary melt mixtures (no definite freezing point). The transient calculations are compared with recent experiments indicating "non-explosivity" of Corium (UO_2-ZrO_2). One potential explanation, based on the freezing characteristics of binary Corium mixture, is proposed for the experimental observations. The numerical results are generalized by discussing the scaling implications of the thermal conduction analysis and by defining different freezing categories. Finally, conclusions are drawn on the potential influence of melt freezing characteristics on steam explosion energetics.

NOMENCLATURE

Bi_x	Biot number; $Bi = hx/k$ (-)
c_p	Specific heat capacity (J/kgK)
Fo_x	Fourier number; $Fo = \alpha t/x^2$ (-)
h	Specific enthalpy (J/kg) or Heat transfer coefficient (W/m^{2}K)
k	Thermal conductivity (W/mK)
k_B	Stefan-Boltzmann constant (W/m^2K^4)
q''	Heat flux (W/m^2)
q'''	Volumetric power (W/m^3)
r	Radial coordinate (m)
R	Particle radius (m)
t	Time (s)
T	Temperature (K)
α	Thermal diffusivity; $\alpha = k/\rho c_p$ (m^2/s)
Δh_{fus}	Heat of fusion (J/kg)
ΔT	Temperature difference (K)
Δx	Layer thickness (m)
ϵ	Emissivity (-)
ρ	Density (kg/m^3)
τ	Time scale (s)

Subscripts

0	Initial
c	Coolant
con	Conduction
l	Liquid
liq	Liquidus point
mp	Melting point
p	Particle
qs	Quasi-steady
rad	Radiative
s	Solid
sat	Saturation
sol	Solidus point

Superscripts

*	Dimensionless variable
'	Modified mushy-zone property

INTRODUCTION

Dynamic shock loads, which determine the immediate behaviour of structures enclosing the steam explosion zone in a light water reactor (LWR) vessel or cavity, have recently appeared as a focus of steam explosion modelling. At the same time, the initial conditions of interest have been extended from nearly saturated (in-vessel) to highly subcooled (ex-vessel) coolant conditions, with new limiting mechanisms coming into play. On the one hand, the thermal energy of the melt particles fragmented by the explosion wave cannot be assumed to be mixed instantly throughout the bulk coolant (even locally), inasmuch as the melt-coolant premixtures are typically quite lean in fuel. On the other hand, the melt-coolant premixing in a deep, subcooled, water pool can lead to relatively fast freezing of the melt particles, hence limiting the maximum thermal energy available for the explosion process. Such dynamical processes within the coolant and the melt phase have to be considered with care before the model predictions can be applied to reactor cases.

The present paper focuses on the melt freezing behaviour. The approximate time scales of melt freezing are first considered by assuming a uniform temperature profile inside the melt particle. Next the conditions, under which melt freezing could be limited by internal conduction, are examined. The conduction limitations are found important, and thus numerical freezing analyses are performed with a one-dimensional transient conduction model. These numerical results are compared with recent experiments on Corium-Water interactions, and one potential explanation for the "non-explosive" behaviour observed in the KROTOS tests is proposed. Further, an attempt is made to generalize the results by scaling and mapping of the melt particle freezing process. The thermal conduction analysis cannot capture all details, and in order to stimulate further work on the subject, some additional factors of interest are explored. Finally, conclusions are drawn on the potential influence of melt freezing characteristics on steam explosion energetics.

APPROXIMATE FREEZING TIMES

Under certain conditions, the internal temperature profile of a melt particle can be assumed to be uniform. With a uniform surface heat flux (q'') and a spherical melt particle of radius R_p, the specific enthalpy (h) changes according to the following equation.

$$\frac{4}{3}\pi R_p^3 \cdot \frac{d(\rho h)}{dt} = -4\pi R_p^2 \cdot q'' \tag{1}$$

In situations examined in the present study, the surface heat flux is dominated by thermal radiation and the surface temperature is much higher than that of the coolant environment. In this case, the following heat flux approximation can be employed.

$$q'' \sim q''_{rad} \sim \epsilon\sigma_B T^4 \tag{2}$$

If, in addition, the particle properties (density ρ; specific heat capacity c_p; emissivity ϵ) are assumed to be constant, substitution of Eq. (2) in Eq. (1) yields the following cooldown equation.

$$\frac{dT}{dt} \sim -\frac{3\epsilon\sigma_B}{\rho c_p R_p}T^4 \tag{3}$$

The time (τ_{liq}) taken to remove the superheat from a melt particle, whose initial temperature (T_0) is above the liquidus point (T_{liq}), can then be easily derived.

$$\tau_{liq} \sim \frac{\rho c_p R_p}{9\epsilon\sigma_B}\left(\frac{1}{T_{liq}^3} - \frac{1}{T_0^3}\right) \tag{4}$$

Subsequently, the time (τ_{sol}) taken to solidify, or to reach the solidus point (T_{sol}), is obtained.

$$\tau_{sol} \sim \frac{\rho c'_p R_p}{9\epsilon\sigma_B}\left(\frac{1}{T_{sol}^3} - \frac{1}{T_{liq}^3}\right) \tag{5}$$

$$c'_p = c_p + \frac{\Delta h_{fus}}{T_{liq} - T_{sol}} \quad (T_{sol} \leq T \leq T_{liq}) \tag{6}$$

With a definite freezing point ($T_{mp} = T_{liq} = T_{sol}$), instead of the temperature interval assumed above, the solidification time becomes

$$\tau_{sol} \sim \frac{\rho\Delta h_{fus} R_p}{3\epsilon\sigma_B T_{mp}^4} \tag{7}$$

where Δh_{fus} is the latent heat of fusion.

The formulae above depend on the assumption of a uniform internal temperature distribution (T) and dominance of radiative heat transfer ($q'' \propto T^4$), which is also a strong function of the *surface* temperature. Obviously, severe errors can be generated by the uniform temperature assumption if the conduction time scales are comparative with those of the quenching (freezing and cooldown) process.

Table 1: Material properties used in the present study.

Material	T_{liq} (K)	T_{sol} (K)	Δh_{fus} (kJ/kg)	k_l (W/mK)	k_s (W/mK)	ρ (kg/m^3)	$c_{p,l}$ (J/kgK)	$c_{p,s}$ (J/kgK)	α_l (10^{-7} m^2/s)	α_s (10^{-7} m^2/s)	ϵ (-)
UO_2	3113	3112.99	300	11	3	8300	470	390	28	9.3	0.8
Al_2O_3	2300	2299.99	1000	8	8	2500	1400	1400	23	23	0.8
Corium	2900	2800	360	10	2.5	8000	540	410	23	7.6	0.8
SS	1727	1671	300	20	40	6900	560	510	52	110	0.8

Solid-phase specific heat capacity ($c_{p,s}$) corresponds to the average value between 300 K and T_{sol}.
Liquid-phase density is applied for both phases; in reality, phase-specific densities differ.
Other properties are taken near the solidus (T_{sol}) or liquidus (T_{liq}) points.
Emissivities are assumed to be high (surface oxidized); the values may be overly high especially for Al_2O_3.

The material properties used in the present study are shown in Table 1, where "SS" stands for Stainless Steel and "Corium" for the binary mixture 80wt%UO_2-20wt%ZrO_2. The properties are approximated from Corradini (1991), CRC (1975), Incropera and DeWitt (1990), Rempe *et al.* (1993), and Roche *et al.* (1993).

The approximate time scales of superheat removal (τ_{liq}) and solidification (τ_{sol}) are shown in Table 2. These time scales are directly related to the particle size and are estimated for a spherical melt particle of radius $R_p = 1\ mm$. One can see that the time scales of superheat removal are low with initial melt superheat $T_0 - T_{liq} < 100\ K$, and that the complete freezing time is an order of magnitude higher. The conduction time scales, which are also included in Table 2, are discussed in the next section.

CONDUCTION LIMITATIONS

The time scale (τ_{con}) required for penetration of a thermal conduction front through a slab of thickness Δx_p, or a sphere of radius R_p, is given below.

$$\tau_{con,slab} = \frac{1}{C_{con,slab}} \frac{\Delta x_p^2}{\alpha} \tag{8}$$

$$C_{con,slab} \sim 1...10$$

$$\tau_{con,sphere} = \frac{1}{C_{con,sphere}} \frac{R_p^2}{\alpha} \tag{9}$$

$$C_{con,sphere} \sim 3...20$$

The numerical ranges given for the coefficient (C_{con}) correspond to $\Theta_{in}^* = (T_{in} - T_{out})/(T_0 - T_{out}) \sim 0.05...0.9$, which is the dimensionless temperature of the insulated inner surface after a constant temperature (T_{out}) has been imposed on the outer surface (Carslaw and Jaeger, 1959; Figs. 11 and 29).

If the conduction time scales are very short compared to the superheat removal (τ_{liq}) and freezing (τ_{sol}) time scales, the assumption of a uniform particle temperature is justified. Otherwise one has to account for the transient conduction limitations. The thermal diffusivities of the solid ($\alpha_{p,s}$) and liquid ($\alpha_{p,l}$) phases also may be different, making it necessary to use phase-specific properties. Although the above choice of the conduction time scale coefficient (C_{con}) is somewhat arbitrary, the following preconditions are adopted for "no transient conduction limitations".

$$\tau_{con,l} \sim \frac{\Delta x_p^2}{\alpha_l} << \tag{10}$$

$$\tau_{liq} \sim \frac{\rho c_p (T_0 - T_{liq}) \Delta x_p}{q''}$$

$$\tau_{con,s} \sim \frac{\Delta x_p^2}{\alpha_s} << \tag{11}$$

$$\tau_{sol} \sim \frac{\rho c_p' (T_{liq} - T_{sol}) \Delta x_p}{q''}$$

The first condition states that thermal conduction in the liquid phase must be much faster than the superheat removal process. The second condition, on the other hand, requires that thermal conduction in the growing solid layer (crust) be much faster than the solidification (crust formation) process. For the whole sphere, the "effective" melt depth can be approximated by $\Delta x_p \sim R_p/3$; one should also note that an outer crust of that thickness contains about two thirds of the particle volume (mass). In the preconditions above, the superheat removal (τ_{liq}) and freezing (τ_{sol}) time scales are expressed in terms of the surface heat flux (q''), however the formulae are basically equivalent with those of the previous section when radiative heat transfer dominates.

In addition to transient limitations, even the quasi-steady heat flux (q''_{qs}) on the particle surface could be limited by conduction. Assuming heat conduction through an

Table 2: Approximate time scales of freezing and conduction ($R_p = 1\ mm$).

Melt	τ_{liq} (s) $T_0 - T_{liq} = 10\ K$	τ_{liq} (s) $100\ K$	$\tau_{con,l}$ (s)	τ_{sol} (s)	$\tau_{con,s}$ (s)	$T_{sol} - T_{out,qs}$	$\frac{T^4_{out,qs}}{T^4_{sol}}$ (-)
UO_2	0.0030	0.029	0.040	0.19	0.12	410	0.57
Al_2O_3	0.0091	0.084	0.048	0.66	0.048	70	0.88
Corium	0.0045	0.042	0.048	0.36	0.15	330	0.60
SS	0.032	0.29	0.021	2.0	0.010	4.4	0.99

Conduction time scales ($\tau_{con,l}$, $\tau_{con,s}$) are estimated with $\Delta x_p \sim R_p/3$.
Quasi-steady crust outer temperature ($T_{out,qs}$) is estimated with $\Delta x_p \sim R_p/3$.

outer shell (Δx_p) on a spherical melt particle, the temperature difference (ΔT_p) over the layer is simply

$$\Delta T_p = \frac{R_p}{R_p - \Delta x_p} \frac{\Delta x_p}{k} q''_{qs} \tag{12}$$

where the thermal conductivity (k) is assumed to be constant; with an infinite radius (R_p), the first curvature term disappears. Next the spherical particle is assumed to radiate heat to a relatively cold environment, as in the previous section. Further, a quasi-steady balance is assumed to exist between solid-phase conduction and surface radiation. The following equation is obtained for determining the quasi-steady outer surface temperature ($T_{out,qs}$) with crust thickness $\Delta x_p \sim R_p/3$.

$$T_{sol} - T_{out,qs} \sim \frac{R_p}{2k} \epsilon_s \sigma_B T^4_{out,qs} \tag{13}$$

The conduction limitations can be particularly relevant with high surface heat fluxes and oxidic (ceramic) melt materials that have low thermal conductivity and diffusivity. This can be seen in Table 2, where the quasi-steady temperature ratio between the outer surface and the solidus point is given in the fourth power, because it represents the decrease in radiative heat flux during crust formation. Table 2 shows that internal conduction can limit freezing of a melt particle of radius $R_p \sim 1\ mm$, with the exception of metallic (SS) melt material with high conductivity. Also the solidification of small Alumina (Al_2O_3) particles may be free of solid-state conduction effects.

The criteria for "no transient conduction limitations", Eqs. (10) and (11), become fulfilled with smaller, submillimeter, particles. This is because the conduction time scales drop as square of the length scale, while the "bulk" freezing times are directly related to the particle size. Above, only the conduction time scales of the liquid phase (prior to surface crust formation) and the solid phase (after crust formation has begun) were considered. With melt materials that have different solidus (T_{sol}) and liquidus points (T_{liq}), the liquid and solid phases are separated by the "mushy zone". The effective heat capacity (c'_p) of the mushy zone is an order of magnitude higher than the non-phase-change values, and the conduction processes are, therefore, much slower. The effects of transient conduction and mushy zone formation are discussed in the next three sections.

TRANSIENT CONDUCTION MODEL

The model is based on the transient, parabolic (Fourier), heat conduction equation.

$$\rho c_p \frac{\partial T}{\partial t} = \nabla \cdot (k \nabla T) + q'''_v \tag{14}$$

Only one-dimensional situations are considered, in spherical geometry. Volumetric heat sources (q'''_v) can be included, but there are usually no sources of great significance for fast freezing processes, with the exception of metal oxidation. The latent heat of fusion (freezing) is treated by modifying the specific heat capacity (to c'_p) between the solidus (T_{sol}) and liquidus (T_{liq}) points, as shown in Eq. (6). The latent heat is distributed uniformly over the phase-change temperature interval. Other distributions (normal, parabolic, triangular, etc.) could be pursued, as well, but the uniform treatment suffices for the situations of interest here.

The only boundary conditions applied are the surface heat fluxes. While for the "inner" ("west") surface symmetric conditions are assumed, the "outer" ("east") boundary is assumed to radiate heat to the coolant environment treated as a perfect absorber.

$$q''_{west} = 0 \tag{15}$$

$$q''_{east} = \epsilon_{east} \sigma_B (T^4_{east} - T^4_c) \tag{16}$$

Certainly, also convective heat transfer would be involved in any real case, but the analyses of the present chapter focus on fast freezing at high melt temperatures (near typical melting or freezing points) where radiative heat transfer tends to dominate.

The numerical scheme is based on the standard control-volume approach, as outlined by Patankar (1980). In order to ensure insensitivity to nodalisation and time scales, the results were compared with those of analytical conduction solutions, including phase-change problems (Alexiades and Solomon, 1993; Carslaw and Jaeger, 1959; Lunardini, 1991). With proper selections on nodalisation and time steps, the fully explicit, half-implicit and fully implicit schemes all provide similar solutions. In all the calculations, a fairly dense grid and uniform node spacing are used. The boundary conditions and material properties are treated explicitly. When the node temperature is between the liquidus and solidus points - the so-called mushy regime - the control volume properties are estimated by linear interpolation between the solid and liquid-phase values.

In the present study, the conduction model is employed to predict the freezing behaviour of two high-temperature melts, namely pure aluminum oxide (Alumina; Al_2O_3) and a binary mixture of uranium dioxide and zirconium dioxide (Corium), interacting with saturated water at atmospheric pressure. Figs. 1 through 8 show the quenching behaviour of distinct, spherical, Corium and Alumina melt particles of radius $R_p = 1\ mm$ or $R_p = 3\ mm$. The horizontal lines (see, e.g., Fig. 3) mark the solidus and liquidus points. Calculations are performed with a uniform grid of 101 nodes, and the "tightly packed" curves represent temperatures of the 11 surface nodes. The initial superheat of the Corium droplet is assumed to be either $T_0 - T_{liq} = 100\ K$ or $200\ K$, and that of Alumina either $T_0 - T_{liq} = 200\ K$ or $300\ K$. Only radiative heat transfer from the melt particles to water is accounted for, with emissivity $\epsilon = 0.8$. As noted in Table 1, the selected emissivity may be too high for Alumina, but the neglect of convective film-boiling heat transfer works into the other direction and compensates for part of the overrated radiation. Anyway, for our purposes here, the parameters provide an adequate basis.

Corium and Alumina behave differently under freezing. Corium, being a binary mixture, freezes over a finite temperature interval, whereas Alumina has a definite freezing point typical for pure oxides. The freezing (solidus) fronts propagate similarly in both materials; see the "accumulated" curves of Figs. 1 and 5. However, the liquidus front can penetrate fast throughout the Corium particle, with the related time scale depending on the particle size and

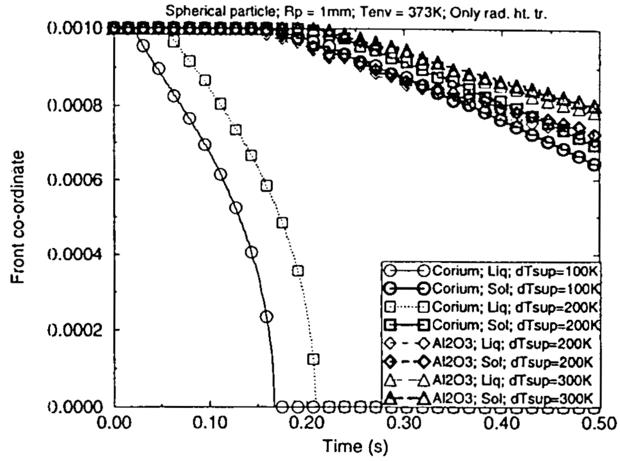

Figure 1: Penetration of the solidus and liquidus fronts into a spherical melt particle of radius 1 mm.

the liquid-phase thermal diffusivity. The conduction limitations become obvious when comparing the approximate time scales of superheat removal and freezing (Table 2) with the transient results for Corium. Complete superheat removal or freezing takes much longer than given by the approximations based on a uniform particle temperature. The penetration rate of the liquidus front is of the same order of magnitude as indicated in Table 2 ($R_p/3\tau_{con,l}$). As shall be seen in the section on "Scaling and mapping", the solidus-liquidus temperature difference ($T_{liq} - T_{sol} = 100\ K$ used here) can affect the maximum depth of fast liquidus front penetration. The temperature profiles of the 1-mm-radius Alumina particle, on the other hand, indicate rather uniform behaviour. In fact, the approximate time scales of superheat removal (τ_{liq}) and freezing (τ_{sol}) are not greatly in error.

When the liquidus line reaches the Corium particle centre, the whole inner core is in the mushy regime surrounded by a harder solid crust. This conduction process takes only a fraction of a second with the 1-mm-radius particle and roughly one second with the 3-mm-radius particle. At these moments, the respective Alumina particle has a relatively large liquid core and a solid crust, the thickness of which is not more than one tenth of the particle radius. The outer crust may also get cracked and loosened due to various sources of stress (flow friction, temperature gradients, particle-particle contact, etc.), in which case the freezing is somewhat enhanced. For the outer crust of the Corium particle, large temperature gradients and decrease in surface heat flux are predicted. This is consistent with the quasi-steady analysis of Table 2 [$(T_{out,qs}/T_{sol})^4$)].

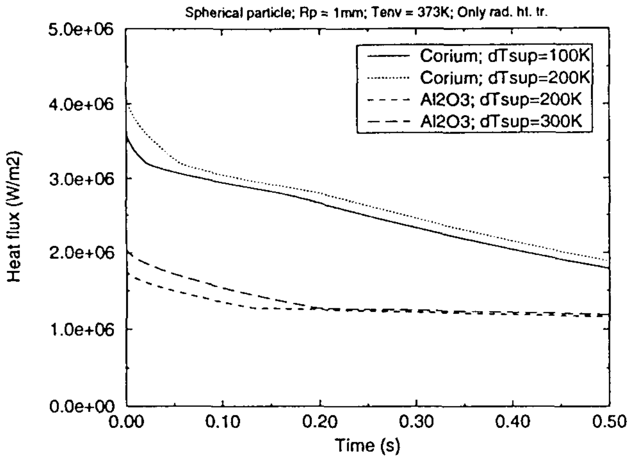

Figure 2: Surface heat flux of a spherical melt particle of radius 1 mm; only radiative heat transfer accounted for.

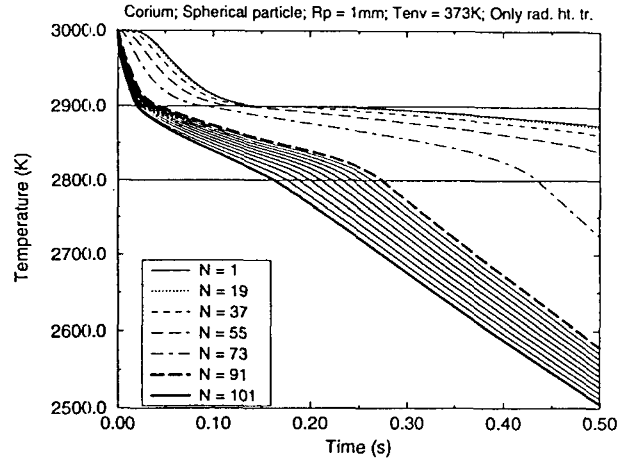

Figure 3: Corium particle temperature profile; radius 1 mm; $T_0 - T_{liq} = 100\ K$.

EXPERIMENTAL CASES

Interesting observations have recently been made in the KROTOS steam explosion experiments at JRC-Ispra (Hohmann *et al.*, 1993; 1994). In several KROTOS tests, where about 1.5 kg of Alumina melt has been poured into water at atmospheric pressure, steam explosions have occurred. In nearly saturated water, the explosion has been triggered by an external pressure pulse, whereas under subcooled conditions also spontaneous explosions have occurred. In the KROTOS-28 and 29 tests with low and high subcooling, respectively, the Alumina melt had penetrated deep into water, before the explosion was artificially (28) and spontaneously (29) triggered. At this moment, most of the discharged melt was present in the melt-water mixing zone, yet causing only moderate voiding. Based on the melt penetration velocity, it can be estimated that some of the melt particles had interacted with water for more than one second and some much less prior to triggering. From Figs. 1 through 8 one can make the order-of-magnitude assessment that melt particles of radius $R_p > 1\ mm$ could have been largely unfrozen (with perhaps a thin outer crust if not loosened), whereas sub-millimeter particles produced early in the interaction were probably almost completely solid. As mentioned above, the emissivity of Alumina can be lower (see, e.g., Table A.11 of Incropera and DeWitt, 1990) than $\epsilon = 0.8$ used here, so that the freezing may be slower, too. In the other Alumina-Water explosions (KROTOS-26 and 30), the melt did not travel very deep, and the quenching was therefore limited prior to triggering. For the explosive Alumina-Water interaction tests, the post-test debris examination cannot reveal the pre-explosion particle sizes. In the KROTOS-27 test with low subcooling, no explosion took place, and only one tenth of the debris mass was found to have a final radius of $R_p < 3\ mm$. This implies that the Alumina freezing characteristics resembled those of the above-described calculations with $R_p = 3\ mm$, and larger.

In sharp contrast to the Alumina-Water interaction tests, no explosions have been observed in the KROTOS Corium-Water interaction tests (Hohmann *et al.*, 1994; Huhtiniemi, Hohmann and Magallon, 1995). They have been conducted with about 3 kg of melt, with or without artificial pressure pulses, and under nearly saturated or highly subcooled coolant conditions. In the KROTOS-35 test with low water subcooling, vigorous steaming led to substantial melt expulsion from the test vessel. The trigger device was activated only after a couple of seconds, which was probably too late from the melt quenching point of view (Hohmann *et al.*, 1994). In the KROTOS-36 test with high subcooling, the triggering device was activated, successfully, after melt indication at the middle of the 1-m-deep water pool, but again vigorous steaming caused significant melt expulsion. The KROTOS-32 and 33 tests were similar to the above tests, however no artificial triggering was used. The KROTOS-37 test setup was similar to that of KROTOS-36, but now the inner diameter of the test section was much larger than before (20 cm instead of 9.5 cm). The coherent melt jet penetrated at least a few tens of centimeters into the water pool, and the triggering

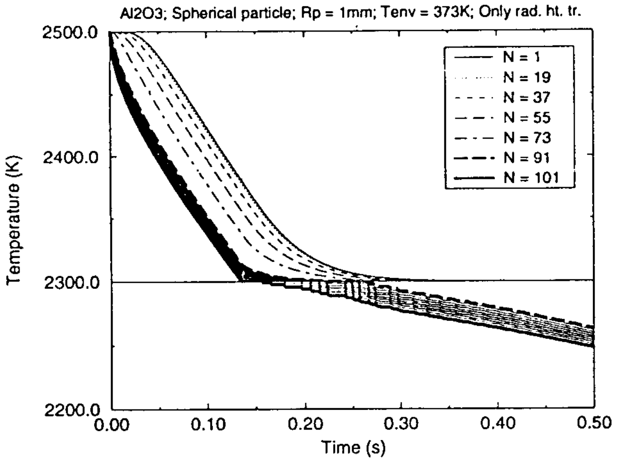

Figure 4: Al_2O_3 particle temperature profile; radius 1 mm; $T_0 - T_{liq} = 200\ K$.

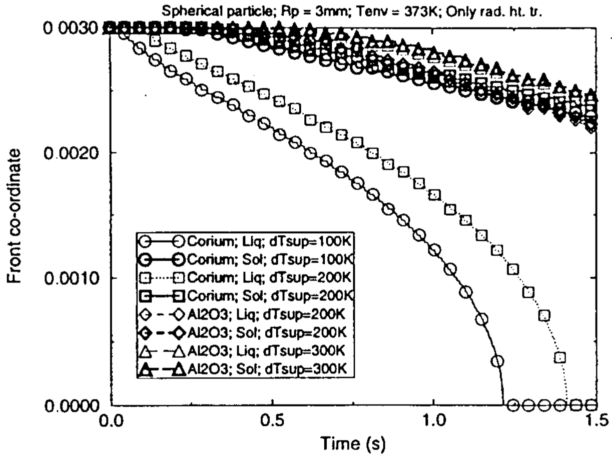

Figure 5: Penetration of the solidus and liquidus fronts into a spherical melt particle of radius 3 mm.

device was activated from the mid-elevation temperature signal. Nevertheless, no explosion occurred, which may have been due to the reduced trigger pulse, as the trigger energy was kept constant but the test section was larger. Similarly to the Alumina-Water tests, the Corium melt particles may have interacted with water over a time period up to about one second before the artificial pressure pulse. Figs. 1 and 5 show that the penetration of the mushy region can be a fairly rapid process, though here one can also anticipate uncertainties in basic melt properties (liquidus and solidus points), initial conditions (initial superheat), and other typical characteristics of binary mixtures (see the section on "Additional factors of interest"). In the post-test examinations, roughly one third of the Corium particle mass has been found with a radius of $R_p < 1\ mm$, one third with $R_p > 2\ mm$, and almost no particles with $R_p > 3\ mm$ (Huhtiniemi, Hohmann and Magallon, 1995; Fig. 5). This implies that the Corium freezing characteristics were close to those of the above-described calculations with $R_p = 1\ mm$.

Additional tests (KROTOS-38, 40 and 41) have been conducted with Alumina melt discharged into a test section with a larger inner diameter. In KROTOS-38, a spontaneous explosion took place before triggering, and a non-triggered explosion occurred also in the KROTOS-40 experiment, where the melt was initially very much superheated. In the KROTOS-41 test, on the other hand, the saturated coolant conditions probably prevented spontaneous explosion, similarly to the KROTOS-27 test with a smaller test section. The coolant voiding at the instant of triggering has been reported to have been much greater in the KROTOS-37 test with Corium than in the KROTOS-38 test with Alumina melt (Hohmann *et al.*, 1994). This may be a combined effect of the differences in melt temperatures, fragmentation and emissivity. The melt-water heat transfer is governed by these factors and so is the melt quenching behaviour, indicating that Corium, indeed, freezes faster.

The main trend appears to be that Alumina-Water explosions are not self-triggered under saturated coolant conditions, but explosions do occur if external triggering is used or if the coolant is significantly subcooled. Corium-Water interactions appear - to say the least - much less explosive, however the reasons for this have to be well understood before one can generalize the KROTOS data to large-scale situations. Here it is worth emphasizing that the KROTOS tests are the first steam explosion experiments with Corium, and that the past tests have usually been conducted with pure materials (see, e.g., Corradini, 1991). Earlier KROTOS tests with Tin/Water interactions involved externally triggered explosions (Hohmann *et al.*, 1993). This is no surprise in the light of the melt quenching behaviour, as significantly superheated metallic melt particles can remain in liquid form over relatively long time periods. In fact, the superheat removal time scales are particularly long for metallic melts with a low melting point (lower heat fluxes) and high thermal conductivity (uniform temperature). Such melt materials as tin (Sn) and aluminum (Al), which are frequently applied in melt-water interaction tests, certainly fall into this category.

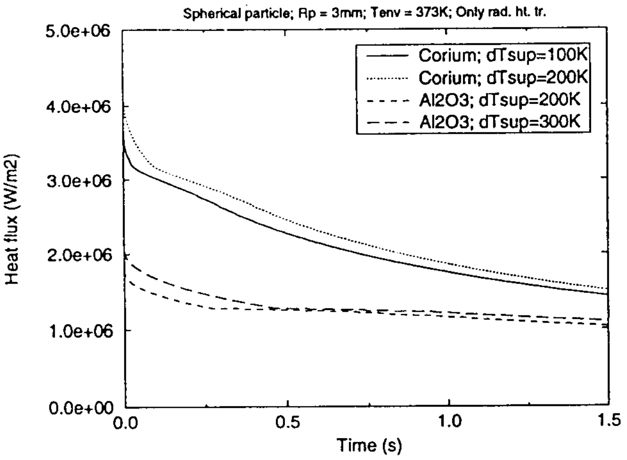

Figure 6: Surface heat flux of a spherical melt particle of radius 3 mm; only radiative heat transfer accounted for.

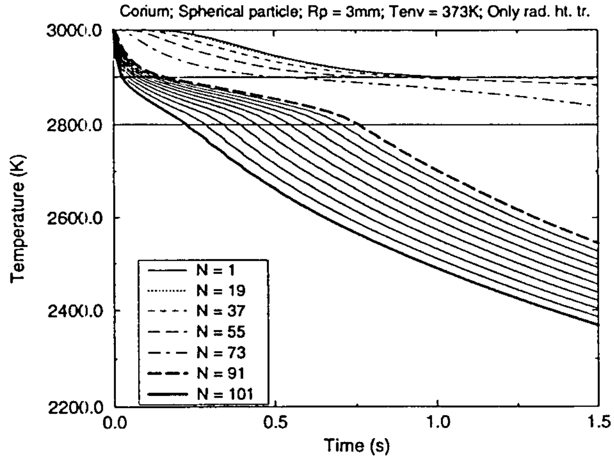

Figure 7: Corium particle temperature profile; radius 3 mm; $T_0 - T_{liq} = 100\ K$.

We believe that the freezing characteristics of a high-temperature binary mixture, such as Corium, may be the reason for the observations in the KROTOS experiments. The general hypothesis proposed here is that the structure of the melt particle is strongly influenced by thermal (freezing) behaviour. The internal structure can change as the particle falls and cools down in water, and it can, later, affect the dynamic melt behaviour and eventual participation in an explosion. The melt particle conditions depend on the melt (jet) breakup and the melt-water mixing zone behaviour, which also can differ between various melt materials. More tests are needed before one can be certain about the governing factors.

It should be noted that we do not claim Corium to be non-explosive as such, but rather that Corium particles can become non-explosive relatively fast when interacting with water. Consequently, additional Corium-Water interaction tests should be performed with higher melt superheats, earlier triggering, and perhaps with pure UO_2, too. Further, single-droplet tests should be pursued with binary melt mixtures (Corium, simulants) to find the time scales in which they become non-explosive. These time scales would be crucial for estimating the potential energetics of ex-vessel melt-water interactions. If the time scales are found essentially zero with reasonable trigger energies, it is justified to call Corium "non-explosive". Finite time scales, on the other hand, can be used to envelope the melt masses that could take part in an explosion. Such freezing-induced limitations of the steam explosion energetics concern subcooled coolant conditions, in particular. Under saturated conditions, coolant voiding becomes the limiting factor and, in addition, spontaneous triggering is less likely. In this respect, coolant voiding and melt freezing can be seen as complementary effects (see, e.g., Theofanous *et al.*, 1994).

SCALING AND MAPPING

The one-dimensional heat conduction equation [Eq. (14) with $q''' = 0$] is given in dimensionless form below.

$$\frac{\partial T^*}{\partial Fo} = \nabla^{*2} T^* \tag{17}$$

$$T^* = T_0^* \quad at\ Fo = 0 \tag{18}$$

$$-\nabla^* T^* = 0 \quad at\ x^* = 0 \tag{19}$$

$$-\nabla^* T^* = q''^* \quad at\ x^* = 1 \tag{20}$$

where

$$T^* = \frac{T - T_{sol}}{T_{liq} - T_{sol}}$$

$$r^* = \frac{r}{R}\ ;\ \nabla^* = R\,\nabla$$

$$Fo = \frac{\alpha t}{R^2}\ ;\ Fo' = \frac{\alpha' t}{R^2}$$

$$q''^* = \frac{q'' R}{k(T_{liq} - T_{sol})}$$

$$\alpha = \frac{k}{\rho c_p}\ ;\ \alpha' = \frac{k}{\rho c_p'}$$

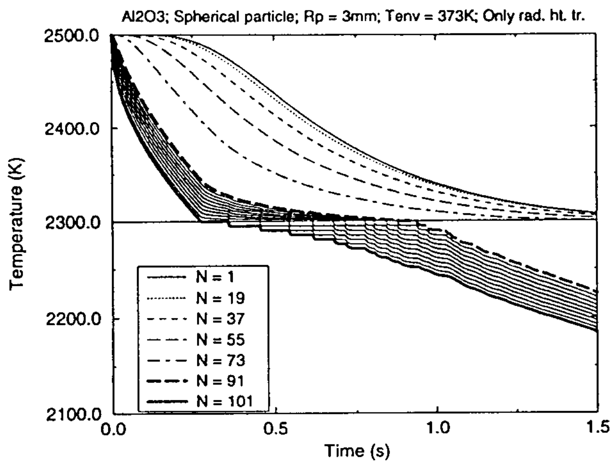

Figure 8: Al_2O_3 particle temperature profile; radius 3 mm; $T_0 - T_{liq} = 200\ K$.

The radius of a spherical particle (R) is selected as the length scale, with the dimensionless radial co-ordinate (r^*) varying from zero to one. The temperature is non-dimensionalized by the liquidus (T_{liq}) and solidus (T_{sol}) points, between which the dimensionless temperature (T^*) can be considered as "liquid fraction"; this is provided that the properties are constant. While time is converted to the Fourier number (Fo), the dimensionless surface heat flux gives the ratio of outward flux and internal conduction. Finally, the thermal diffusivity (α) is modified (α') to account for heat of fusion during freezing. The prototypic material and the simulant should comprise similar penetration characteristics of the solidus and liquidus fronts (in dimensionless time). For this, one needs to maintain the dimensionless temperatures and surface heat flux, as well as the ratio of thermal diffusivities (α/α').

It is not likely that all phase-specific diffusivities (α_{liq}, α', α_{sol}) and the dimensionless heat flux (q''^*) can be matched. Consequently, numerical analyses have to be performed when interpreting the simulant test results and extrapolating them to prototypic situations. Figs. 9 and 10 show an example of the scaling principles described above. The numerical analyses are performed first for a Corium particle of radius $R_p = 1\ mm$ and initial superheat $T_0 - T_{liq} = 100\ K$. The temperature difference between solidus and liquidus temperature is assumed to be the "best-estimate" $T_{liq} - T_{sol} = 100\ K$, or ten times lower (10 K). The initial temperature and the freezing point of the simulant melt material are assumed to be 1000 K lower than those of Corium, which means that the initial radiative heat flux is lowered by a factor of about five. The conductivities are chosen, accordingly, to be five times lower than those of Corium. Some scaling distortion is created by the non-linear temperature dependence of the surface heat flux, yet the penetration of the solidus and liquidus fronts is still almost the same for Corium and simulant. The influence of the solidus-liquidus temperature difference can also be seen in Figs. 9 and 10, where the middle curves represent the thinner mushy zone. In a final analysis, also the convective part of the film-boiling heat transfer has to be included, especially with lower melt temperatures and subcooled coolant conditions.

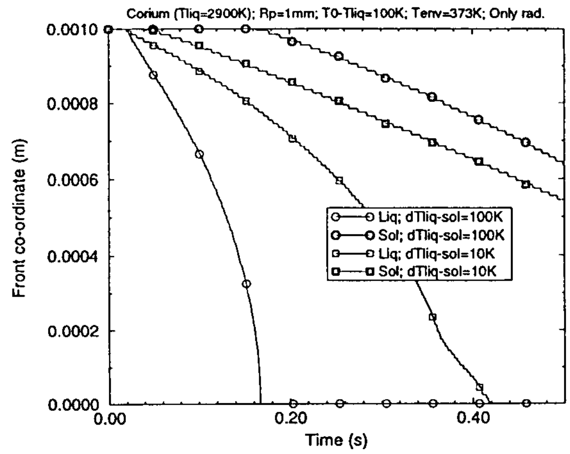

Figure 9: Penetration of the solidus and liquidus fronts into a Corium melt particle of radius 1 mm.

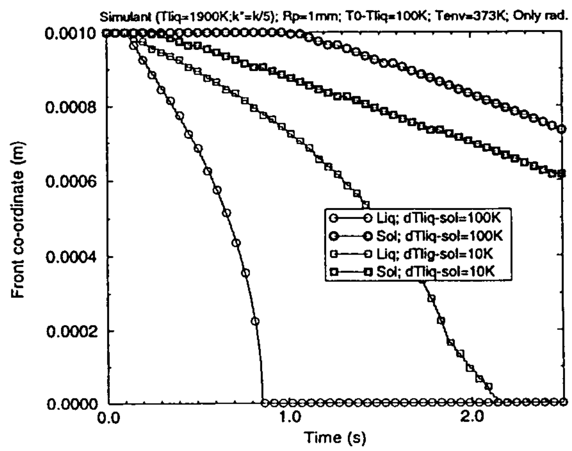

Figure 10: Penetration of the solidus and liquidus fronts into a simulant melt particle of radius 1 mm.

For definition of the various freezing categories, the conduction limitation criteria [Eqs. (10) and (11)] are employed, however now the time scale ratios[1] are used, as shown below.

$$\frac{\tau_{con,l}}{\tau_{liq}} = \frac{q''\Delta x_p}{k_l(T_0 - T_{liq})} \tag{21}$$

$$\frac{\tau_{con,s}}{\tau_{sol}} = \frac{q''\Delta x_p}{k_s[(T_{liq} - T_{sol}) + \frac{\Delta h_{fus}}{c_p}]} \tag{22}$$

Table 3 gives the figures of merit for a particle of radius $R_p = 1\ mm$ and initial superheat $T_0 - T_{liq} = 100\ K$; see also Tables 1 and 2. The length scale is approximated by one third of the radius ($\Delta x_p = R_p/3$) and the initial radiative heat flux (q_0'') represents the surface heat flux. For all properties without phase specification (subscript l or s), the average properties are used.

Table 3: Figures of merit for mapping of freezing ($R_p = 1\ mm$).

Melt	$T_0 - T_{liq}$ (K)	q_0'' (MW/m^2)	$\frac{\tau_{con,l}}{\tau_{liq}}$ (-)	$\frac{\tau_{con,s}}{\tau_{sol}}$ (-)	$q_0''^*$ (-)
UO_2	100	4.8	1.5	0.77	∞
Al_2O_3	100	1.5	0.63	0.088	∞
Corium	100	3.7	1.2	0.57	5.9
SS	100	0.51	0.084	0.0068	0.30

Time scale ratios are estimated with $\Delta x_p \sim R_p/3$.

The first time scale ratio ($\tau_{con,l}/\tau_{liq}$) of Table 3 reflects the potential for crust formation prior to bulk freezing. As discussed in previous sections, only metallic melts (SS above) can resist early crust formation. The second time scale ratio ($\tau_{con,s}/\tau_{sol}$) represents the importance of solid-phase conduction limitations while the crust is growing inwards. Such limitations are apparent for UO_2 and Corium. Finally, if the initial dimensionless heat flux ($q_0''^*$) is low, the mushy regime can be thick compared to the melt particle size. One can see that the selected stainless steel (SS) properties allow mushy zone formation throughout the particle, while the Corium properties (used here) indicate a more limited mushy zone thickness.

[1]These time scale ratios and the dimensionless heat flux (q''^*) can be seen as "modified" Biot numbers. The traditional Biot number ($Bi_R = hR/k$) criterion for a uniform internal temperature profile, say $Bi_R << 1$ (see Fig. 5.15 of Incropera and DeWitt, 1990), is not applied here. This is due to the phase-change process and the fact that the temperature variations of interest are small compared to the particle-coolant temperature difference. The relative temperature variations are small - yet important.

It appears prudent to expect freezing-related differences between three basic configurations: (i) a superheated metal-type melt droplet, (ii) an oxide-type melt particle with a solid crust and liquid inside, and (iii) a mixed-type (binary, ternary) melt particle with a liquid core, an intermediate mushy region and some crust on top.

ADDITIONAL FACTORS

At this point, it is necessary to stress the limitations of the thermal conduction model, which are listed and commented upon as follows.

- *One-dimensionality.* Some two-dimensional effects might be induced by the film-boiling heat fluxes and the internal melt particle behaviour. On the other hand, there are also indications that melt particles are spinning while falling through water.
- *Parabolic conduction.* Hyperbolic (non-Fourier) conduction might be of interest in some situations, where the freezing process is fast and involves two "phases" (liquid and solid; solid and interstitial pores).
- *No interdiffusion.* The formation of the mushy zone depends on the relative efficiency of the diffusion of heat (conduction) and species (interdiffusion). The thermal diffusivity, however, is typically much higher than the binary diffusion coefficients and the process thus thermally governed.
- *No supercooling.* Fast freezing might involve melt supercooling, with somewhat delayed crystallization and latent heat release.
- *No voiding.* Voids can develop during solidification, since the solid-phase density is generally higher than that of the liquid phase.
- *No convection.* Melt convection may cause the liquid-phase conductivity to be effectively higher. For solid-phase conduction-limited freezing processes, internal convection is probably not a major factor. The influence can be studied by increasing the liquid-phase conductivity.
- *No deformation.* The form of the melt particles can deviate from spherical. A major part of the frozen melt particles found in experiments is usually in a more or less spherical form. In fact, large deformation appears to cause fragmentation.

- *No fragmentation.* Continuous removal of the solid crust layer, and even major fragmentation caused by particle-coolant and particle-particle interactions, can enhance the freezing process. If major fragmentation is fast compared to thermal processes, as typical, the freezing analysis can be performed with the final particle sizes (estimated or measured).
- *No heat generation.* Decay heat contribution is typically minor, however exothermic metal oxidation can delay the freezing process.

Concerning the additional factors above, no final statements can be made here. Nevertheless, the one-dimensional thermal conduction analysis can capture the most salient features of the melt particle freezing process, and forms the basis for additional considerations.

CONCLUSIONS

The quenching (freezing and cooldown) of melt particles is one of the major factors affecting the ex-vessel steam explosion loadings. It is obvious that solidified melt particles cannot take part in an explosion, and, consequently, the time scales of freezing are of primary interest. The quenching depends, first of all, on the surface heat fluxes and any other heat sources such as exothermic metal oxidation. In the previous sections, the approximate freezing time scales were estimated, but it was also found that the neglect of internal conduction limitations may lead to an underestimation of the freezing times. Transient conduction analyses were performed to explore potential conduction effects, which depend on the particle size and properties. When considering the importance of internal conduction, one should also note that the surface shell includes most of the sphere mass, and that shock-wave-induced fragmentation may be resisted prior to complete freezing.

The explosive melt fragmentation behaviour may, indeed, depend on the state of the melt particle just prior to shock wave-induced acceleration. A mushy particle can be particularly "stiff" due to internal crystal formation and subsequent increase in effective surface tension and viscosity, while a mostly liquid droplet can only resist moderate forces without fragmenting. It appears prudent to expect differences between three basic configurations: (i) a superheated metal-type melt droplet, (ii) an oxide-type melt particle with a solid crust and a liquid core, and (iii) a mixed-type (binary, ternary) melt particle with a liquid core, an intermediate mushy region and some crust on top. The transitions between these categories depend on material properties and the thickness of the solid and mushy layers.

We believe that the high surface heat fluxes, the relatively low initial superheats, and the strongly temperature-dependent properties of Corium could be the key to the recent observations in the KROTOS tests (no explosions, yet, with Corium). With binary melt mixtures, the properties change continuously during freezing, in contrast to pure melt materials which exhibit "sudden" solidification. Single droplet experiments should be performed to understand fragmentation of the mixed-type melts, both before and during the explosion propagation phase. With additional data on the time scales that can make the melt particles non-explosive, or at least more resistant to fast fragmentation, the freezing models could be employed to predict ex-vessel reactor situations.[2] Needless to say, also the properties of various core melt mixtures, the pre-explosion particle sizes, as well as the vessel melt release conditions, are crucial for the estimates on ex-vessel steam explosion energetics.

ACKNOWLEDGEMENTS

The critical, constructive, comments of Dr. T.N. Dinh (KTH) and Dr. J. Green (KTH) are gratefully acknowledged.

REFERENCES

Alexiades V, Solomon AD (1993). *Mathematical Modeling of Melting and Freezing Processes.* Hemisphere. 1993.

Carslaw HS, Jaeger JC (1959). *Conduction of Heat in Solids.* Second Edition. Oxford University Press. 1959.

Corradini ML (1991). Vapor Explosions: a Review of Experiments for Accident Analysis. *Nuclear Safety,* Vol.

[2]In melt-water interaction codes with Lagrangian particle grouping, one could apply a transient or a quasi-stationary approach for calculating the internal melt particle behaviour; the transient calculation times could be minimized by grid optimization. It may not be possible to perform such analyses with multifield codes that employ single phase-specific temperatures, though some type of "constitutive" relations could be developed to remove mass from the melt phase to the non-explosive (solid) debris phase.

32, No. 3, July-September 1991.

CRC (1975). *Handbook of Chemistry and Physics.* 56th Edition. CRC Press. 1975.

Hohmann H, *et al.* (1993). FCI Experiments in the Aluminumoxide/Water System. *Proceedings of the CSNI Specialists Meeting on Fuel-Coolant Interactions,* Santa Barbara, California, January 5-8, 1993. NUREG/CP-0127. NEA/CSNI/R(93)8. Also in *Nuclear Engineering and Design* 155 (1995) 391-403.

Hohmann H, *et al.* (1994). Advance in the FARO/KROTOS Melt Quenching Test Series. *22nd Water Reactor Safety Information Meeting,* Bethesda, Maryland, October 24-26, 1994.

Huhtiniemi I, Hohmann H, Magallon D (1995). FCI Experiments in the Corium/Water System. *Proceedings of the 7th International Meeting on Nuclear Reactor Thermal-Hydraulics, NURETH-7,* Saratoga Springs, New York, September 10-15, 1995.

Incropera FP, DeWitt DP (1990). *Fundamentals of Heat and Mass Transfer.* Third Edition. John Wiley & Sons. 1990.

Lunardini VJ (1991). *Heat Transfer with Freezing and Thawing.* Elsevier. 1991.

Patankar SV (1980). *Numerical Heat Transfer and Fluid Flow.* Hemisphere. 1980.

Rempe JL, *et al.* (1993). Light Water Reactor Lower Head Failure Analysis. *NUREG/CR-5642.* EGG-2618. U.S. Nuclear Regulatory Commission. October 1993.

Roche MF, *et al.* (1993). Solidus and Liquidus Temperatures of Core-Concrete Mixtures. *NUREG/CR-6032.* ANL-93/9. U.S. Nuclear Regulatory Commission. June 1993.

Theofanous TG, *et al.* (1994). A Study of Ex-Vessel Steam Explosions in Swedish BWRs. *Proceedings of the OECD/NEA/CSNI Specialist Meeting on Selected Containment Severe Accident Management Strategies,* Stockholm, Sweden, June 13-15, 1994. NEA/CSNI/R(95)3.

DISTRIBUTION:

Beredskabsstyrelsen
Attn: Björn Thorlaksen
Louise Dahlerup
P.O.Box 189
DK-3460 Birkeröd

Risö National Laboratory
Attn: Povl Ölgaard
Frank Höjerup
Knud Ladekarl Thomsen
Peter Fynbo
P.O.Box 49
DK-4000 Roskilde

Finnish Center of Radiation
and Nuclear Safety
Attn: Lasse Reiman (3)
Kalevi Haule
Timo Karjunen
Juhani Hyvärinen
P.O.Box 14
FIN-00881 Helsinki

Teollisuuden Voima Oy
Attn: Markku friberg
Heikki Sjövall
Seppo Koski
Risto Himanen
FIN-27160 Olkiluoto

IVO International Ltd
Attn: Harri Tuomisto
Petra Lundström
Olli Kymäläinen
FIN-01019 IVO

Jussi Vaurio
Loviisan Voimalaitos
P.O.Box 23
FIN-07901 Loviisa

Björn Wahlström
VTT Automation
P.O.Box 13002
FIN-02044 VTT

VTT Energy
Attn: Lasse Mattila
Ilona Lindholm (5)
Risto Sairanen (5)
Kari Ikonen
Esko Pekkarinen
Ari Silde
P.O.Box 1604
FIN-02044 VTT

Tord Walderhaug
Geislavarnir Rikisins
Laugavegur 118 D
IS-150 Reykjavik

Institutt för Energiteknikk
Attn: Egil Stokke
Oivind Berg (3)
P.O.Box 175
N-1750 Halden

Sverre Hornkjöl
Statens Strålevern
P.O.Box 55
N-1345 Österås

Swedish Nuclear Power Inspectorate
Attn: Wiktor Frid (8)
Oddbjörn Sandervåg
Gert Hedner
S-10658 Stockholm

Vattenfall Energisystem AB
Attn: Klas Hedberg
Veine Gustavsson (3)
P.O.Box 528
S-16216 Stockholm

Forsmarks Kraftgrupp AB
Attn: Gustaf Löwenhielm (2)
Henning Danielsson
S-74203 Östhammar

Kenneth Persson (3)
Vattenfall AB
Ringhalsverket
S-43022 Väröbacka

Emil Bachofner (3)
OKG AB
S-57093 Figeholm

Jan-Anders Svensson (3)
Barsebäck Kraft AB
P.O.Box 524
S-24625 Löddeköpinge

Lars Nilsson (4)
Studsvik Eco & Safety AB
S-61128 Nyköping

ABB Atom AB
Attn: Yngve Waaranperä
Timo Okkonen
S-72163 Västerås

ES-Konsult AB
Attn: Erik Söderman
Ferenc Muller
P.O.Box 3096
S-16103 Bromma

Kjell Andersson
Karinta Konsult HB
P.O.Box 6048
S-18306 Täby

Torkel Bennerstedt (5)
NKS
PL 2336
S-76010 Bergshamra

Royal Institute of Technology
Attn: Bal Raj Sehgal (10)
T. N. Dinh
R. R. Nourgaliev
V. A. Bui
J. Andersson
K. Green
Nuclear Power Safety
S-10044 Stockholm

U.S. Nuclear Regulatory Commission
Attn: Charles Ader
Sudhamay Basu
Washington, DC 20555
U.S.A

Brian Turland
233/A32
AEA Technology
Winfrith
Dorchester
Dorset DT2 8DH
UK

Mati Merilo
Electric Power Research Institute
P.O.Box 10412
CA 94303
U.S.A